MAGNETICS DESIGN
FOR HIGH CURRENT LOW VOLTAGE DC/DC CONVERTER

by

HUA ZHOU
B.S. Xi'an Jiaotong University, 1994
M.S. Xi'an Jiaotong University, 1997

A dissertation submitted in partial fulfillment of the requirements
for the degree of Doctor of Philosophy
in the School of Electrical Engineering and Computer Science
in the College of Engineering and Computer Science
at the University of Central Florida
Orlando, Florida

Summer Term
2007

Major Professors:
Thomas X. Wu
Issa Batarseh
Khai D. T. Ngo

UMI Number: 3377841

INFORMATION TO USERS

The quality of this reproduction is dependent upon the quality of the copy submitted. Broken or indistinct print, colored or poor quality illustrations and photographs, print bleed-through, substandard margins, and improper alignment can adversely affect reproduction.
In the unlikely event that the author did not send a complete manuscript and there are missing pages, these will be noted. Also, if unauthorized copyright material had to be removed, a note will indicate the deletion.

UMI®

ABSTRACT

With the increasing demand for small and cost efficient DC/DC converters, the power converters are expected to operate with high efficiency. Magnetics components design is one of the biggest challenges in achieving the higher power density and higher efficiency due to the significant portion of magnetics components volume in the whole power system. At the same time, most of the experimental phenomena are related to the magnetics components. So, good magnetics components design is one of the key issues to implement low voltage high current DC/DC converter.

Planar technology has many advantages. It has low profile construction, low leakage inductance and inter-winding capacitance, excellent repeatability of parasitic properties, cost efficiency, great reliability, and excellent thermal characteristics. On the other side, however, planar technology also has some disadvantages. Although it improves thermal performance, the planar format increases footprint area. The fact that windings can be placed closer in planar technology to reduce leakage inductance also often has an unwanted effect of increasing parasitic capacitances. In this dissertation, the planar magnetics designs for high current low voltage applications are thoroughly investigated and one CAD design methodology based on FEA numerical analysis is proposed. Because the frequency dependant parasitic parameters of magnetics components are included in the circuit model, the whole circuit analysis is more accurate.

When it is implemented correctly, integrated magnetics technique can produce a significant reduction in the magnetic core content number and it can also result in cost efficient designs with

less weight and smaller volume. These will increase the whole converter's power density and power efficiency. For high output current and low output voltage applications, half bridge in primary and current doublers in secondary are proved to be a very good solution. Based on this topology, four different integrated magnetics structures are analyzed and compared with each other. One unified model is introduced and implemented in the circuit analysis. A new integrated magnetics component core shape is proposed. All simulation and experimental results verify the integrated magnetics design.

There are several new magnetics components applications shown in the dissertation. Active transient voltage compensator is a good solution to the challenging high slew rate load current transient requirement of VRM. The transformer works as an extra voltage source. During the transient periods, the transformer injects or absorbs the extra transient to or from the circuit. A peak current mode controlled integrated magnetics structure is proposed in the dissertation. Two transformers and two inductors are integrated in one core. It can force the two input capacitors of half bridge topology to have the same voltage potential and solve the voltage unbalance issue. The proposed integrated magnetics structure is simple compared with other methods implementing the current mode control to half bridge topology. Circuit analysis, simulation and experimental results verify the feasibility of these applications.

To my family

ACKNOWLEDGMENTS

With the sincerest and warmest appreciations from my heart, I would like to say thanks to my advisor Dr. Thomas X. Wu, and co-advisors Dr. Issa Batarseh and Dr. Khai Ngo for their guidance and encouragement through my studies at the University of Central Florida. Their extensive vision and creative thinking have been the source of inspiration for all my work. During the past several years, I have learned from them not only knowledge but also their strict approaches to scientific research. These are going to benefit me for the rest of my life.

I would also like to thank other committee members: Dr. Z. John Shen, Dr. Yanfei Liu and Dr. Jun Wang for their support and encouragement.

It has been a great pleasure to study in the Florida Power Electronics Center at University of Central Florida. I cherish the friendships that I have made over there. I would like to thank the following visiting scholars or my fellow students: Dr. Hong Mao, Dr. Jaber A. Abu Qahouq, Dr. Xianfcheng Wang, Dr. Jun Liu, Dr. Songquan Deng, Mr. Shangyang Xiao, Mr. Liangbin Yao, Ms. Yangyang Wen, Mr. Osama Abdel Rahama, Ms. Majd Batarseh, Mr. Feng Tian, for the useful discussions.

Finally, my deepest and heartfelt appreciation goes to my families for their unconditional love.

TABLE OF CONTENTS

LIST OF FIGURES

LIST OF TABLES

CHAPTER 1: INTRODUCTION

1.1 Magnetics Components for Power Electronics

The origin of modern power electronics was stimulated by the development of power semiconductor devices for high frequency switching purposes. At the same time, magnetic cores for transformers and inductors are another important and necessary accompanying component.

There are various magnetic functions that are used in a switching power supply. They are:

1. Power transformer;

2. Power inductor or choke;

3. In-line or differential-mode choke;

4. Common-mode choke;

5. EMI suppression;

6. Pulse transformer for transistor firing;

7. Magnetic amplifier;

8. Power factor correction.

The choice of the best magnetic component is determined by:

1. The type of converter topology used;

2. Frequency of the circuit;

3. Power requirements;

4. The regulation needed (percentage variation of output voltage permitted);

5. Cost of the component;

6. Efficiency required;

7. Input and output voltages and currents possible consistent with other factors.

With the increasing demand for small and cost-efficient DC/DC converters, the power converters are expected to operate with high efficiency. However, even with modern improved and advanced topologies, magnetics design is still one of the biggest challenges in achieving the higher power density and higher efficiency due to the significant portion of magnetics volume in the whole power system [1]. At the same time, most of the experimental phenomena are related to the magnetics components. In many power application situations, the magnetics components can not be omitted due to the safety reasons. So, good magnetics components design is one of the key issues to implement low voltage high current DC/DC converter.

In recent years, there are two distinct trends in power electronics magnetics design. One considers the use of planar structures [2]. Planar has closer board spacing, applies simpler conductor assembly methods, and therefore achieves lower profile and better manufacture ability. The planar electrical features are also repeatable. These advantages makes planar prevail in the power converter industry. The other trend is to push the frequencies. Because magnetic cores are traditionally the largest component in a solid-state circuit, operation at high frequencies is seen as a possible solution to decrease the volume. Several hundreds of kilohertz systems are being extended; and there is also a push of switching frequencies in the several-megahertz range [3]. However, the design of transformers and inductors is usually a limiting technology for higher frequency systems.

The integrated magnetics as an approach to accomplish low profile and high power density in power applications has been investigated intensively [4][5]. With integrated magnetic

techniques, several magnetic components can be constructed in one magnetic core by sharing a common magnetic path. Thus, the number of magnetic cores can be reduced. The flux ripple and the current ripple can also be suppressed. Hence, with magnetic integration technologies, low cost and high power density power converter can be achieved.

The magnetic components often occupy a large portion of size in a power converter. How to get an optimal magnetics design is critical to minimize the system profile and further increase its power density. Integrated magnetics technology, planar magnetics technology and passive integration technology are developed to reduce the profile and the component counts and to eliminate some of the interconnections between different components. In the conventional approaches, magnetic components are often designed based on magnetic-circuit reluctance models. Core loss and conduction loss in magnetic devices are roughly estimated. With the increase of switching frequency driven by the continuously lower profile and higher power density, it becomes difficult to evaluate the loss due to skin effect and proximity effect through the traditional analysis methods. Subsequently, FEA (Finite Element Analysis) method based on numerical analysis of electromagnetic fields has been adopted. From the computed electromagnetic fields results, FEA can accurately evaluate conduction loss, core loss and magnetic field distribution for each of the winding structures with different core geometry. Then, an optimized magnetics design can be achieved.

1.1.1 Power Transformer

For power transformer, because high permeability cores are always used to maximize the coupling between different windings, the magnetizing current is small compared to load current

(2% to 10%). But, the stability of magnetizing and leakage inductances may be poor, since it varies with mechanical handling, electrical or thermal shocks. Resonant frequency of primary may be well below maximum operating frequency for wideband transformers. Most of the time, the voltage ratio differs slightly from actual turn ratio. The performance is affected by winding resistance which is independent of signal level, but increases with frequency due to the skin effect. The performance is also affected by leakage inductance which appears in series with the winding resistance due to imperfect magnetic coupling between windings.

Power transformers have one common requirement: the material saturation value should be as high as possible, consistent with other factors such as small core loss. At very low frequencies, the materials are saturation-driven and the eddy current losses are moderately low. At high frequencies, the materials are core-loss-driven so that the materials such as ferrites are generally used. For medium high frequencies, materials such as thin gage silicon iron, amorphous materials and the new Nano-crystalline materials are available. In power transformer functions, a high saturation material with low losses under the operating conditions is desirable. The desirable materials for transformer cores are those that have a high flux density and keep the temperature rise within desirable limits. The major magnetics components material for the power electronics is the ferrite.

Planar transformers designed for power applications must satisfy the same requirements as conventional power transformers. These requirements include the mechanisms minimizing the loss and the provision of an acceptable cooling strategy. The task of minimizing the core losses is similar to that of a conventional wound magnetic. It requires suitable choices of the switching frequency, core shape and size, and core material. For different design, the main difference lies

in the choice of core shape and size. For magnetics components, there is no best core shape and the tradeoff must be made. It depends on the application, space constraints, temperature, winding capabilities, assembly, and a number of other factors.

Minimizing copper losses at high frequency requires a good understanding of the principles of skin effect and proximity loss. Interleaving is a well-known technique used to minimize high frequency effects contributing to winding losses within planar turns. However, the level of interleaving is limited by considerations of capacitive effects between different windings and the concerns of providing adequate levels of isolation between the windings. So, it is usually not the best solution to fill the core window with copper. In fact, in many applications high levels of interleaving of relatively thin layers results in a high insulator to copper. This makes the use of printed circuit boards particularly suitable for transformer winding structures despite the upper limit of approximately 45% to 50% on copper utilization of the window. In some very low profile applications, the copper utilization factor can be increased through the use of thinner insulation systems. In the case of single-turn, single-layer winding designed to carry high current, thick external copper stampings can augment or replace PCB layers. In some applications where further interleaving is undesirable or not practical, thicker copper may be used for improved thermal transfer without a loss or efficiency penalty.

1.1.2 Power Inductor

Power inductor applications are mainly focused on their capability to store large amounts of power in their magnetic field. They are different from the inductors used in LC circuits for frequency control. As such, they can limit the amount of AC voltage and current. Since there are

large DC current and smaller superimposed AC current, air gaps are needed to prevent the core from saturation. The amount of gap depends on the maximum DC current, the shape and size of the core and the inductance needed for energy storage.

Because of a large DC component in power inductors, the gapped ferrite cores are used for many high current power applications. The gap is added when there is a threat of saturation that would allow the current in the coil to build up and overheat the core catastrophically. Gapped core can also be used to control the inductance and to raise the Q value of the core. Since the AC component is small, core loss is not as important as in the case of the power transformers. The shape of the component influences the performance of the device. The reduction in temperature rise will depend on some factors such as the operating frequency, the gap length and the wire diameter.

1.2 Planar Magnetics

Philips (1998) claims the advantages of the planar technology including low profile construction, low leakage inductance and inter-winding capacitance, excellent repeatability of parasitic properties, low cost, great reliability and excellent thermal characteristics.

The characteristics of planar magnetics are not all advantageous. Although it improves thermal performance, the planar format increases footprint area. Even the windings can be placed closer to reduce leakage inductance; it usually has an unwanted effect of increasing parasitic capacitances. The repeatability of characteristics obtained from PCB windings structure also comes at the price of having a greater portion of the winding window filled with dielectric material, thus reducing copper fill factor and limiting the number of turns. Further more, typical

6

problems of planar structures are the thermal management and the high value of the capacitive effects. In many applications, it still has some advantages to use multi-layer PCBs in planar magnetics. Since the multi-layer PCBs allow the interconnection of arbitrary layers, the interleaved primary and secondary windings can be implemented much more easily than with conventional magnetics. This provides the means to further reduce leakage inductance value and decrease high frequency winding losses. This is a good feature for high frequency square wave switching applications. Another advantage of the planar magnetic is that it enhances thermal performance because of the greater surface area to volume ratio providing more area to contact the heat sink. This is illustrated in the smaller value of thermal resistance quoted for planar cores over conventional cores.

1.2.1 Low Profile

An important feature of planar transformers is their low profile. This feature makes possible the use of planar transformers in on-board converters. This is one reason that planar magnetics has large footprint area. The term low profile is often used to describe planar magnetics. However, not all low profile magnetics are planar. In particular low profile cores, such as the EFD type, use conventional wire wound technology, lacking many of the characteristics of planar magnetics.

The effect of core height on power density has been studied in several references. Some of these studies have compared planar magnetics to more conventional low profile magnetics and found that the low profile magnetics can have better volumetric efficiency and higher power density for certain applications.

1.2.2 High-Frequency Losses

Some earlier studies assess winding configurations, investigate the optimal placement of windings, compare different winding technologies and optimize layouts of turns to minimize overall winding resistance. Among different winding configurations involving the use of solid wire, Litz wire, PCB and foil windings at 500 kHz, PCB windings have lower AC resistance (approximately 85% – 90%) than similar solid wire windings but higher than Litz wire windings (approximately 115%). Leakage inductances of the PCB implementations are lower than both the wire and Litz wire implementations.

It also became evident that circularly wound planar windings can have significant 2D field effects in the winding window, which gives rise to losses not accounted for by the traditional approach to the winding loss computation. These effects are also investigated for foil windings and conclusions are drawn as to how these 2D or edge effects might be minimized. The conclusions are that winding losses are minimized for primary and secondary layers with equal width, and with minimum spacing between winding end and core center leg.

1.2.3 Leakage Inductance

The easy interleaving in planar structures allows the minimization and control of leakage inductance within the windings. However, particular attention should be paid to the termination of the windings. For example, depending on the secondary termination method used, the leakage inductance presented to the circuit can be up to three times that computed by the classical short circuit secondary approach.

It is obvious that the benefits of careful transformer design can easily be nullified by a lack of care in the connection of the transformer to the rest of the circuit. Inappropriate termination design can account for as much as 75% of the short circuit AC resistance of a planar device**.**

1.2.4 Planar Winding Technologies

Various technologies can be used to implement the planar windings. The most popular ones are Printed Circuit Board (PCB), flex circuit and stamped copper. Windings fabricated in thick film and LTCC have also been used primarily in lower power applications.

The use of PCBs gives a highly repeatable means of implementing planar windings. In principle, the windings can be an integral part of the system interconnection substrate thus totally eliminating all terminations. In practice, however, the interconnection substrate rarely has sufficient layers to fully accommodate the magnetic component windings. But, it's still better than other winding technology. The disadvantage of PCBs is that the window utilization factor can be quite low (typically 0.25 - 0.3 compared to 0.4 for conventional magnetics) due to a typical inter-turn spacing and minimum dielectric thickness.

Flex circuit (copper on a thin, flexible polymer substrate) gives an improved utilization factor as the dielectric thickness is as low as 50μm. Many layers of flex circuit can be laminated together resulting in a rigid structure similar to a PCB but with increased utilization factor. On the other side, it can facilitate the use of techniques such as the "z-folding" method. This folding method can be used to implement a large number of layers without the need for via or soldering for layer interconnects. Similar to PCBs, flex conductor thickness may be limited to standard thickness, typically 17, 35, 70, and 105μm, with minimum conductor spacing increasing with

9

thickness. Unlike PCBs, the flex technologies are more suited to much heavier copper weights, e.g. 210μm or larger.

Stamped copper windings provide an inexpensive means to implement thick single turn windings. The main disadvantages are that insulation layers must be separately applied and layer interconnection is provided by some external means.

1.3 Integrated Magnetics

One of the more interesting magnetics design techniques in practice today is construction of the transformer and inductor on a single magnetic core structure. This technique has come to be known as Integrated Magnetics (IM) design. IM methods have become increasingly popular since 1977, when "coupled-inductor'' assembly concepts and associated converter designs [15] [16] [17] are more fully disclosed. Implemented correctly, IM techniques can significantly reduce the magnetic core content of related power circuits and result in cost-efficient designs. This kind packaging has been extended to include implementations in planar forms, using printed-circuit approaches for windings together with low profile ferrite core constructions.

It was subsequently demonstrated in 1984 [18] [19] for circuit arrangements and in 1987 [20] on a system level that all power conversion circuit designs of the switch mode have one or more IM forms. Prior to these points in time, it is commonly believed that only those power circuits where transformer and inductor have dynamically proportional winding potentials could have IM forms. Such special converter circuits include transformer-isolated versions of the C'uk [16], SEPIC and ZETA topologies. However, by using core structures that possess more than one major material flux path [18], IM techniques can be applied to all switch mode power systems,

and can be extended to include other magnetic elements often excluded. One example of such elements is the secondary stage input and output filter inductances used for reducing conducted AC current ripples.

IM designs typically use soft-ferrite E-I or E-E core structures. The main difference among different structures is different winding arrangements on the three "legs" of the core. For the core leg where inductor windings are situated, an air gap is needed to obtain the desired inductance values and keep the core from saturation. Effective core leg areas must be chosen in accord with the maximum flux levels that will occur as a result of converter operation so as to prevent saturation of the core under maximum loading conditions of the system. The use of printed wiring methods for the IM windings can lower the height profile of the overall package of the magnetic component.

Conventional IM constructions, whether they use PCB style or wire windings, do have some undesirable limitations. Because windings are putted on the outer legs of the core, it is not possible to completely surround all windings with core material to restrict magnetic leakage levels. Also, because conventional constructions using E-I or E-E cores restricting window locations for windings to two locales and material flux paths to a maximum of three, other power magnetic components in a converter circuit (like input and output filter inductances) cannot be easily accommodated in an IM arrangement without significant topology changes. This, in turn, often leads to undesirable compromises in power converter performance.

1.4 Outline of Research

In this dissertation, magnetics components designs for low voltage high current applications are investigated thoroughly. Some specific designs are described in detail. The research work is mainly focused on these following topics:

1. magnetics component structures;

Four different integrated magnetics structures are analyzed and compared thoroughly in this dissertation. The characteristics and power loss mechanism of IM structures are investigated. To increase the efficiency of magnetics component, one optimized IM structure is proposed. This design optimizes the core shape to decrease the copper loss.

1. unified magnetics component model;

When different integrated magnetics structures are compared, the unified circuit model is needed. Otherwise, for different winding number and different winding locations, it is hard to get the reasonable comparison results. One unified circuit model is introduced in this dissertation. Only the terminal parameters are consider in this model and it is constructed from the simplified and unified impedance matrix. Then, any component model can be unified by several coupled inductors. This simplifies the circuit analysis.

2. design methodology;

Conventionally, magnetics component designs are based on the reluctance model analysis results. Before the component is real constructed, the performance can only be roughly estimated. In this dissertation, FEA simulation is included in the design procedure and one CAD design methodology is introduced. Because the parasitic effects and terminal effects are all included in the simulation results, the model based on this simulation result is accurate. This

helps to evaluate magnetics design before it is really made. This is also helpful to decrease the design period and design cost.

3. different applications of magnetics components.

Generally, transformer is a passive device which transforms electric energy from one circuit into another through electromagnetic induction. In this dissertation, a new application for transformer in VRM application is introduced. The transformer works as a voltage source in active voltage design. When transformer works during the VRM transient time, it injects or absorbs the extra transient current to or from the load circuit. It is similar to an extra voltage source added to the original topology. During the transient time, the working frequency is meager-hertz. So the transient response is fast.

Another new application is introduced in section 4.3. Because of half bridge topology inherent voltage unbalance issue, the current mode control can not be used directly. Because the current mode control has some advantages compared with voltage mode control, such as cycle by cycle over load limitation and fast transient response, a new magnetics component structure is proposed to make up the topology shortage. The circuit structure is simple and the control method is easy to be implemented.

CHAPTER 2: CHARACTERISTICS OF MAGNETICS COMPONENTS FOR HIGH CURRENT APPLICATIONS

2.1 Magnetics Components Modeling and Simulation

The integrated magnetics is a promising technique to reduce the size of the magnetic components and improve the behavior of the circuit. The use of magnetics components containing windings in different core leg is a common practice to integrate transformer and inductor in the same magnetic core. The use of a model for integrated magnetics is a helpful tool to select adequate winding strategy. Because the selection of the core, air gaps and winding setup are not easy, the accurate model is needed to select the appropriate constructive parameters. The voltage differences between turns, between winding layers and between windings to core create parasitic elements for magnetics components. It is hard to model the critical parasitic parameters just through the traditional reluctance model.

The reluctance that models the leakage path is dependent on the geometry of the windings. Different winding arrangements produce different leakage inductances. The leakage inductance is extended to include flux in the radial field. It is desirable to predict these leakages and develop an electrical model to ensure that the electrical properties of the magnetics components are suitable for the converter topology. Accurate modeling and simulation can reduce the costly delays. In the conventional model, the reluctance that models the leakage path cannot always be related to the physical structure of the magnetic components. The topology of the conventional model has been previously discussed [16][17][18][19].

The relationship between dual electrical circuits is based on the interchange junction-points and meshes. An identical relationship exists between the magnetic circuit of the magnetic component and its equivalent electrical circuit. The physically-based model of the multi-winding magnetic component is introduced in [20]. The electric-magnetic duality theorem is applied to extract the electrical model form the magnetic model. Therefore, the final electrical model is derived directly from the actual physical magnetic structure under investigation. All the parameters in the model have one-to-one relationship with corresponding physical quantities in the original magnetic structure.

The electrical models of multi-winding transformers can be expressed in several different ways. The "ladder" model is one of the most popular and widely used magnetics models in power electronics. It consists of a magnetizing inductance and a series of "leakage" inductances connected between the adjacent windings. In relatively simple magnetics structures, the parameters of the ladder model can be easily related to the geometry of the core and the windings. The inductances can be computed by relating the flux pattern to the physical arrangements of the core and the windings. But, it should be noted that the widely-used ladder model is an approximation based on winding geometry: the couplings between non-adjacent windings are neglected. The author [28] has shown that geometry alone is insufficient to justify this approximation. For an n-winding transformer, the ladder model has 2n-1 independent parameters. On the other side, the inductance matrix in the general magnetics model has $n(n+1)/2$ independent parameters.

FEA tools have been used to model different integrated structures. The goal is to obtain the coupling parameters among different windings, and then generate a simple model based on

linearly coupled inductors. Since the 3D FEA solvers are not efficient in terms of computation time, a 2D approach has been developed by applying the "Double 2D" technique [15]. Double 2D approach is based on the division of the windings of the magnetic component in two parts. Each part produces field distribution in different planes of the space. Using this technique it is assumed the linearity in the conductors. The preconditions of the "double 2D" method are: parts of the conductors that are considered in each simulation are perpendicular, the dotted product of the fields created by them is zero, and therefore the interaction of both simulations is null. The effect of the corners of the conductors is neglected, which is not a wrong assumption for most practical cases. The error is still under the acceptable range.

The main advantages of the FEA double 2D method are:

1. It is accurate and 2D effects (like the fringing flux around the air gap area) are considered, since it is based on FEA calculations;

2. Since it is frequency dependent, it is valid for non-sinusoidal waveforms. This is very useful for SMPS application;

3. The couplings between each pair of windings are accurately calculated;

4. Since 2D FEA solvers are used instead of 3D ones, the solution time is not very high.

The main drawback of the FEA solvers is that a FEA tool is needed and it is necessary to learn how to use it. Meanwhile, although the solution time is not an issue using the latest generation computers, the problem definition in the FEA tool (geometry, materials and boundary conditions) is tedious. However, this is the only way to proceed with FEA tools.

2.2 Integrated Inductors for High Current Application

Powering digital system needs high-current low-voltage power converter with fast transient response. The combination of high current and fast response requires a voltage regulator module (VRM) located adjacent the load. At present, the standard design is a buck converter with multiple staggered in phase parallel sections [7],[8],[9],[10],[11],[12]. In a buck converter, when the load current changes, the inductor current ramps up or down to match the new load current. At the same time, the output capacitor supplies the difference current. The small inductor allows the ramping current to quickly minimize the output capacitor requirement. On the other hand, the small inductor leads to large current ripple. Because the full current ripple flows through the MOSFET switch and the inductor itself, higher current ripple results in higher losses and higher peak current requirements. For a single phase converter, large current ripple will increase the requirement of the output capacitor. Increasing the operating frequency can reduce the current ripple. But it also can increase the switching and gate-drive losses and magnetics core loss.

Interleaved converter is a suitable solution for many applications due to the better dynamic response, better thermal management, smaller filters, less EMI content and better package. This allows the smaller inductance without a large output capacitor. When a large number of phases are used, package issues are very important, and magnetic components volume is a critical point. In this situation, coupled inductor structure can decrease the number of magnetic cores and simplify the circuit components. At the same time, it still can decrease the current ripple and have good transient response. In [13],[14], it is shown that coupled inductors in interleaved converter can reduce the current ripple. This reduction can extend to the inductor winding and switch itself. There are three kinds of integrated inductors:

1. Discrete inductors packaging: the inductors are discrete components and they are packed remaining independent one from others. Both dynamic and static performances remain unchanged. The main drawbacks of this kind integration are high losses and big size.

2. Decoupled integrated inductors: the inductors are integrated on the same core. The interleaving concept is extended to magnetic fluxes: fluxes with the same waveform and time shifted are added or subtracted. The component acts mainly as an inductor, storing energy in the core. The main benefits obtained with integration are the size, losses and cost reduction.

3. Tightly coupled inductors: the windings are integrated on the same magnetic core. The component acts as a transformer because, ideally, no energy is stored in the core, but it is transferred from one phase to the others. In this situation, filtering needs are dramatically reduced.

2.3 Integrated Transformer and Inductors

The current–doubler rectifier (CDR), depicted in Fig. 2.1, is widely used and appears in several papers and textbooks [21].
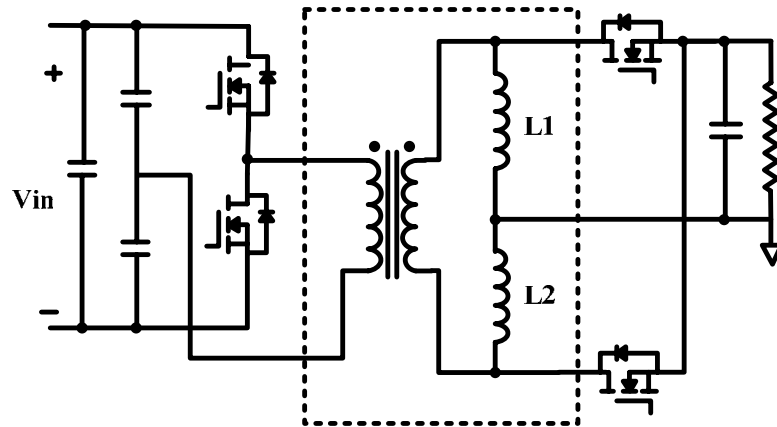
Fig. 2.1 Half bridge and current doubler circuit topology

The circuit is rediscovered recently for high frequency DC/DC converter applications. The low current stresses in the transformer secondary side, the inductors and the rectifiers make this circuit especially attractive for DC/DC converters with high output currents. The circuit can be used with different double-ended primary topologies, such as push-pull, half bridge, and full bridge [22], [23]. Half bridge converter is preferred for lower reversal voltage which is equal to half of the input voltage in theory. Moreover, because the primary leakage inductance spikes can be clamped to the DC supply bus, the leakage inductance energy is returned to the input power supply instead of to be dissipated in some resistive elements. At the same time, because the half-bridge converter has fewer components, it can simplify the implementation of converters. Many references have shown that half bridge topology is very promising for low voltage high current application.

A disadvantage of the CDR is the need for three magnetic components, namely, one transformer and two inductors. Besides the size and cost concerns, the interconnection losses of these components also have negative impacts on efficiency, especially in high-current

applications. To solve this problem, the two filter inductors can be magnetically coupled, as suggested in [24]. At the same time, integrated magnetic structures that implement the transformer and the two inductors on a single magnetic core have been proposed. Fig. 2.2 shows four such structures that have been published in the literatures [25], [26], and [27]:

Structure 1   Structure 2

Structure 3   Structure 4
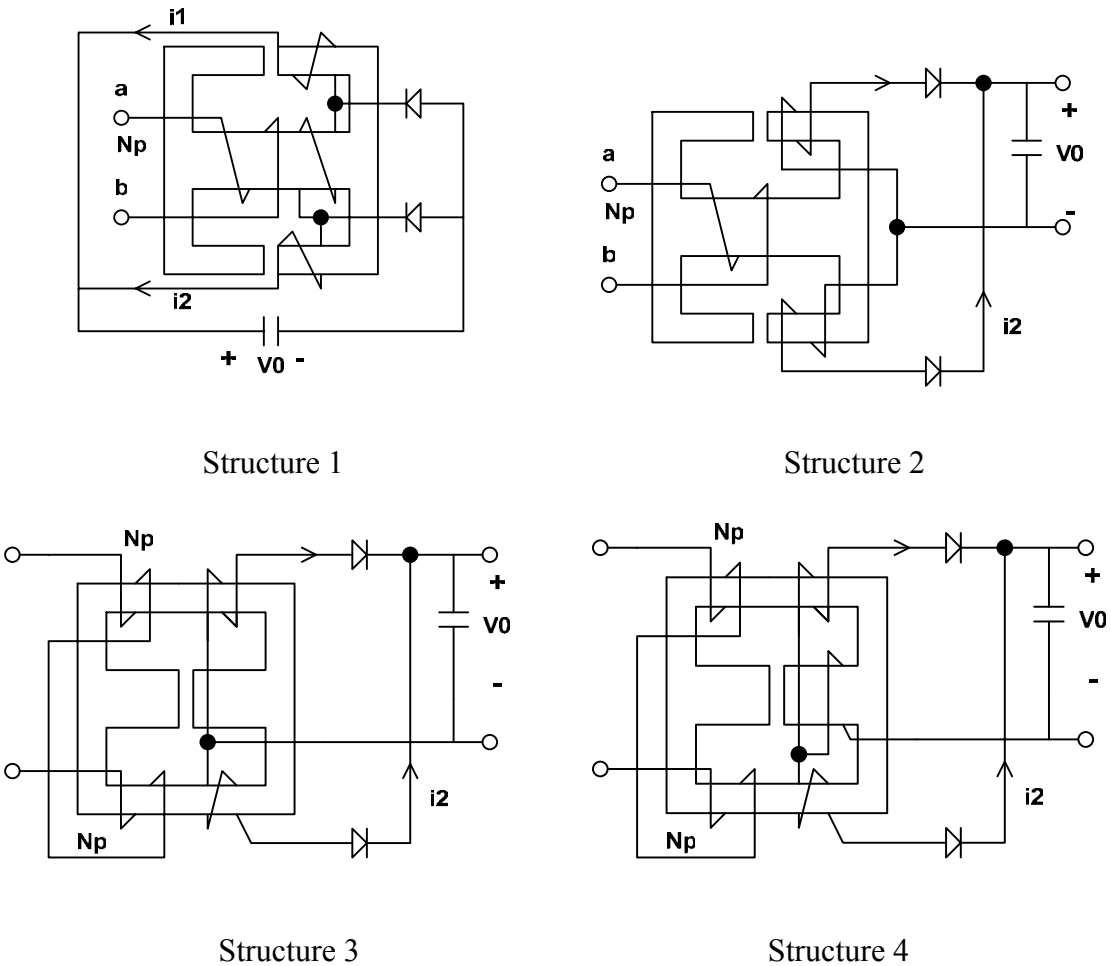
Fig. 2.2 Four different integrated magnetic structures

In structure 1, the transformer and inductor windings can be selected independently. This provides freedom in the design and allows higher inductance to be achieved. But, the separated

transformer and inductor windings imply the use of more copper as well as higher conduction loss and interconnection losses. In structure 2 [25], the transformer primary and second windings are located in the different legs. Then, the leakage inductance between the primary and secondary windings is high. This structure has limited filter inductance value. In structure 3 [26], it has lower leakage inductance compared with structure 2. It also has limited filter inductance. In structure 4 [27], there is an extra winding added in the center leg. This can increase the filter inductance value. In [27], the filter inductance value can be tripled when there is one turn extra winding in the center leg. When the frequency is low, the copper loss of structure 4 is lower than the structure 3 because of the lower current ripple. When the frequency is high, the advantage is not so obviously because the extra winding will bring in the extra copper loss.

Based on the current-doubler rectifier's working modes, some paper derive the equations from the reluctance model for each working mode. The performance of the IM structure is evaluated based on these equations. The question is, if there is no specific working circuit, how the IM structure can be analyzed.

2.4 Core Loss for Non-Sinusoidal Waveforms

Traditionally, the Stienmetz's equation is used to calculate the power density of the core. It expresses loss density with fixed exponent of frequency and flux density.

$$P = kf^{\alpha}B^{\beta} \tag{1}$$

This equation may work in a limited frequency or limited flux density range. It is not suitable for non-sinusoidal waveforms. These exponents are known to change significantly with

21

frequency, flux density and waveforms. This kind of variation represents the fact that relative contributions of the three fundamental loss mechanisms (hysteretic, classical eddy current and excess eddy current) change with frequency, flux density and waveforms [6]. Switching power converters can have very different waveforms and these non-sinusoidal waveforms will result in different losses [30], [31]. By the way, DC bias value can also significantly affect loss [32], [33], [34].

In [29], the author defines effective amplitude as amplitude that may be substituted into a simple formula, originally intended for simple waveforms, to enable calculation of loss arising from arbitrary waveforms. The use of rms amplitude for this case is dependent on the loss mechanism in the resistor. Effective frequencies are less commonly used than effective amplitudes, but can be useful for frequency-dependent winding losses [25], [26], [27]. Again, the calculation of effective frequency is specific to the loss mechanism.

A fairly general hypothesis for instantaneous core loss is [36]:

$$P_v(t) = P_d\left(\frac{dB}{dt}, B\right) \tag{2}$$

Where P_d is an unknown power dissipation function, a formula that can be used to calculate loss for any waveform for P_v is [29]:

$$P_v = \frac{1}{T}\int_0^T k_1 \left|\frac{dB}{dt}\right|^{\alpha} |B(t)|^{\beta-\alpha} dt \tag{3}$$

$$k_1 = \frac{k}{(2\pi)^{\alpha-1}\int_0^{2\pi} |\cos\theta|^{\alpha} |\sin\theta|^{\beta-\alpha} d\theta} \tag{4}$$

22

To use Steinmetz equation, what are needed are an effective frequency f_e and effective amplitude B_e.

$$P_v = \frac{1}{T} \int_0^T k_1 \left| \frac{dB}{dt} \right|^\alpha |B(t)|^{\beta-\alpha} \, dt = k_1 f_e^\alpha B_e^\beta \tag{5}$$

The effective frequency should be related to the change rate of the waveform, and the effective amplitude should relate to the amplitude of the waveform features.

$$B_e = \left(\frac{1}{T} \int_0^T |B(t)|^b \, dt \right)^{\frac{1}{b}} \tag{6}$$

Where b =1 for average absolute value and b = 2 for rms.

$$f_e = k_2 \left(\frac{\int_0^T \left| \frac{dB}{dt} \right|^\alpha |B(t)|^{\beta-\alpha} \, dt}{\int_0^T |B(t)|^\beta \, dt} \right) \tag{7}$$

This is a reasonable, defensible choice for effective frequency.

Equation 5 is the generalized Steinmetz equation (GSE). It can be considered a generalization of the Steinmetz equation for any waveform. It has an improvement in that different nominal periods of the waveforms do not affect the result, and, for sinusoidal waveforms, it is expected to provide the same accuracy as the Steinmetz equation does. An important limitation of this equation is that it is typically necessary to use different values of the parameters in the Steinmetz equation for different frequency ranges. This shows that the GSE has limited accuracy for a waveform containing harmonics at a wide range of frequencies.

CHAPTER 3: PLANAR MAGNETICS DESIGN

3.1 Discrete Magnetics Design for Low Voltage and High Current Converter

3.1.1 Design of Planar Transformer

The general design procedure is shown in Fig. 3.1.
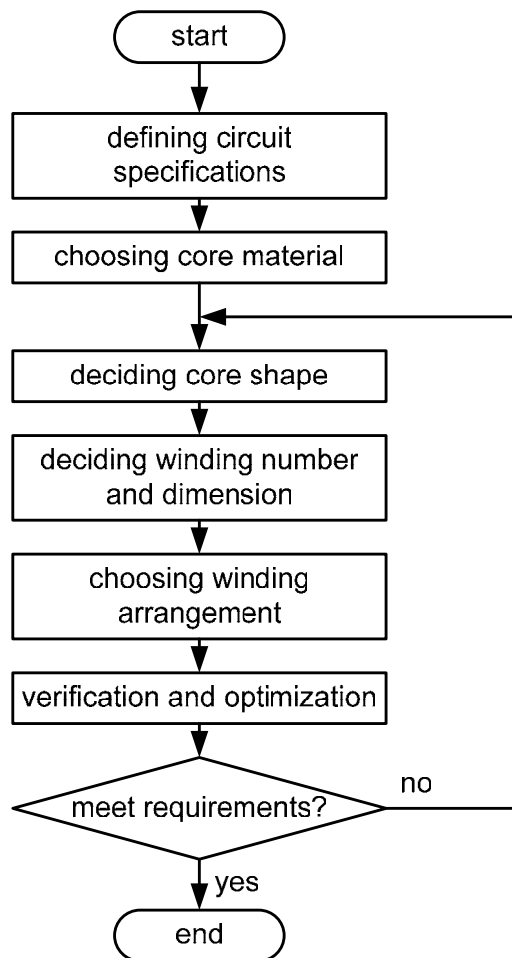
Fig. 3.1 Transformer design procedure

3.1.1.1 Specifications

As it has been discussed before, half bridge with current doubler topology is chosen for this high current and low voltage application. The objective of this work is to design a planar transformer using multi-layer PCB with low profile (0.2 in), output power of 30 W, and high frequency for the proposed DC/DC converter. Fig. 3.2 shows proposed converter topology with the following specifications.
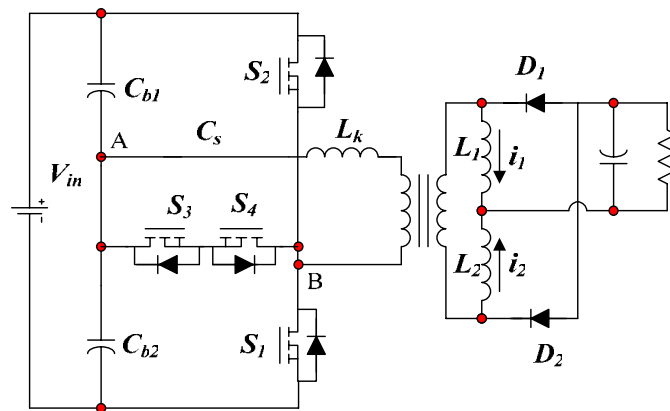
Fig. 3.2 DC/DC converter topology

Size: 0.9 in x 1.3 in x 0.2 in

Input: 36~75V

Output: 1.0V@30A

Load Slew Rate: 50 amps/us, ST 10us max

Deviaton: 3% with zero external capacitance

Efficiency: 86% @ full load

Swithching frequency: $\geq$ 400kHz

I/O: Surface-Mount, configuration not specified

Match Isolation: Basic

The design specifications for the transformer are given as:

Primary voltage $V_1 = 18\sim37.5V$

Turns ratio $n = 6$

Duty cycle $D = 0.4$

Switching frequency $f = 500\text{kHz}$

Ambient temperature $T_a = 40°C$

Allowed temperature rise $\Delta T = 50°C$

In this preliminary design, since the profile of the magnetics is strictly required to be no more than 0.2 in, the commercially available planar ferrite cores with such low profile requirement are evaluated first.

3.1.1.2 Selections of Core Shape and Material

To satisfy the space and height limits, the ER14.5 is chosen for the transformer. The shape and dimensions of the core are shown in Fig. 3. 3.
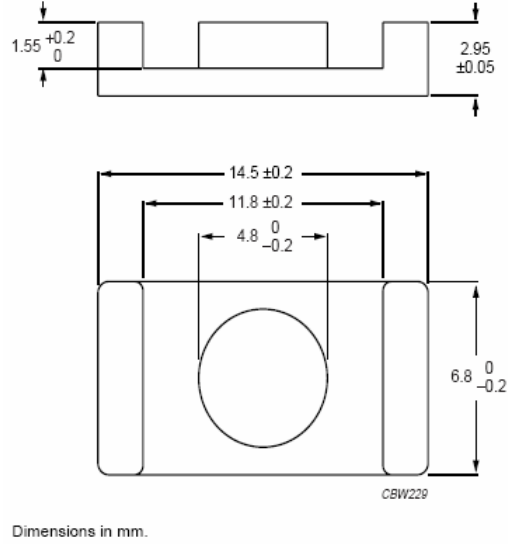
Fig. 3.3 Core shapes (ER14.5)

The next step is to determine the numbers of turns for primary and secondary windings, and then evaluate the core loss. Finally the core material will be selected based on rough calculations of core losses. From the circuit point of view, the turn's ratio of the transformer is initially assumed to be 6 ($n = 6$), and the numbers of turns for primary and secondary windings are chosen as $n_1 = 6$ for the primary winding, and $n_2 = 1$ for the secondary winding. Given these parameters, the maximum flux density can easily be calculated using following equation:

$$B_{max} = \frac{\lambda_1}{2n_1 A_C} = \frac{\int_0^{DT} v_1(t)dt}{2n_1 A_C} \tag{8}$$

Based on the estimated core losses and working frequency, ferrite 3F35 is selected as the magnetic material for the transformer. Meanwhile, the copper thickness of a 4-oz copper (around 140μm) is chosen. If the thickness of the insulation layer of the PCB is 100μm, the total thickness of the PCB will reach:

27

$8 \times 140 + 7 \times 100 = 1820\,\mu m = 1.82mm.$

By now we have determined the core material of ferrite 3F35 and core shape as ER14.5 for the transformer. In the following sub-sections the copper loss, either DC or AC loss, will be evaluated by Ansoft FEM simulation tools. By comparing the copper loss of various interleaving structures, the optimal winding layout is finalized.

3.1.1.3 Winding Arrangements with Loss Simulations

Although the AC loss is usually dominant in the transformer windings loss, it is still necessary to estimate the corresponding DC loss. In the design, the skin depth of copper at 500kHz is 93.5μm for 25°C or 107.9μm for 100°C and the thickness of 4-oz PCB is about 140μm which is less than twice of the skin depth. With these parameters, the DC loss value should basically reflect the AC copper loss if the proximity effect is neglected.

Since there is only one turn for the secondary winding, it is very easy to calculate the DC loss in the secondary winding. The DC loss estimation of the primary winding is more complex than that of the secondary winding. For the primary winding, there are several possible winding connections to obtain the desired 6 turns: (a) 6 turns for one PCB layer; (b) 3 turns for one PCB layer and 2 layers in series; (c) 2 turns for one PCB layer and 3 layers in series; and (d) 1 turn for one PCB layer and 6 layers in series.

The number of turns per layer and the spacing between the turns are denoted by the symbols N_L and S respectively. For an available winding width b_w, the track width w_t can be calculated with following equation (see Fig. 3.4):

$$w_t = \frac{b_w - (N_L + 1) \cdot S}{N_L}$$

(9)
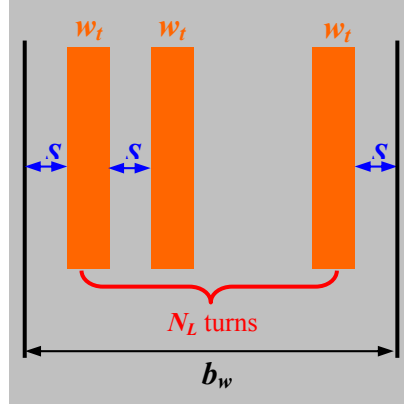
Fig. 3.4 Track width wt, spacing s and winding width b_w

After the number of turns for each layer and dimensions of the PCB track are determined, it is possible to estimate the DC copper losses for both primary and secondary windings. The DC conduction losses for the 4 possible winding connections above are then estimated. By comparing the results, it is obvious that the DC copper loss is least when the primary winding is composed of 2 layers in series and each layer with only 3 turn.

So far we have selected the core material (3F35), core shape (ER14.5), and winding layers for the transformer (2 layers in series and 3 turn each layer for primary winding, 4 layers in parallel for secondary winding). However, such design is usually far away from being optimal to estimate the copper loss only based on the DC analysis. Therefore, it is critical to quantitatively determine the total AC copper loss for various interleaving winding structures. By properly interleaving the primary and secondary windings, the extra AC loss resulting from proximity effect can be reduced to the largest degree.

In order to accurately determine the high-frequency conduction loss in transformer planar windings, an effective electromagnetic simulation tool based on finite element analysis (FEA) is usually desired. Ansoft Maxwell Field Simulator (2D or 3D), as one of the most popular software tools in the industry, provides us with numerical solutions to the complicated 2D and 3D structures. AC conduction losses performance in the transformer will be simulated using Ansoft Maxwell software.

The current distributions on the cross-sectional area of the windings are investigated for various interleaving winding structures. By analyzing the current distribution and conduction loss, the desired interleaving winding structure can be found from simulation results. The accurate AC copper loss can be extracted using Maxwell 3D field simulator.

Considering the structural feature of ER core, an axis-symmetrical model is adopted in Maxwell 2D simulation. Fig. 3.5 shows the possible winding arrangements for the transformer. The red conductors represent the primary windings while the green are the secondary windings.
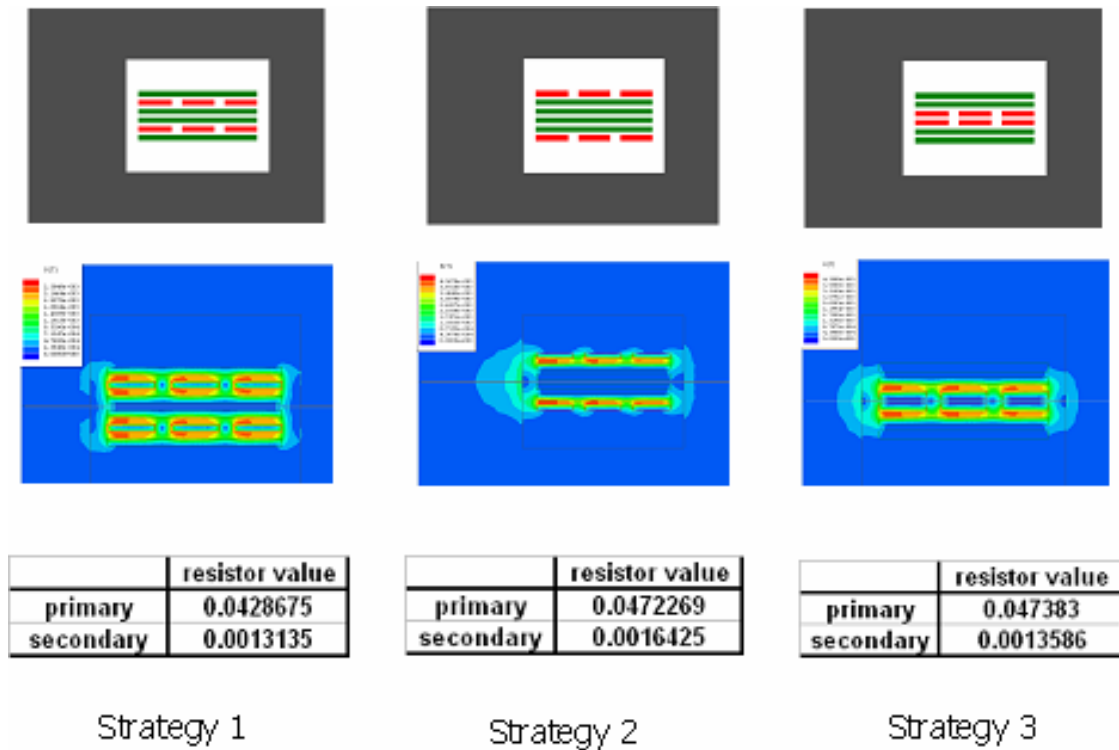
Fig. 3.5 Interleaved winding strategy

Using Maxwell 2D simulation software, current distributions for above four structures are illustrated respectively. It can be seen that the current distributes more uniformly in the interleaved arrangements than that in non-interleaving structure. Maxwell 2D simulation results also present the high-frequency copper resistance value in different winding strategy. The simulated results show that interleaving primary and secondary windings can dramatically improve the current distribution and therefore reduce the AC copper loss. The winding resistor value indicates that the loss for interleaving strategy 1 is the best one among the three interleaving structures.

It should be noted that the effect of winding terminations and connections in the transformer is neglected in Maxwell 2D simulations. To accurately calculate the AC loss in transformer

windings, it is desirable to simulate the conduction losses from 3-dimensional point of view. Maxwell 3D simulation can accurately compute the AC winding losses and further optimize the interleaving winding arrangements. Fig. 3.6 shows the 3D model of the multi-layer PCB planar transformer. It is always time-and-memory-consuming to do 3D simulations, but the result is more accurate.
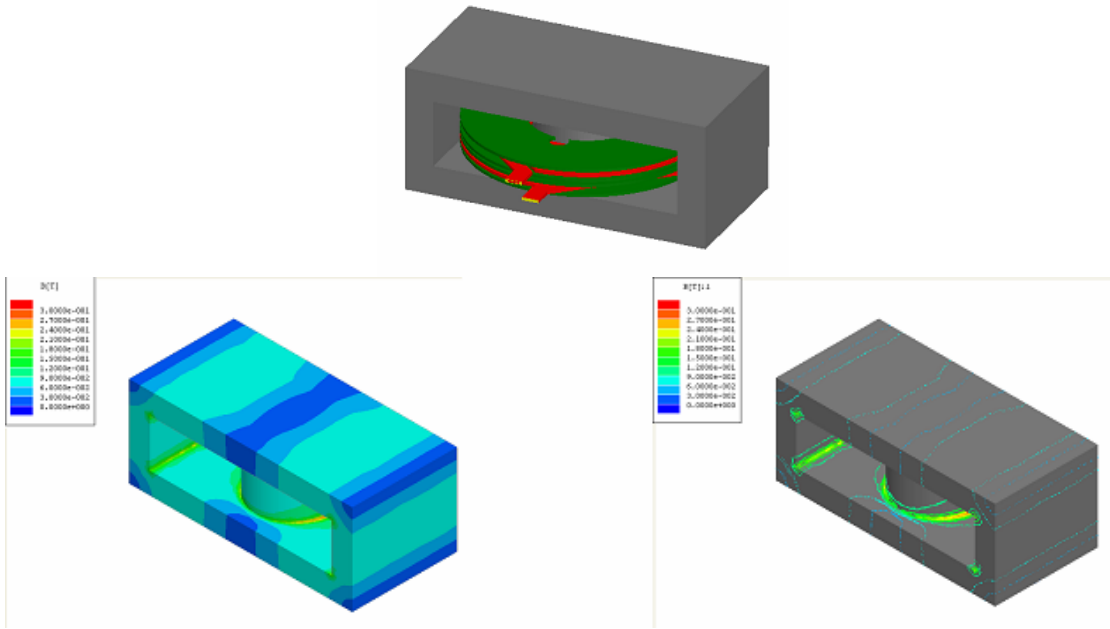
Fig. 3.6 3D model and simulation result of an interleaved planar transformer in Maxwell 3D

The Maxwell 3D simulation result clearly shows that the flux density distribution and magnitude meet the design requirements. The preliminary design results of multi-layer PCB transformer are summarized in as follows:

Core: ER14.5

Material: 3F35

Winding Strategy:
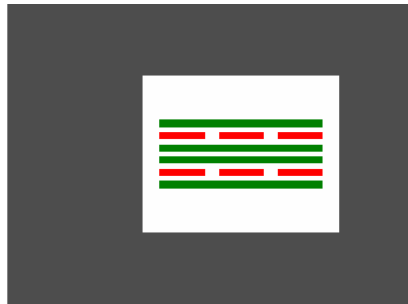
Fig. 3.7 Planar Transformer winding strategy

3.1.2 Design of Planar Filter Inductor

There are obvious incentives for converters to operate at higher frequencies. Converters operating at high frequencies require significantly smaller inductance values and therefore smaller magnetic components. However, as the frequencies increase, core loss and winding losse may also dramatically increase and higher switching frequencies do not always result in the expected size reduction.

3.1.2.1 Specifications

The inductor design specifications are as below:

Circuit Input voltage: 36~75V

Output voltage: 1.0V

Output power: 30W

Switching frequency: 500 KHz

Inductor height: 0.2 in

Applied current: 15 A+ AC Ripple

3.1.2.2 Selection of Core Shape and Material

Magnetic component design generally involves a tradeoff between the reduction of core loss and the increasing of winding loss or vice versa. The loss characteristic of the magnetic material itself presents a fundamental limitation on core loss reduction so that the intrinsic reduction of core loss density depends on magnetic material improvements. Desirable characteristics of magnetic cores for power inductors and transformers can be summarized as follows: first, high saturation flux in order to obtain high saturation current; second, high permeability to obtain high inductance; third, high resistivity to reduce eddy current loss.

For power inductor, the air gap is needed in the core. The traditional air gap calculation equation for inductor is shown:

$$L = \frac{\mu_0 A_E N^2}{l_g} \tag{10}$$

Here, l_g is the gap length and A_E is the effective cross sectional area of the core. If the fringing effects at the gap and the permeability of the core are considered, the more accurate air gap length and inductance equations are:

$$l_g = \frac{NI_M + \frac{D(1-D)V_{in}T_s}{2NA_L} - B_{max}\frac{l_e}{\mu_0\mu_r}}{\frac{B_{max}}{\mu_0\eta} - B_{max}\frac{1}{\mu_0\mu_r} - \frac{D(1-D)V_{in}T_s}{2NA_Ll_e}\left(\frac{\mu_r}{\eta}-1\right)} \tag{11}$$

34

$$L = \frac{A_L N^2}{\left(\frac{\mu_r}{\eta} - 1\right)\frac{l_g}{l_e} + 1}$$

(12)

Here,

μ_0 : Permeability of free space

μ_r : Relative permeability of the material

l_e : Effective magnetic path length of the core

η : Core's cross section area correction parameter for fringing effect (between 1.05 and 1.1)

A_L : Inductance factor without the air gap (provided by manufacturer)

B_{max} : Maximum operating flux density selected for the design

By investigating some commercial cores, core ER9.5 is chosen and 3F35 is core material. The specification of 3F35 is shown in Fig. 3.8.

3F35 SPECIFICATIONS

A medium to high frequency power material for use in power and general purpose transformers at frequencies of 0.5 - 1 MHz.

	CONDITIONS	VALUE	UNIT
μ_i	25 °C; ≤10 kHz; 0.1 mT	1400±20%	
μ_a	100 °C; 25 kHz; 200 mT	≈ 2400	
B	25 °C; 10 kHz; 250 A/m	≈ 450	mT
	100 °C; 10 kHz; 250 A/m	≈ 370	
P_v	100 °C; 400 kHz; 50 mT	≈ 60	kW/m³
	100 °C; 500 kHz; 50 mT	≈ 90	
	100 °C; 500 kHz; 100 mT	≈ 700	
ρ	DC; 25 °C	≈ 10	Ωm
T_C		≥ 240	°C
density		≈ 4750	kg/m³
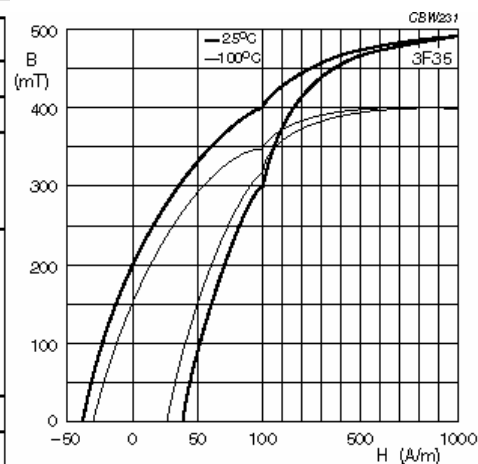
Fig. 3.8 3F35 Specifications (www.ferroxcube.com)

35

3.1.2.3 Winding Layout with Loss Simulations

PCB structures are utilized to fabricate planar windings. In this design, there are also several layers paralleled together for one turn because of the high current. To increase the inductance value and decrease the current ripple, there are two turns for this inductor.
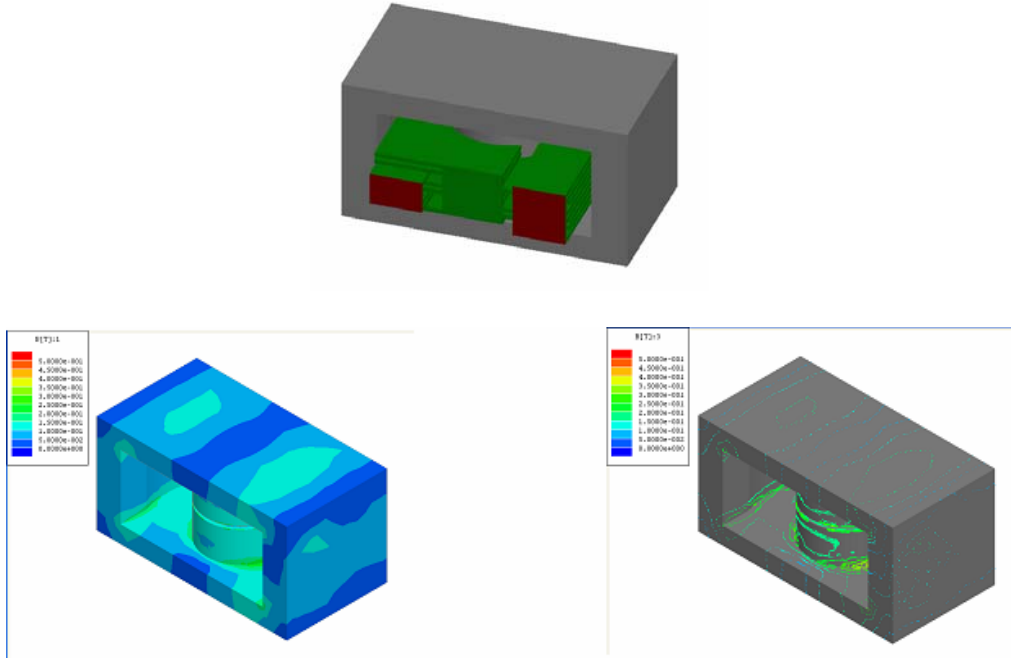
Fig. 3.9 Inductor 3D Model and Simulation Results

The Maxwell 3D simulation result clearly shows that the flux density distribution and magnitude meet the design requirements. The design result of inductor is as follows:

Core: ER9.5

Material: 3F35

Winding Strategy: every four layers paralled and then connected in serial

3.1.3 Simulation and Experimental Results

3.1.3.1 Circuit Model

The traditional two-winding transformer model is shown in Fig. 3.10. The primary winding resistance is represented by R_p, the leakage inductance by L_{lk}, magnetizing inductance by L_m, core loss by R_c, and self-capacitance by C_p. The secondary winding resistance is R_s, the secondary self-capacitance is C_s, and cross capacitance between primary and secondary is C_m. The parameters in this model can be used for characterizing components and identifying circuit simulation. However, this simple model is complicated because all of the resistors and inductors of the model are nonlinear functions of either frequency, or excitation level, or both. The capacitors also exhibit minor nonlinearities, but they are further complicated by a very crude approximation to the multiple inter-winding capacitance effects that really exist in the component.
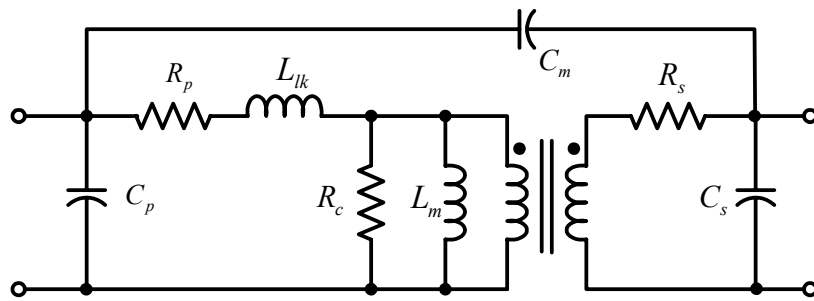
Fig. 3.10 Traditional two-winding transformer model

Fig. 3.11 is the secondary open and short-circuited measurement results, two impedance curves are drawn. The open-circuit measurement gives the primary resistance, magnetizing

37

inductance, and capacitance (via the resonant frequency). Normally, the magnetizing inductance is treated as a constant value over working frequency range. In fact, it varies significantly due to material variations, temperature and frequency. The short-circuit measurement gives the secondary resistance and leakage inductance which will significantly influence the circuit performance. At very low frequencies or DC situation, we can directly measure the primary dc resistance. Beyond that low frequency, the value of the primary and reflected secondary resistance can be measured from the primary terminals. When frequency is above certain value, the short circuit impedance rises due to an increase in AC resistance. From the impedance curve, real and imaginary parts of the impedance are separated out and the value of each of these parameters can be extracted.

Fig. 3.11 Transformer primary impedance curve

Because the leakage inductance will cause ringing in the circuit at high frequencies, so it is important to know the value at the ringing frequency in order to be able to design a proper snubber. There is an industry rule that it is often quoted: "The leakage inductance should be 1% of magnetizing inductance for a transformer." In real design example, with the tightly coupled

windings, the leakage can be less than 0.2% of magnetizing inductance at kilo Hz, and 0.1% at mega Hz.

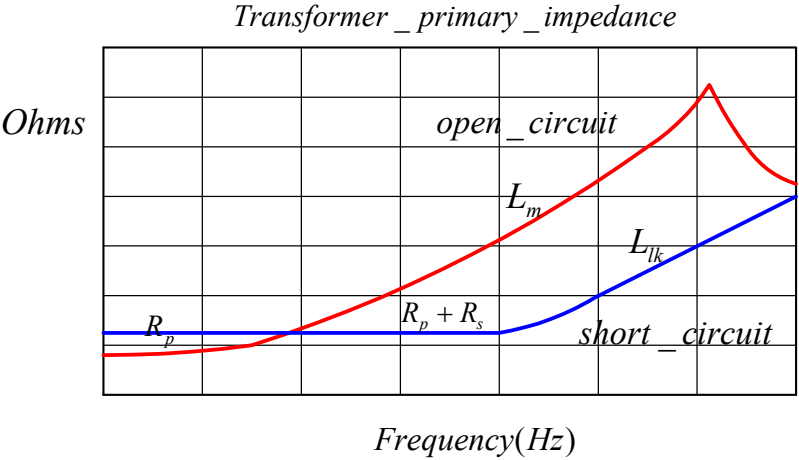All these information are derived from the extended frequency response measurements on transformers. How to get these parameter values before we have the real components becomes an issue. In addition, when there are several magnetic components or there are multi windings in one core, the accurate and simple circuit model is needed for circuit analysis and evaluation before we have the real magnetic components.

For conventional circuit simulation, the magnetics model is constructed using the simple transformer and inductor model. This method omits the frequency dependent feature of the magnetics component. The method also omits parasitic effect of the component. In this design, a CAD design methodology is proposed and Maxwell 3D FEA simulation is adopted. From the 3D simulation, the parameter matrix is extracted. This matrix includes the frequency influence and parasitic effect. The design procedure is as follows:

CHAPTER 2: Using FEM to do the EM field analysis for magnetics components;

CHAPTER 3: Extracting impedance matrix from the FEM simulation result;

CHAPTER 4: Generating converter specified model parameters;

CHAPTER 5: Constructing circuit model and applying the model to the converter design.

The physical structure model of the discrete magnetics structure is shown in Fig.3.12.
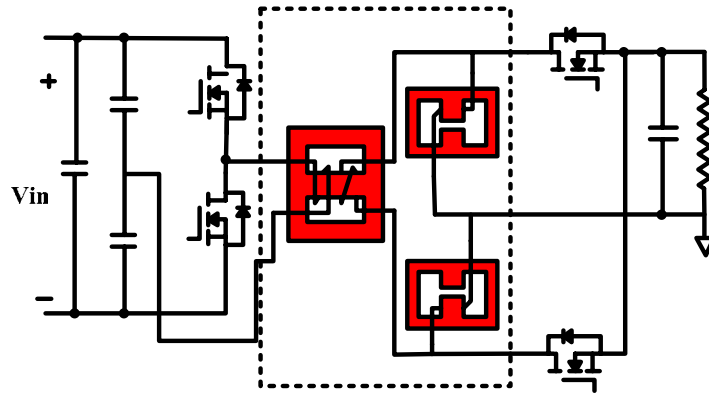
Fig. 3.12 Physical structures of discrete magnetics

From the FEA simulation results, the impedance matrix is derived:

Table 3.1 Discrete Structure Parameter Matrix

	P		S		L1		L2	
	Resistor (ohm)	Inductor (H)	Resistor (ohm)	Inductor (H)	Resistor (ohm)	Inductor (H)	Resistor (ohm)	Inductor (H)
P	0.043869	6.76E-5	-0.00193	-1.13E-5	0	0	0	0
S	-0.00193	-1.13E-5	0.001157	1.88E-6	0	0	0	0
L1	0	0	0	0	0.006872	2.27E-5	0	0
L2	0	0	0	0	0	0	0.006872	2.27E-7

The whole magnetics structure can be treated as 3 port circuit network when it referred to other part of the converter circuit. So, the 4x4 matrix is changed to 3x3 matrix. The Pspise model is constructed from the 3x3 matrix. In this model, the H block is used to model the mutual resistance and the k parameter is used to model the coupling among the different windings.
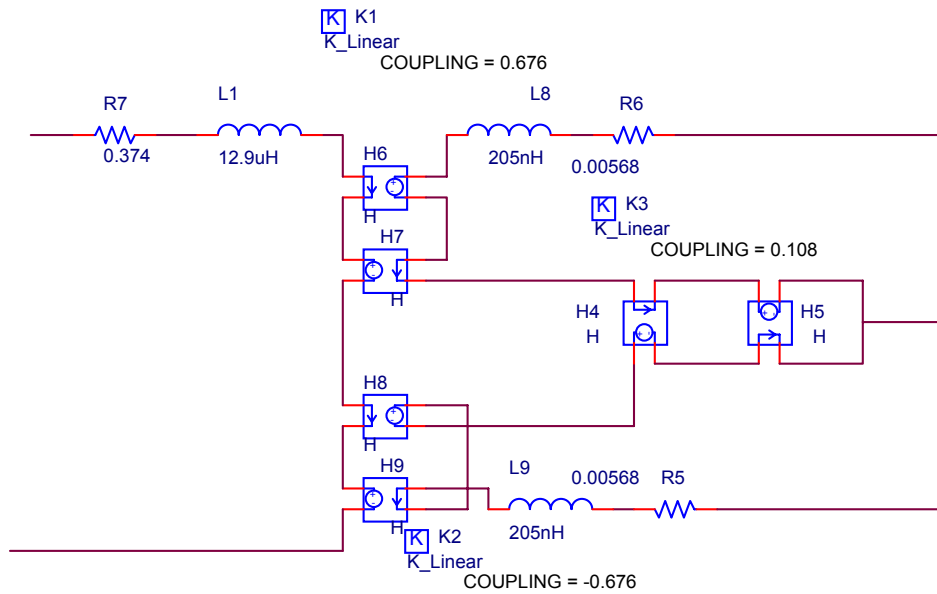
Fig. 3.13 Pspise model of the discrete magnetics structure

3.1.3.2 Simulation Results

Putting the magnetics component model into the Pspise whole circuit model, the simulation results are shown in Fig. 3.14.
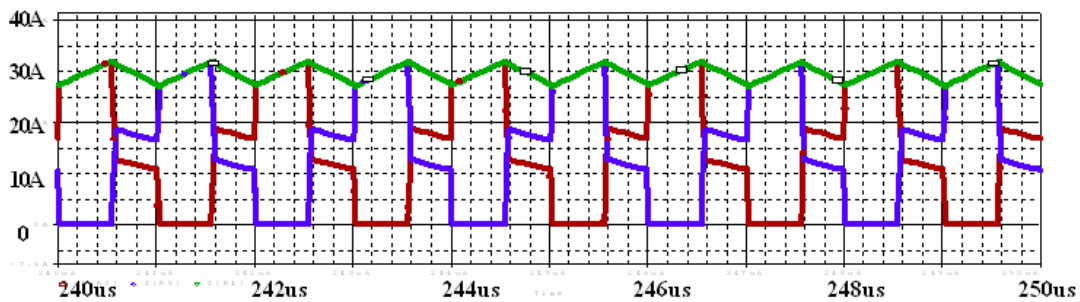
Fig. 3.14 Secondary current waveform of the whole circuit w/o clamp

To decrease the current ringing and increase the efficiency, the active clamp is added in the primary side. The current waveform is following:

41
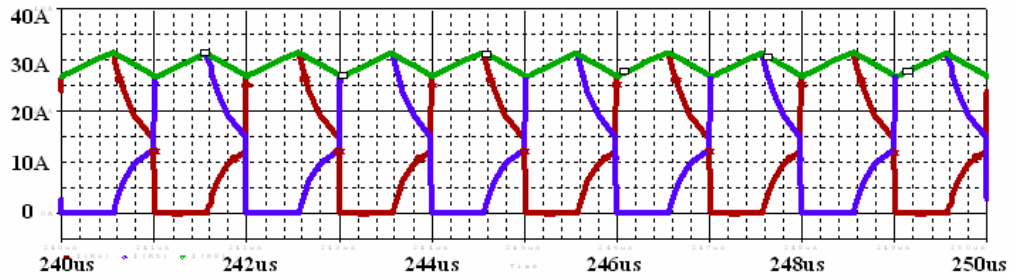
Fig. 3.15 Secondary current waveforms w clamp
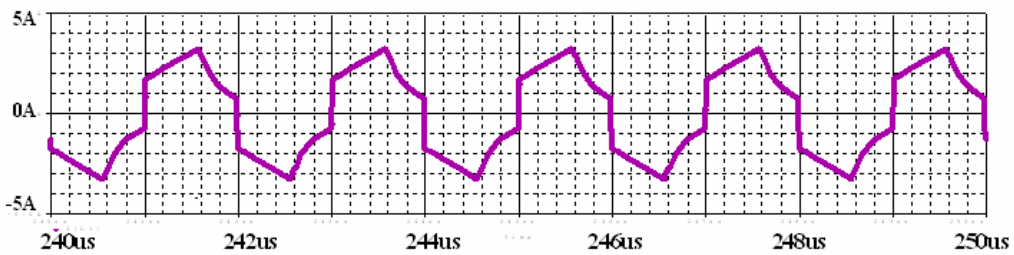
Fig. 3.16 Primary current waveform w clamp

Because the model parameters are frequency-dependant and include the parasitic effect, the simulation results are more accurate. This point is shown clearly in the next section.

3.1.3.3 Experimental Results

Experiment circuit board is shown in Fig. 3.17. It is shown very clearly that the footprint of the magnetics components occupies almost 25% of the whole area.
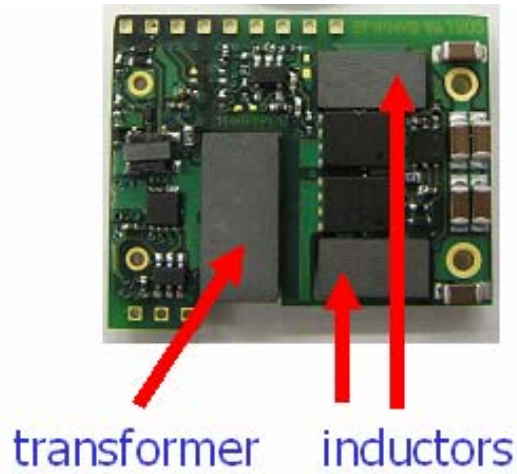
Fig. 3.17 Experiment board

Fig. 3.18 and Fig. 3.19 are the experimental results of the primary voltage and current waveform. Fig. 3.20 is the simulation result of the primary voltage and current waveform. The two results are almost same. This means the magnetics component model is accurate.
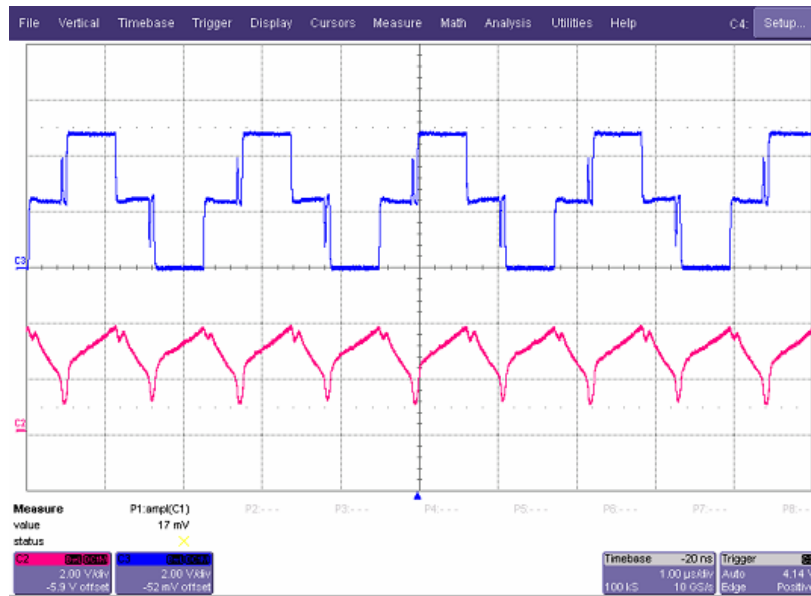
Fig. 3.18 Primary voltage and current waveform

43
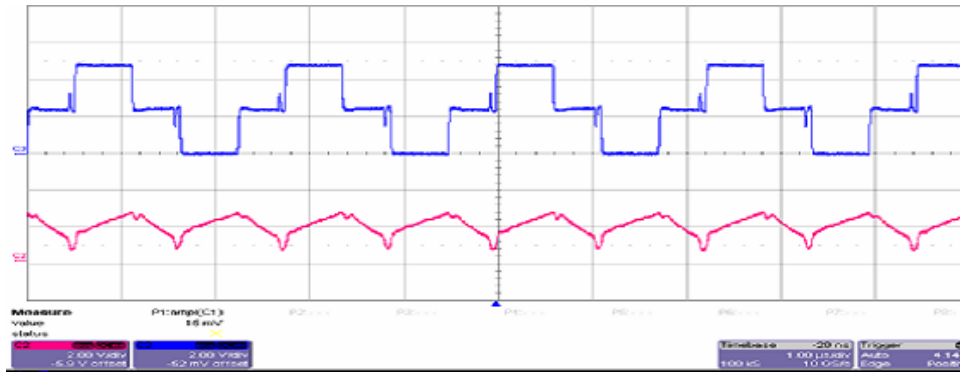
Fig. 3.19 Primary voltage and current waveform after rectify
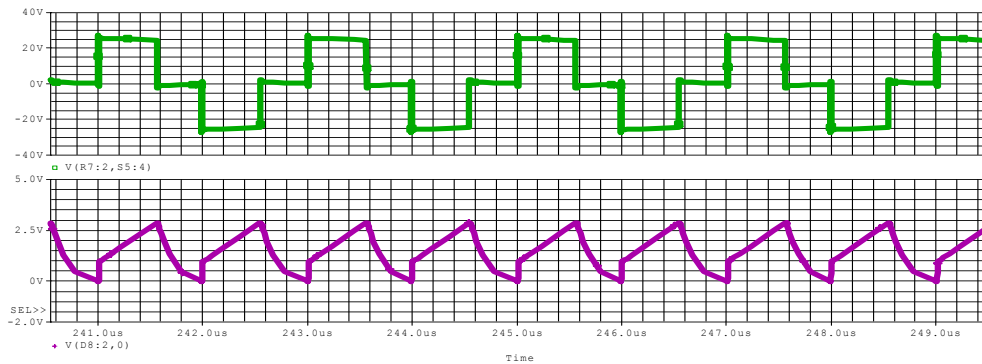
Fig. 3.20 Simulation primary voltage and current waveform after rectify

3.1.4 Volume Optimization

In current distributed power system (DPS) applications, there are increasing demands on high-power-density, low-profile, and high-efficiency front-end dc/dc converters. In most cases, the overall size and volume of front-end DC/DC converters are primarily determined by the size and volume of the passive components and the interconnections between them. Lots of efforts

44

have been made in the past few years to reduce the footprint and profile of the passive components.

The total loss can be approximately divided into two parts: the core loss and the winding loss, assuming that the loss factor of the insulation materials, as well as volume of leakage layer magnetic materials is small, so that the losses in those materials can be neglected. The AC winding loss modeling for transformers and inductors has been a research topic for many years. The finite-element model (FEM) is believed to be more accurate than the 1-D analytical models provided in [38]-[43]. However, in order to reduce the calculation error to an acceptable level by using the FEM method, a long computation time is always needed, making the iterative optimal design procedure time consuming and almost impractical. On the other hand, the 1-D model is very time effective and can give an acceptable result as long as the conditions for the 1-D approximation can be well satisfied. For the passive components, the winding conductor thickness is always less than or equal to the skin depth of the conductor at the fundamental frequency, while it is also much smaller than the conductor width. The windings are also always placed far away from the air gap. This implies that the fringing effects and edge effects can be neglected in this structure. After these conditions are satisfied, the 1-D winding loss model is used in the volume optimization.

$$
\begin{aligned}
i(t) &= I_0 + \sum_{j=1}^{\infty} \sqrt{2} I_j \cos(j\omega t) \\
\varphi_j &= \sqrt{j}\varphi_1 \\
P_j &= I_j^2 R_{dc} \sqrt{j}\varphi_1 \sum_m Q_m \\
P_{cu} &= I_0^2 R_{dc} + \sum P_j
\end{aligned}
\tag{13}
$$

For PWM converters, the excitation current is normally a square wave. The effects of harmonics have to be taken into account. The Fourier series is shown in equation 13.

Because of the interleaving arrangement of the windings, the MMF of each layer will be changed. At last, the power loss will be different for different layer.
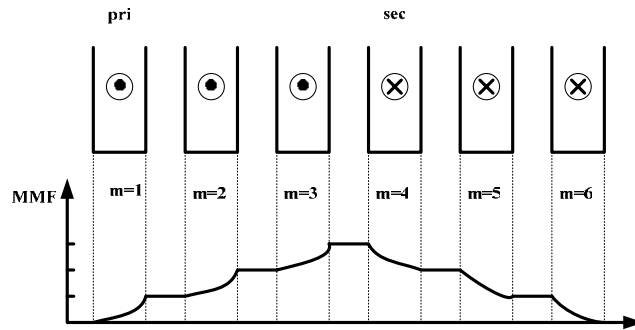
Fig. 3.21 MMF of non interleaving transformer
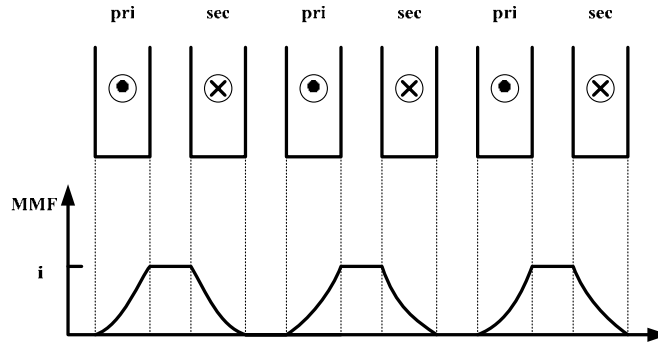
Fig. 3.22 MMF of interleaving transformer

The Fig.3.21 and Fig.3.22 show how the winding arrangement will influence the MMF.

After two parameters have been defined:

$$\eta = \frac{l_w - insulation}{l_w} \qquad\qquad (14)$$

$$\delta' = \frac{\delta}{\sqrt{\eta}} \qquad (15)$$

$$\varphi = \frac{h}{\delta'} = \sqrt{\eta}\frac{h}{\delta} \qquad (16)$$

The power loss in each layer can be calculated:

$$
\begin{aligned}
P &= I^2 R_{dc}\varphi Q'(\varphi,m) \\
Q'(\varphi,m) &= (2m^2 - 2m + 1)G_1(\varphi) - 4m(m-1)G_2(\varphi) \\
G_1(\varphi) &= \frac{\sinh(2\varphi) + \sin(2\varphi)}{\cosh(2\varphi) - \cos(2\varphi)} \\
G_2(\varphi) &= \frac{\sinh(\varphi)\cos(\varphi) + \cosh(\varphi)\sin(\varphi)}{\cosh(2\varphi) - \cos(2\varphi)}
\end{aligned}
\qquad (17)
$$

The core loss calculation has been discussed before.

After the AC loss model has been obtained, the optimal design program can be developed. The design procedure is an iterative process. The detailed design steps are listed as follows.

1) Specifying all the components parameters from circuit analysis. These parameters are transformer turns ratio, magnetizing inductance, excitation voltage, current waveforms, profile, efficiency, switching frequency, insulation thickness, and clearance distance, etc..

2) Choosing core material based on t the first step result. The design variables include the dimension range of the core, winding current density range, and of winding turns number.

3) Setting up the calculation equations. The target can be power density, profile, footprint, etc., as a function of the constraints and the design variables. In this design, given the efficiency value, the minimal core volume is the design target.

4) Starting the iteration process by changing the core dimensions and calculating the power density of each design. A set of design curves is obtained from the calculation. For one certain winding current density value, an optimal design point could be obtained.

5) Writing down the results after the smallest core volume design is identified.
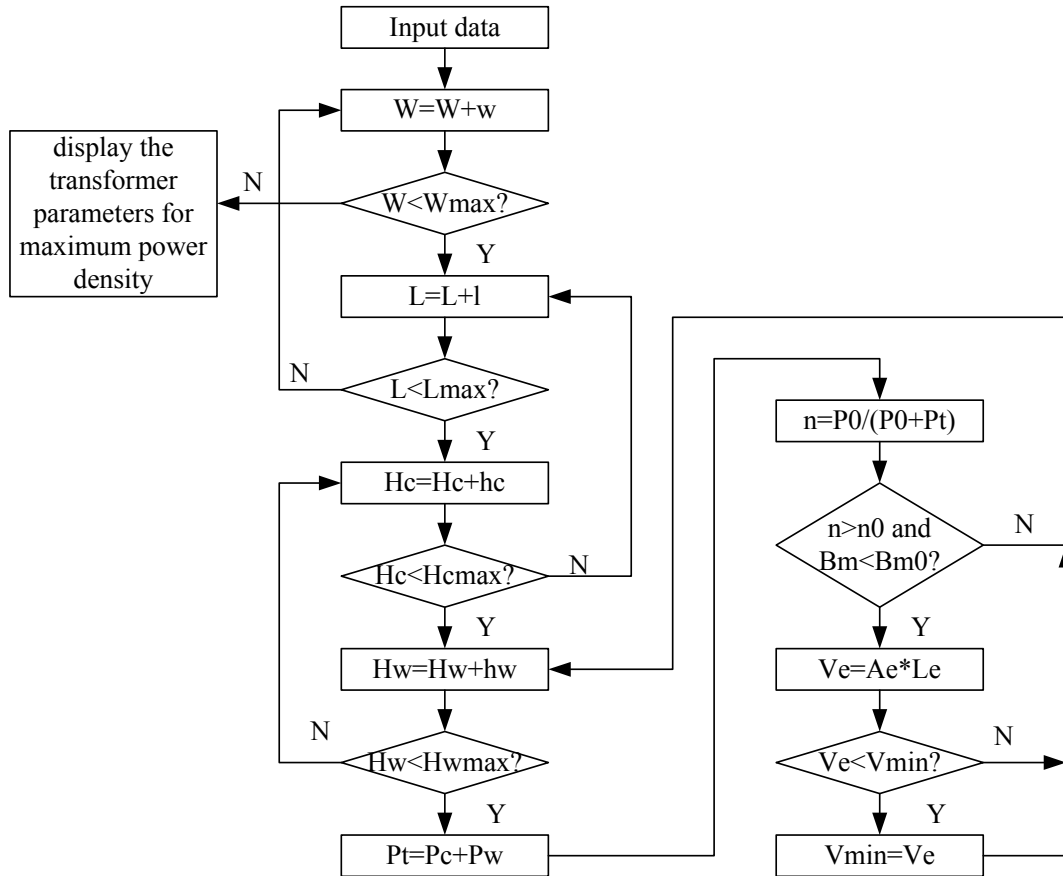
Fig. 3.23 Flow chart of the optimization program

A transformer optimization results are shown in Table 3.2 , Fig. 3.24 and Fig. 3.25.

Table 3.2 Transformer Optimize Result

	100k	200K	300K	400K	500K	600K	700K	800K	900K	1M
width	0.017	0.008	0.005	0.004	0.003	0.003	0.003	0.003	0.003	0.003
length	0.019	0.013	0.012	0.01	0.011	0.009	0.009	0.008	0.008	0.008
hight	0.004	0.004	0.004	0.004	0.004	0.004	0.004	0.004	0.004	0.004
widow hight	0.002	0.002	0.002	0.002	0.002	0.002	0.002	0.002	0.002	0.002
Ve	7.66E-07	2.6444E-07	1.55E-07	1.08E-07	8.72E-08	7.52E-08	7.52E-08	6.92E-08	6.92E-08	6.92E-08
Ae	1.73E-05	8.1951E-06	5.13E-06	4.12E-06	3.08E-06	3.10E-06	3.10E-06	3.11E-06	3.11E-06	3.11E-06
Le	0.044263	0.032268	0.03027	0.026273	0.028271	0.024275	0.024275	0.022277	0.022277	0.022277
Rcenter	0.0032898	0.002257	0.0017841	0.0015958	0.001382	0.001382	0.001382	0.001382	0.001382	0.001382
Bm	0.16191	0.17203	0.1835	0.17203	0.1835	0.15292	0.13107	0.11469	0.10194	0.09175
Ptotal	0.90069	0.90052	0.9094	0.91289	0.90913	0.86993	0.80165	0.9004	0.86655	0.84041
Cu_loss	0.47296	0.47458	0.40821	0.48346	0.3625	0.49784	0.49713	0.66475	0.66435	0.6641
core_loss	0.42783	0.42595	0.50116	0.42943	0.54663	0.37209	0.30452	0.23565	0.20219	0.17631
efficiency	0.98521	0.98521	0.98507	0.98501	0.98507	0.98571	0.98682	0.98522	0.98576	0.98619
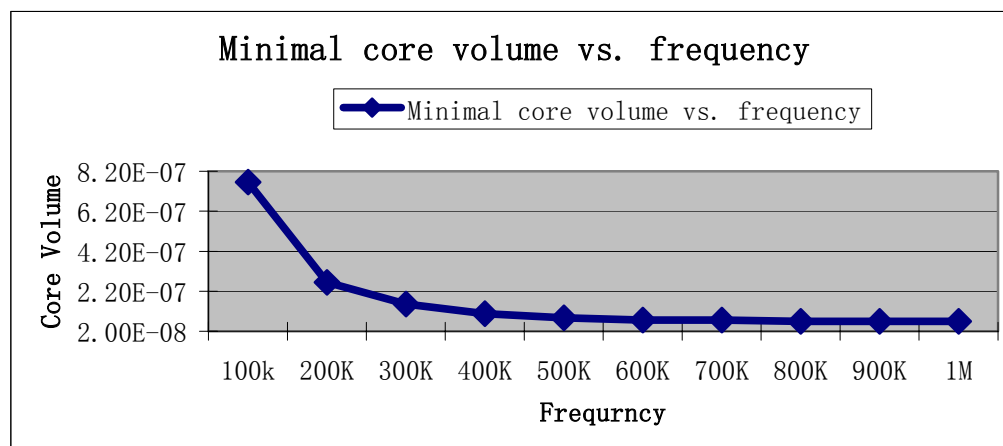
Fig. 3.24 Minimal core volume vs. frequency

When the frequency is increased, under the given efficiency requirement, the core volume can be decreased. Because the copper loss is increased as well, there is an optimized minimal core volume for the given power efficiency.

For the same output power, a higher efficiency normally requires a larger core volume. But when efficiency becomes high, a small increase in efficiency results in big increase in the core volume. So, there is trade off between the efficiency and minimal volume.
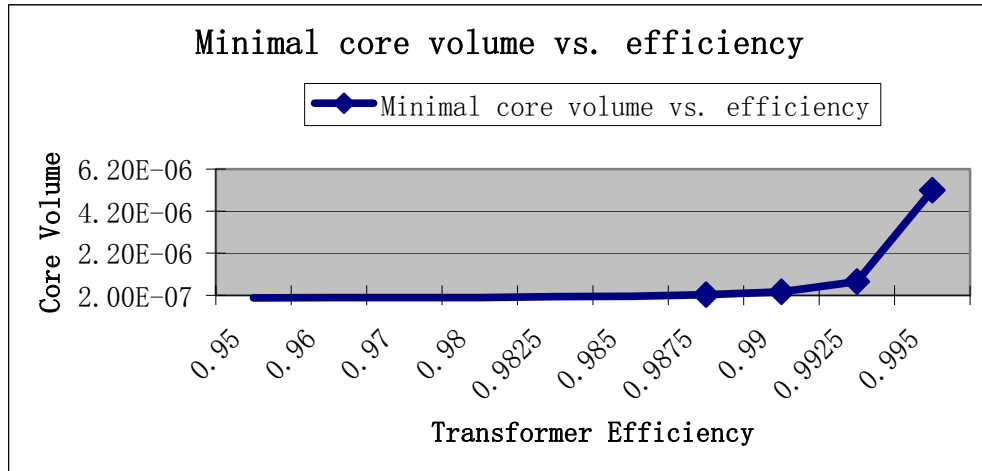
Fig. 3.25 Minimal core volume vs. efficiency

3.2 Active Transient Voltage Compensator Magnetics Design for VRM

3.2.1 High Current and High Slew Rate VRM

The advance of microprocessor technology sets high requirements for the power delivery system. When the number of transistors in the microprocessor increases, the current demand also increases. The supply voltage is expected to decrease to reduce the power consumption. Moreover, the microprocessor's load transient speed is also increased with the increased operating frequency. The low voltage, high current and fast load transition speeds are the

challenges imposed on microprocessor power supplies. When the microprocessor switches between "sleep mode" and "active mode," the current demand of the microprocessor switches between no load and full load. Because of the very high clock speed, the transition process imposes very high current slew rates to the circuit. Active transient voltage compensator (ATVC) [47] is a good solution to the challenging high slew rate load current transient requirement of VRM. ATVC only works in transient periods. At the same time, because the main VR only operates in low frequency in steady period, the efficiency of the VR is high.

In general, transformer is a device which transforms alternating (AC) electric energy from one circuit into another circuit through electromagnetic inductor. Here, the active transient voltage compensator (ATVC) improves transient response through the same basic concept. It is shown in Fig. 3.26: Vinj is the injected voltage source and Rs is the equivalent impedance of ATVC. It only engages into the circuit in transient periods with several MHz operation frequencies, while the main VR operates at low frequency (several hundred KHz) for good efficiency. In this application, a transformer has been adopted to work as the Vinj voltage source. The circuit injects or absorbs the high slew rate current through the transformer. The transient current value is mainly determined by the transformer leakage inductance value. At the steady state, the voltage source is removed from the circuit. In the steady state working mode, the transformer just works as a big filter inductor [47].
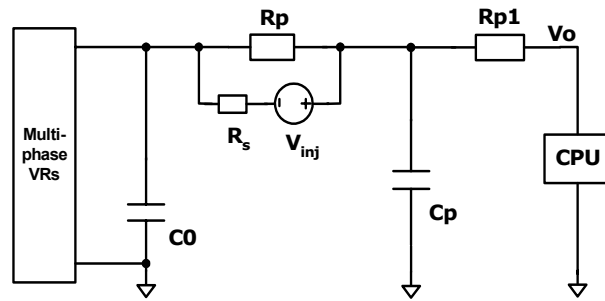
Fig. 3.26 Power delivery structure: (a) initial CPUs power delivery structure and (b) the current

For the ATVC, the transformer is an important component. Because of the DC bias current (inductor), high frequency (MHz) and the high slew rate load current, the design of the transformer is a key issue in the ATVC design. The turns- ratio and the leakage inductance value of the transformer will influence the current slew rate. When the transformer works as an inductor, an air gap is needed to keep the core from the saturation. The air gap length will influence the transformer leakage inductance values. On the other hand, every parameter is frequency dependant. The small change of the parameters will introduce big difference to the transient response. Instead of the normally simple magnetic circuit analysis, the FEM (finite element method) analysis is adopted. The frequency dependent transformer parameters are extracted from the frequency dependent impedance matrix directly. This model is useful for the design of whole VRM circuit.

3.2.2 Transformer Working Modes

The transformer working modes are analyzed first to make things clear. How the parameter values influence the circuit performance is also analyzed. The whole AVTC implement circuit is

shown in Fig. 3.27. There are five parameters in this two winding transformer model. The idea transformer turns ratio is $N:1$. The secondary side of the transformer is paralleled to the main VR circuit and the primary side is connected to the MOSFET. In this figure, R_{LM} is the transformer equivalent resistance value; L_M is the transformer magnetizing inductance value; L_{lk1} and L_{lk2} are the leakage inductance of each transformer winding; i_M is the transformer magnetizing current value; i_{ATVC} is the transformer total injected current; i_{LK1} and i_{LK2} are the value of each transformer winding's current.
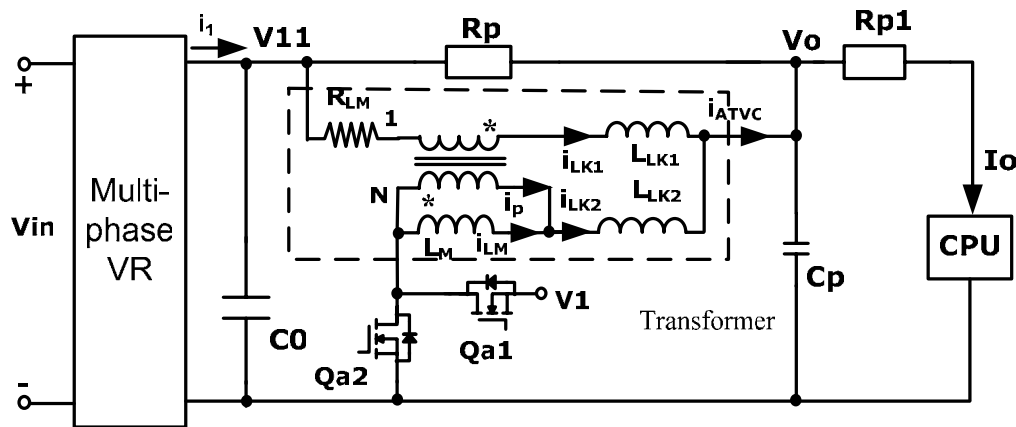
Fig. 3.27 ATVC implementation circuit

There are three working modes for this transformer:

Buck circuit state:

Qa1 is on, Qa2 is off and transformer works at high frequency (MHz). The microprocessor switches from "sleep mode" to the "active mode". This is the step up load.

Because of the $\omega L \gg R_{LM}$, we can omit the resistor in the theory analysis. The transformer primary voltage can be simplified as

$$V_1 - V_0 = L_{LK2} \cdot \frac{di_{LK2}}{dt} + L_M \cdot \frac{di_{LM}}{dt} \qquad (18)$$

The transformer secondary voltage is given as

$$V_{11} - V_0 = L_{LK1} \cdot \frac{di_{LK1}}{dt} - \frac{L_M}{N} \cdot \frac{di_{LM}}{dt} \qquad (19)$$

The voltage drop between the V11 and V0 is near zero. So that

$$L_M \cdot \frac{di_{LM}}{dt} = N \cdot L_{LK1} \cdot \frac{di_{LK1}}{dt} \qquad (20)$$

Because of the idea transformer, we can assume $i_{LM} \approx 0$ and $i_P = \frac{i_{LK1}}{N} \approx i_{LK2}$.

Then it can be yielded

$$V_1 - V_0 = N^2 \cdot L_{LK1} \cdot \frac{di_{LK2}}{dt} + L_{LK2} \cdot \frac{di_{LK2}}{dt} \qquad (21)$$

From the equation (21), when the voltage value is settled, the leakage inductance value of each winding will decide the current slew rate value. The transformer total injects current can be expressed as

$$\frac{di_{ATVC}}{dt} = (1+N) \cdot \frac{di_{LK2}}{dt} + \frac{di_{LM}}{dt} \qquad (22)$$

Steady state:

Qa1 is off, Qa2 is off and transformer works as an inductor. The transformer works as a filter inductor. The filter inductance value is equal to transformer secondary winding's self inductance value.

$$I_{ATVC} \approx \frac{R_P}{R_P + R_{LM}} \cdot I_1$$

(23)

I_{ATVC} is the output DC current. From this value, the air gap length can be decided. In this working mode, the transformer total output current equals the transformer secondary current. The main VRM circuit works in the low frequency (KHz) instead of transient high frequency (MHz). At the same time, the large filter inductor means the small current ripple. The high efficiency of the whole converter can be achieved.

Boost circuit state:

Qa1 is off, Qa2 is on and transformer works at high frequency. This is step down load.

The transformer primary voltage is given by

$$-V_0 = N^2 \cdot L_{LK1} \cdot \frac{di_{LK2}}{dt} + L_{LK2} \cdot \frac{di_{LK2}}{dt}$$

(24)

The transformer total absorbs current is

$$\frac{di_{ATVC}}{dt} = (1+N) \cdot \frac{di_{LK2}}{dt} + \frac{di_{LM}}{dt}$$

(25)

The equations also show that the transformer leakage inductance values will determinate the transient slew current value. Designing the transformer with suitable parameters value is the main task of the whole design.

3.2.3 Transformer Model

For the conventional approaches, magnetic components are often designed based on magnetic equivalent circuit models. The core loss and conduction loss in magnetic devices are roughly estimated. However, with the increase in the switching frequency, it becomes difficult to apply the traditional analysis to evaluate the power losses caused by skin effect and proximity effect [48]. Furthermore, the leakage inductance value has a big impact on the whole circuit performance [49]. From the working modes which is explained before, it is very important to know the leakage inductance value of each transformer winding. This cannot be calculated just from the normal transformer open circuit and short circuit model. In the steady state, the transformer works as an inductor. The air gap is needed to keep the magnetic core from saturation. When the turns-ratio is small, the value ratio between the magnetizing inductance and leakage inductance is small. The open circuit is not suitable to decide the magnetic inductance value. The new model is needed to derive each winding's leakage inductance and the transformer magnetizing inductance value. Ansoft Maxwell 3D software is adopted to design the transformer. The Maxwell 3D is the FEM numerical method. It begins from electrical magnetic field FEM analysis and simulation. The skin effect, proximity effect and parasitic parameters are all included in the simulation. The simulation result is accurate and frequency dependent. The impedance matrix of the component can be extracted from the electrical magnetic field simulation results directly.

In this design, the magnetic core ER11 from Philips is used for the transformer to reduce the whole volume of the converter.

56
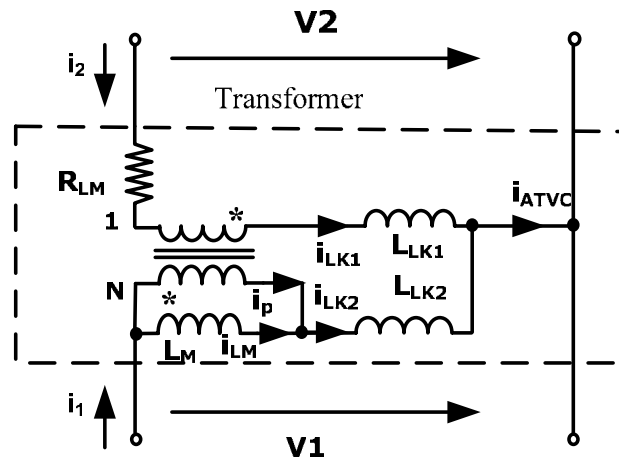
Fig. 3.28 Transformer model

The transformer model is shown in Fig. 3.28. The model includes an idea transformer, the leakage inductance of each winding and one effective resistor. Here, it should be noted that the magnetic component is called transformer just because the current waveforms are same as a real transformer. From the energy point, it works like two strong coupled inductors.
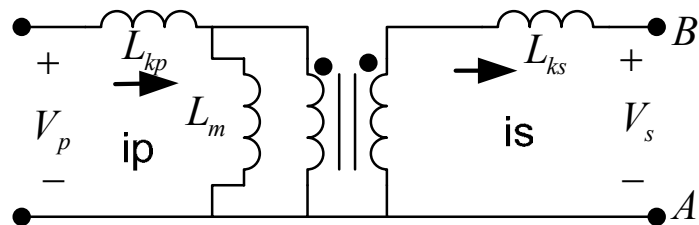
Fig. 3.29 Traditional transformer model

Fig. 3.29 is the traditional transformer mode. On the primary side, the reference directions of the voltage and current are same and they are as same as the real direction. So, the primary side of the transformer absorbs the energy from the source. On the secondary side, the directions of the voltage and current are different. The transformer sends the energy out to the load. From the

energy point, the transformer can only transfer the energy. Because of the leakage inductance, there is small energy stored in the core.
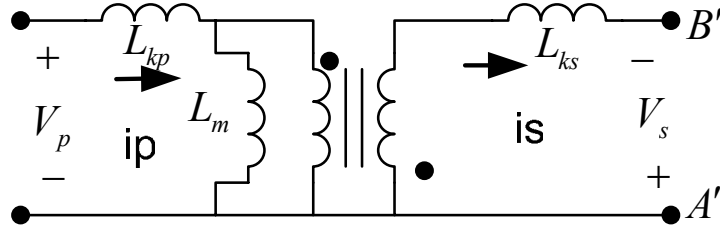
Fig. 3.30 Inverse transformer model

Fig. 3.30 is what we called the inverse transformer in this design. The reference voltage direction for the secondary side is different from the traditional one. The secondary side absorbs the energy too. So, from the energy point, it is strongly coupled inductors and stores the energy. But, because the current waveforms are same as the real transformer, we call it "inversed transformer".

In this model, the transformer is analyzed as a two ports network. From the Maxwell 3D simulation, the accurate and frequency-dependable impedance matrix of this model can be calculated. In the matrix, the real part is the resistor value and the imagery part is the inductance value. They have been automatically separated. To calculate the inductance value, we only need to consider the imagery part of the impedance matrix.

The equation of the network can be written explicitly as

$$\begin{pmatrix} V_1 \\ V_2 \end{pmatrix} = \begin{pmatrix} z_{11} & z_{12} \\ z_{21} & z_{22} \end{pmatrix} \cdot \begin{pmatrix} i_1 \\ i_2 \end{pmatrix}$$

(26)

From the two ports circuit, the secondary voltage is presented as

$$V_2 = \omega L_{LK1} \cdot i_{LK1} - \frac{1}{N} \cdot \omega L_M \cdot i_{LM}$$

$$= \omega L_{LK1} \cdot i_2 - \frac{1}{N} \cdot \omega L_M \cdot \left(i_1 - i_p \right)$$

$$= \omega L_{LK1} \cdot i_2 - \frac{1}{N} \cdot \omega L_M \cdot \left(i_1 - \frac{1}{N} \cdot i_2 \right)$$

$$= -\frac{1}{N} \cdot \omega L_M \cdot i_1 + \left(\omega L_{LK1} + \frac{1}{N^2} \cdot \omega L_M \right) \cdot i_1 \tag{27}$$

and the primary voltage is given by

$$V_1 = \omega L_{LK2} \cdot i_{LK2} + \omega L_M \cdot i_{LM}$$

$$= \omega L_{LK2} \cdot i_1 + \omega L_M \cdot \left(i_1 - i_p \right)$$

$$= \omega L_{LK2} \cdot i_1 + \omega L_M \cdot \left(i_1 - \frac{1}{N} \cdot i_2 \right)$$

$$= \left(\omega L_{LK2} + \omega L_M \right) \cdot i_1 - \omega L_M \cdot \frac{1}{N} \cdot i_2 \tag{28}$$

When compared with the Maxwell 3D impedance matrix result, the matrix equation can be simplified to

$$\mathrm{Im} \begin{pmatrix} z_{11} & z_{12} \\ z_{21} & z_{22} \end{pmatrix} = \begin{pmatrix} L_{LK2} + L_M & -\frac{1}{N} \cdot L_M \\ -\frac{1}{N} \cdot L_M & L_{LK1} + \frac{1}{N^2} \cdot L_M \end{pmatrix} \tag{29}$$

From the equation (29), the transformer magnetizing and leakage inductance value can be calculated. Same as the Maxwell 3D FEM numerical result, the inductance value is accurate and frequency dependent. The most important thing for the ATVC is that the leakage inductance value for each winding can be shown clearly in the model. This is useful for the whole VR

circuit analysis and simulation. Through the same method, from the real part of impedance matrix, the effective resistor value R_{LM} can be calculated.

3.2.4 Simulation Result

The ATVC circuit requirements are: setting less resistor value to decrease the power loss and increase the efficiency; setting less leakage inductance to improve the transient response and making tradeoff between the switch loss and transient response.

The Maxwell 3D software is used to perform the detail simulation. According to the transformer circuit model, we can decide the turns-ratio, air gap length and operating frequency of the transformer for ATVC. From the equations (22) and (25), an effective leakage inductance is defined as:

$$L_{leakge} = N^2 \cdot L_{LK1} + L_{LK2}$$
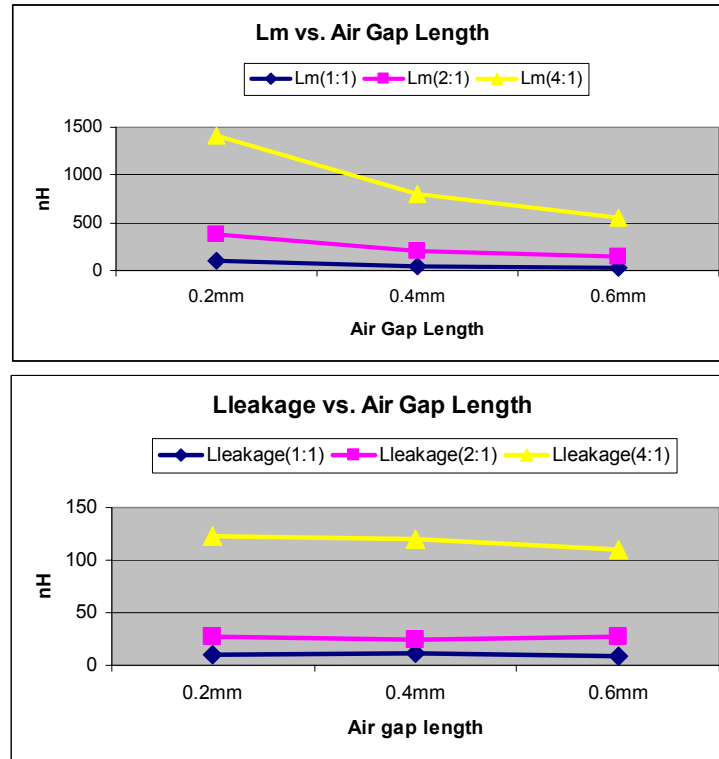
Fig. 3.31 Inductance values vs. air gap length

When the air gap is increased, the magnetizing inductance value decreases a lot and the effective leakage inductance just changes a little. To keep the magnetizing inductance value far larger than leakage inductance value and keep leakage inductance value small, the air gap length 0.2mm is enough.

Because the transformer works as the inductor in the steady state, the flux density distribution with the certain air gap length is checked to keep transformer from saturation when it works as a filter inductor.

Turns ratio 1:1   Turns ratio 2:1
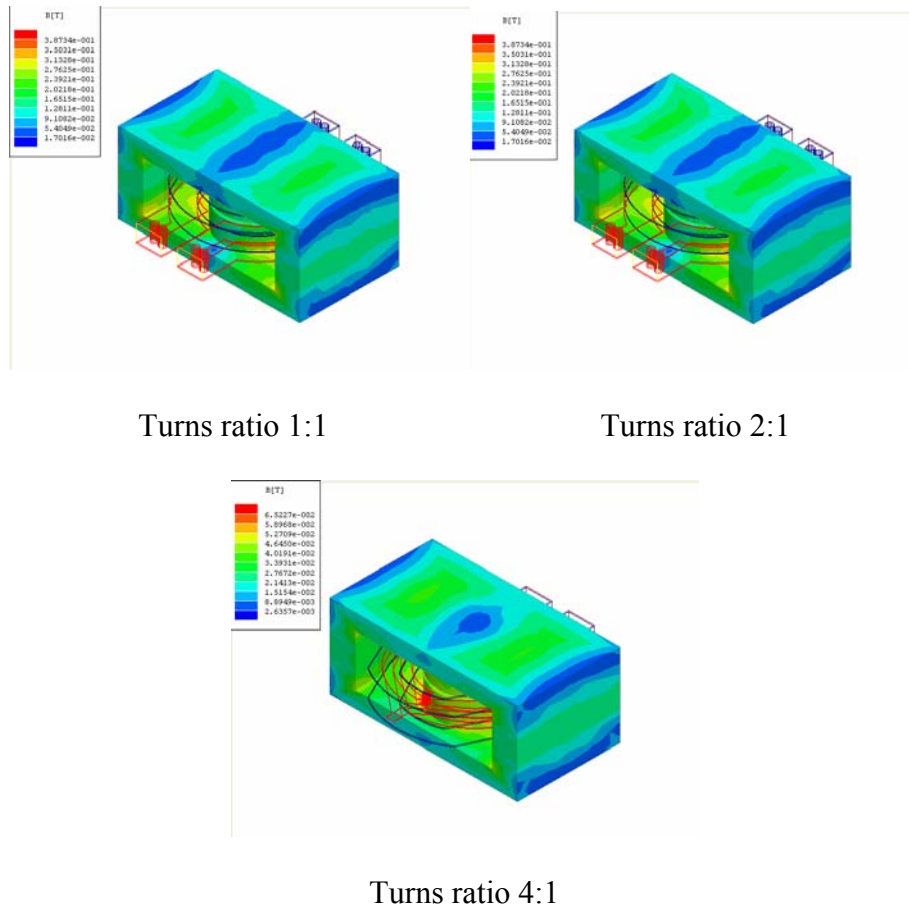
Turns ratio 4:1

Fig. 3.32 Flux density distributions for different turns-ratio

From the simulation results of flux density distribution which are shown in Fig. 3.32, ER11 core with different turns- ratio meets the flux density requirements.

When the frequency is increased, for different turns-ratio, the magnetizing inductance almost stays constant and the leakage inductance increases a little. For better efficiency during the transient period, the frequency 1.5MHz is identified.
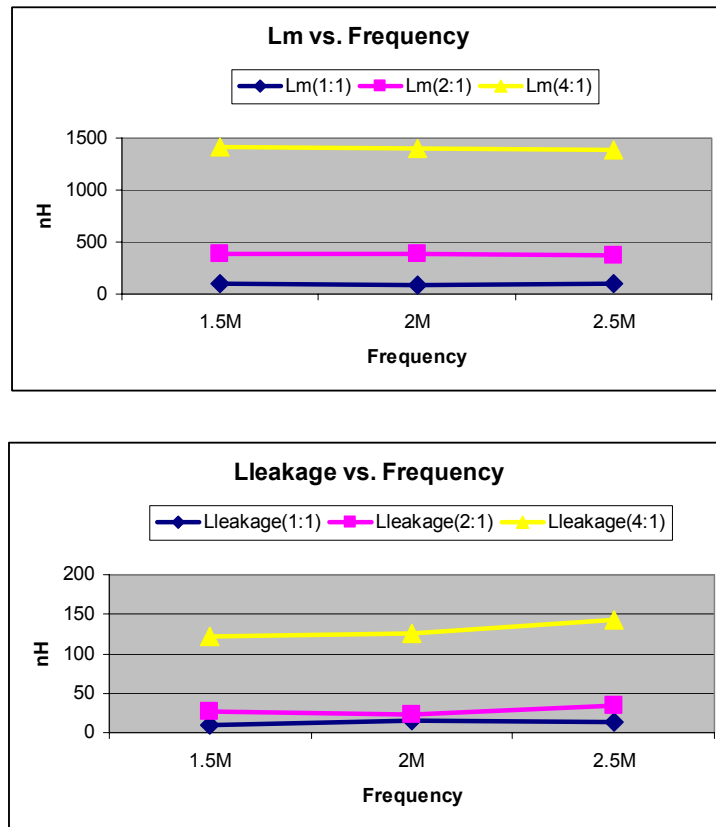
Fig. 3.33 Inductance values vs. frequency

When the transformer turns-ratio is increased, the magnetizing inductance and the leakage inductance are both increased. For the better efficiency and better transient response, the turns-ratio 2:1 is adopted.
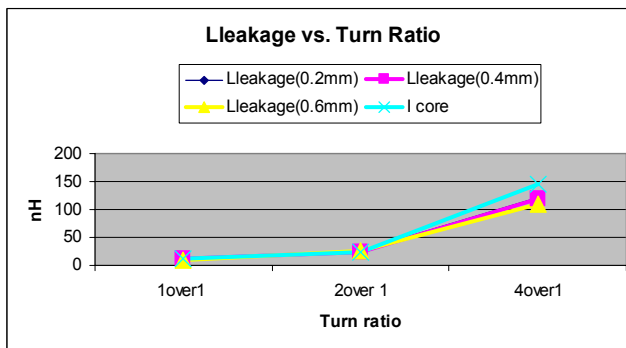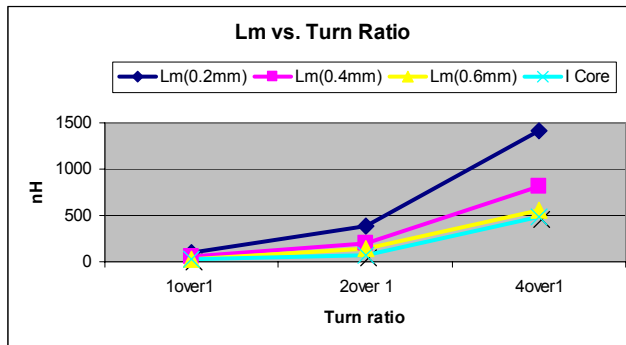
Fig. 3.34 Inductance values vs. turns-ratio
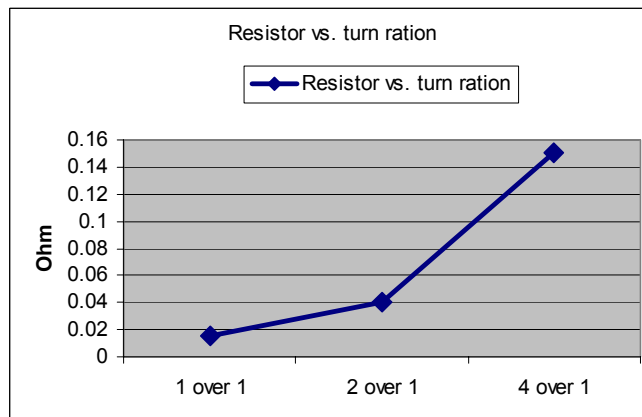
Fig. 3.35 Resistor vs. turns-ratio

When the turns-ratio is increased, the effective resistor value is also increased if the core size is settled.

64

According to the simulation results, the transformer with the switching frequency 1.5 MHz, 2:1 turns-ratio and 0.2mm air gap length is chosen. In this design, the effective leakage inductance value is 26.5 nH and the magnetizing inductance is 382 nH. The core size is ER11 and the core material is 3F35.
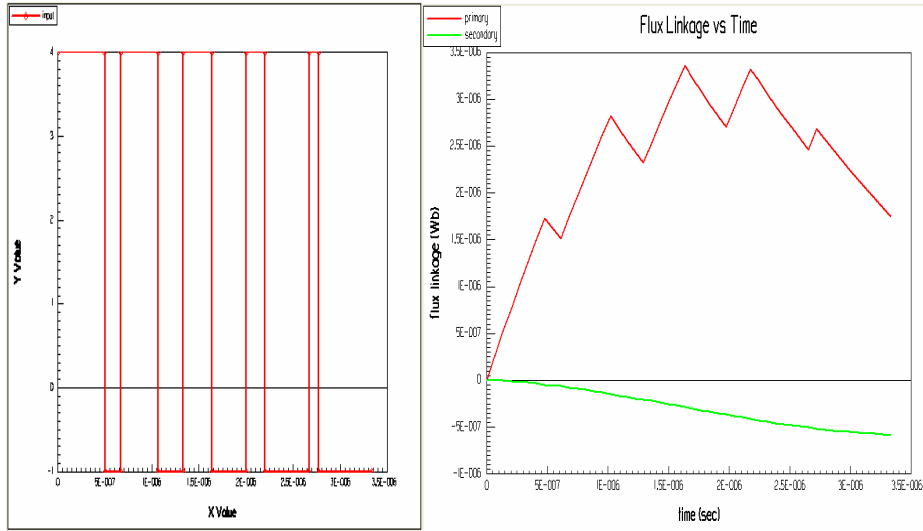
(1) Input voltage for the transformer   (2) Flux linkage waveform
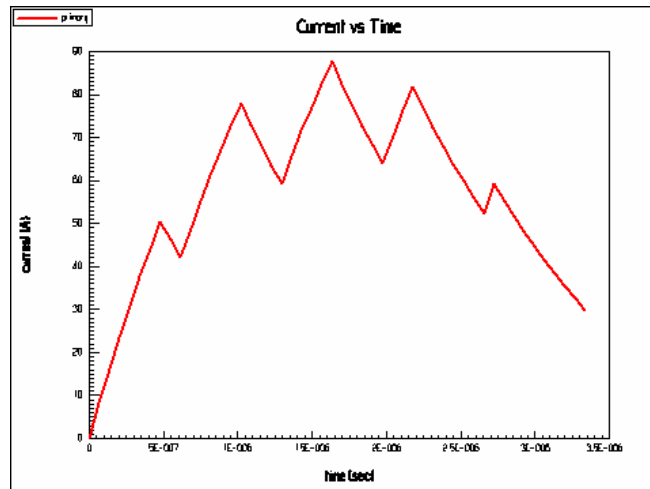
(3) Transformer current waveform

Fig. 3.36 Maxwell 3D transient simulation results

Because of the high frequency (MHz), the eddy current effects in the winding and core have to be in consideration. At the same time, because the core's permeability changes with frequency and flux density, all of these will affect the performance of ATVC [50]. The Maxwell 3D transformer transient simulation is a good way to understand the transformer transient working performance. In the transient simulation, the actual voltage is added to the Maxwell 3D model of the magnetic component. In Fig. 3.36, the transient flux linkage waveform distributed in the core and transformer transient winding current waveform are given. From the simulation results, it is clear that the transformer transient current slew rate can reach 0.12A/ns.

3.2.5 Experiment Verification

Using the procedure introduced above, a transformer has been designed. A two channel VRM [53] and ATVC prototype was built to verify the design. It is shown in Fig. 3.37. The main VRM switching frequency is 300 KHz and the ATVC operating frequency is 1.5 MHz.
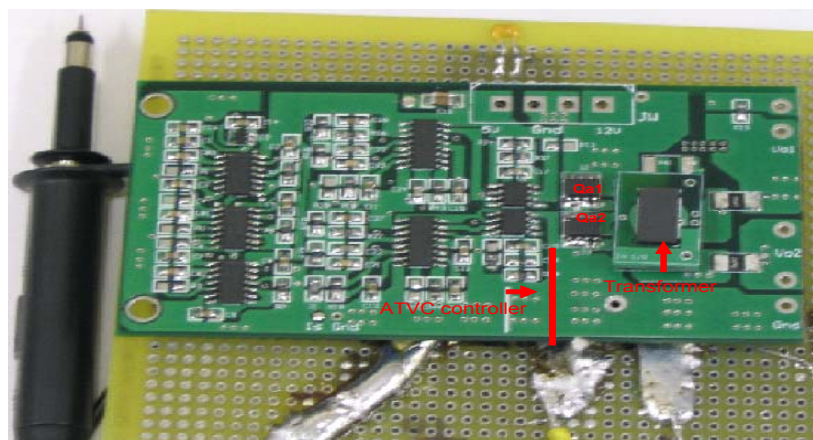
Fig. 3.37 Experiment prototype

66

VRM experimental results without and with ATVC are shown in Fig. 3.38 and Fig. 3.39 separately. The load current is switched between 1A and 25A. We can see that the VRM with ATVC has better transient response. The transient current can catch the load current quickly.
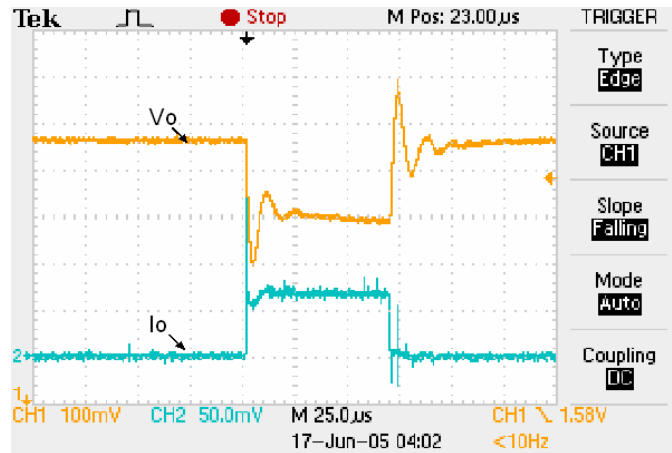
Fig. 3.38 VRM experimental results without ATVC
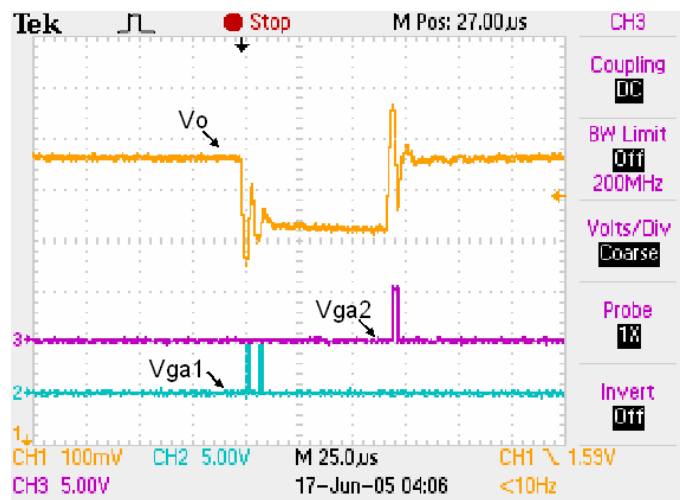
Fig. 3.39 VRM experimental results with ATVC.

67

When the load is increased suddenly, the transformer injects current to the circuit. When the load is decreased suddenly, the transformer absorbs current from the circuit. From the experimental waveform, it is clear that the transformer design can satisfy the ATVC circuit requirement. The ATVC transient current slew rate can reach 0.11A/ns.
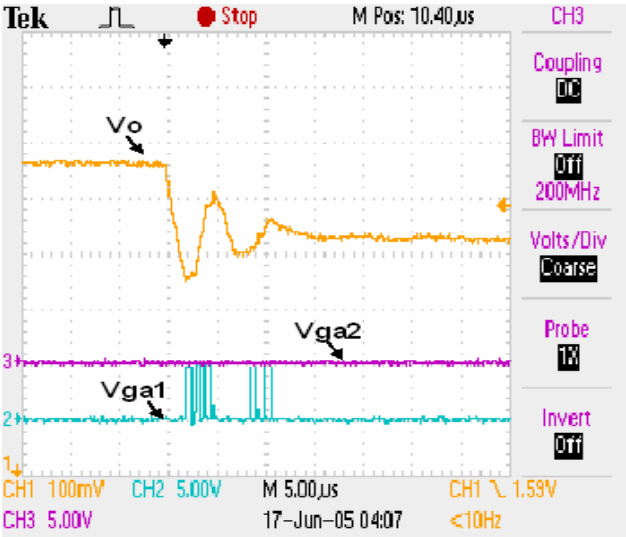
Fig. 3.40 Step down detail waveform, VRM and ATVC work together
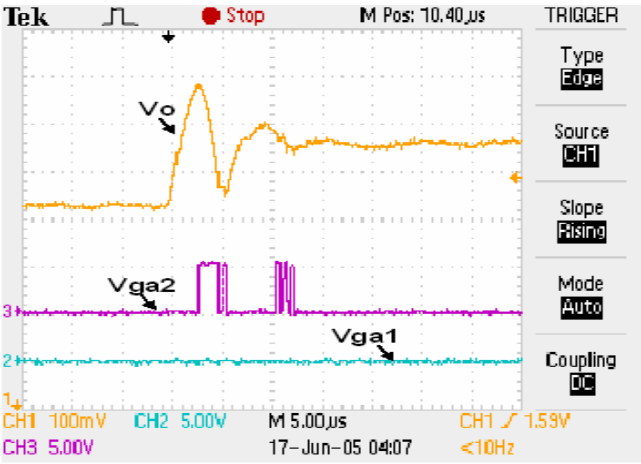
Fig. 3.41 Step up detail waveform, VRM and ATVC work together

Fig. 3.40 and Fig. 3.41 are detailed waveforms and MOSFET gate signal in ATVC. The two MOSFETs are turned on at different time periods according to different working conditions. The experimental results verify the intuitive magnetics components design for high current and high slew rate application in VRM.

CHAPTER 4: INTEGRATED MAGNETICS

4.1 Coupled Inductors

Current-doubler topology is presented in the literature as a possible solution to decrease the power losses in the transformer secondary side windings of the full-wave buck-derived converters, such as push-pull, half-bridge [68], [69] and full-bridge [70], [71]. In comparison to conventional center-tapped topology, current-doubler topology can reduce the losses by approximately 50%. The penalty for the improvement is an additional inductor. This inconvenience can be partially alleviated by integrating both inductors on a common core. Integration without magnetic coupling of the windings was discussed in [68] and [71]. Compared with the discrete structure, integrated structure has smaller effective filter inductance value. For the discrete couple inductor structure, there is only one inductance value which has limited working range. In the [72], three coupled inductor structures are compared and analyzed. The objective is to search the zero ripple condition when the inductors have identical voltage waveform. In [75] and [76], the integrated coupled inductors structure between the channels is proposed to improve both the steady state and dynamic performances with easier manufacturing. But, they all have limited inductance adjustable range.

The electrical schematic and inductor winding arrangement for a Y-shape coupled inductor are shown in Fig. 4.1. The windings located at the out legs are inversely coupled and the turn numbers are same. It has large inductance adjustable range to optimize the inductance value for good circuit performance.

70
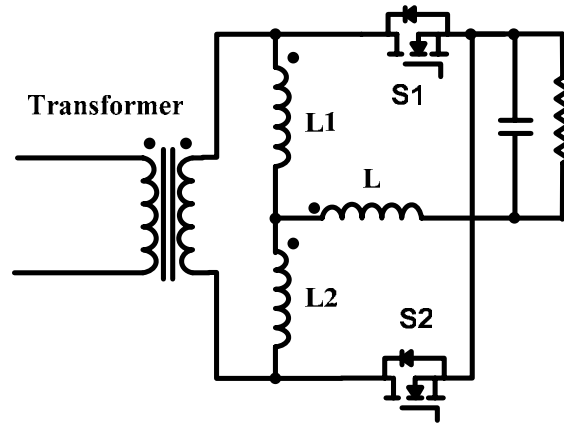
(a) Proposed circuit
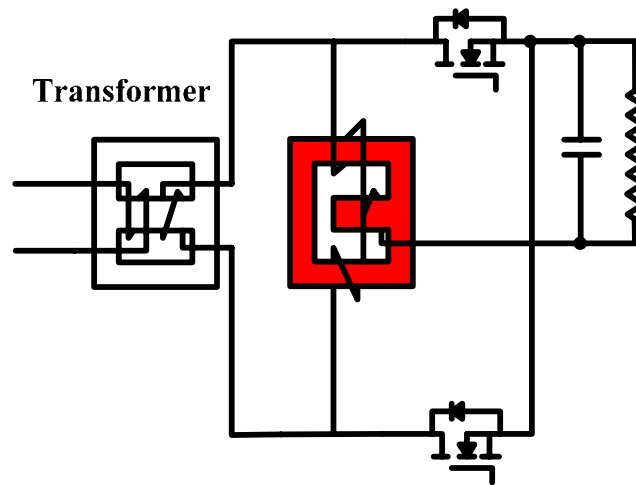
(b) Physical structure

Fig. 4.1 Proposed Y-shape integrated coupled inductor structure

4.1.1 Model Derivation

In Fig. 4.2, the R_0 represents the reluctance of each outer core leg and R_c represents the equivalent reluctance of the center leg. R_c value is normally dominated by the length of the air

gap. In practice, however, the stray field component can strongly influence the R_c value and the calculation of the air gap is difficult. N_L is the out leg winding turn number and N_C is the center leg winging turn number.
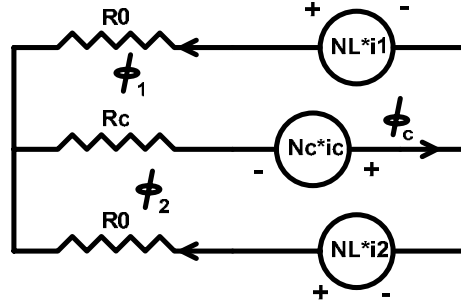
Fig. 4.2 Reluctance model

The flux in each core leg is given by following equation:

$$
\begin{pmatrix} \phi_1 \\ \phi_2 \\ \phi_c \end{pmatrix} = \begin{pmatrix} \dfrac{R_0 + R_c}{R_0^2 + 2R_0 \cdot R_c} & \dfrac{-R_c}{R_0^2 + 2R_0 \cdot R_c} & \dfrac{R_0}{R_0^2 + 2R_0 \cdot R_c} \\ \dfrac{-R_c}{R_0^2 + 2R_0 \cdot R_c} & \dfrac{R_0 + R_c}{R_0^2 + 2R_0 \cdot R_c} & \dfrac{R_0}{R_0^2 + 2R_0 \cdot R_c} \\ \dfrac{R_0}{R_0^2 + 2R_0 \cdot R_c} & \dfrac{R_0}{R_0^2 + 2R_0 \cdot R_c} & \dfrac{2R_0}{R_0^2 + 2R_0 \cdot R_c} \end{pmatrix} \begin{pmatrix} N_L \cdot i_1 \\ N_L \cdot i_2 \\ N_c \cdot i_c \end{pmatrix} \tag{31}
$$

Because of $i_c = i_1 + i_2$, the equation is changed to:

$$
\begin{pmatrix} \phi_1 \\ \phi_2 \\ \phi_c \end{pmatrix} = \begin{pmatrix} \dfrac{N_L \cdot (R_0 + R_c) + N_c \cdot R_0}{R_0^2 + 2R_0 \cdot R_c} & \dfrac{-N_L \cdot R_c + N_c \cdot R_0}{R_0^2 + 2R_0 \cdot R_c} \\ \dfrac{-N_L \cdot R_c + N_c \cdot R_0}{R_0^2 + 2R_0 \cdot R_c} & \dfrac{N_L \cdot (R_0 + R_c) + N_c \cdot R_0}{R_0^2 + 2R_0 \cdot R_c} \\ \dfrac{N_L \cdot R_0 + 2 \cdot N_c \cdot R_0}{R_0^2 + 2R_0 \cdot R_c} & \dfrac{N_L \cdot R_0 + 2 \cdot N_c \cdot R_0}{R_0^2 + 2R_0 \cdot R_c} \end{pmatrix} \cdot \begin{pmatrix} i_1 \\ i_2 \end{pmatrix} \tag{32}
$$

From the magnetic basic equation $v = N \dfrac{d\phi}{dt}$,

72

$$
\begin{pmatrix} v_{L1} \\ v_{L2} \\ v_c \end{pmatrix} = A \cdot \begin{pmatrix} \dfrac{d}{dt} i_1 \\ \dfrac{d}{dt} i_2 \\ \dfrac{d}{dt} i_c \end{pmatrix}
$$

(33)

$$
A = \begin{pmatrix} N_L{}^2 \dfrac{R_0 + R_c}{R_0^2 + 2R_0 \cdot R_c} & N_L{}^2 \dfrac{-R_c}{R_0^2 + 2R_0 \cdot R_c} & N_L N_c \dfrac{R_0}{R_0^2 + 2R_0 \cdot R_c} \\ N_L{}^2 \dfrac{-R_c}{R_0^2 + 2R_0 \cdot R_c} & N_L{}^2 \dfrac{R_0 + R_c}{R_0^2 + 2R_0 \cdot R_c} & N_L N_c \dfrac{R_0}{R_0^2 + 2R_0 \cdot R_c} \\ N_L N_c \dfrac{R_0}{R_0^2 + 2R_0 \cdot R_c} & N_L N_c \dfrac{R_0}{R_0^2 + 2R_0 \cdot R_c} & N_c{}^2 \dfrac{2R_0}{R_0^2 + 2R_0 \cdot R_c} \end{pmatrix}
$$

(34)

$$
\begin{pmatrix} v_1 \\ v_2 \\ v_c \end{pmatrix} = \begin{pmatrix} L_{10} & -M_{12} & M_{1C} \\ -M_{21} & L_{20} & M_{2C} \\ M_{C1} & M_{C2} & L_{C0} \end{pmatrix} \begin{pmatrix} \dfrac{d}{dt} i_1 \\ \dfrac{d}{dt} i_2 \\ \dfrac{d}{dt} i_c \end{pmatrix}
$$

$$
= \begin{pmatrix} L_0 & -M_0 & M_c \\ -M_0 & L_0 & M_c \\ M_c & M_c & L_c \end{pmatrix} \cdot \begin{pmatrix} \dfrac{d}{dt} i_1 \\ \dfrac{d}{dt} i_2 \\ \dfrac{d}{dt} i_c \end{pmatrix}
$$

(35)

Because of the symmetry structure:

$$
L_{10} = L_{20} = L_0 , \; M_{12} = M_{21} = M_0 , \; M_{C1} = M_{1C} = M_{2C} = M_{C2} = M_C
$$

$$L_0 = N_L^2 \cdot \frac{R_0 + R_c}{R_0^2 + 2R_0 \cdot R_c}$$

(36)

$$L_c = N_c^2 \cdot \frac{2R_0}{R_0^2 + 2R_0 \cdot R_c}$$

(37)

$$M_0 = N_L^2 \cdot \frac{R_c}{R_0^2 + 2R_0 \cdot R_c}$$

(38)

$$M_c = N_L N_c \cdot \frac{R_0}{R_0^2 + 2R_0 \cdot R_c}$$

(39)

The coupling coefficients are:

$$k_0 = \frac{M_0}{\sqrt{L_0 L_0}} = \frac{R_c}{R_0 + R_c} = \frac{1}{\alpha + 1}$$

(40)

$$k_c = \frac{M_c}{\sqrt{L_0 L_c}} = \frac{R_0}{\sqrt{2R_0 \cdot (R_0 + R_c)}} = \frac{1}{\sqrt{2 + 2/\alpha}}$$

(41)

In these equations, $\alpha = \dfrac{R_0}{R_c}$ and $0 < \alpha < 1$.

We can see from here: k_0 is between 0.5 and 1 and k_c is between 0 and 0.5.

$$\begin{pmatrix} v_1 \\ v_2 \\ v_c \end{pmatrix} = \begin{pmatrix} L_0 + M_c & -M_0 + M_c \\ -M_0 + M_c & L_0 + M_c \\ L_c + M_c & L_c + M_c \end{pmatrix} \cdot \begin{pmatrix} \dfrac{d}{dt} i_1 \\ \dfrac{d}{dt} i_2 \end{pmatrix}$$

(42)

$$\begin{pmatrix} v_{1e} \\ v_{2e} \end{pmatrix} = \begin{pmatrix} L_0 + L_c + 2M_c & L_c - M_0 + 2M_c \\ L_c - M_0 + 2M_c & L_0 + L_c + 2M_c \end{pmatrix} \cdot \begin{pmatrix} \dfrac{d}{dt}i_1 \\ \dfrac{d}{dt}i_2 \end{pmatrix}$$

(43)

$$v_{1e} = -V_{out} + V_{in+}$$
$$v_{2e} = -V_{out} + V_{in-}$$

(44)

To keep the magnetic core from the saturation, from the view of mechanical stability, there is an air gap located in the center leg and $R_c \gg R_0$. When center leg turns number N_c is small, the $L_c - M_0 + 2M_c < 0$. So, the inversed idea transformer model is used to decouple the inductors. The equivalent circuit model can be constructed in Fig. 4.3. In this model, the leakages inductors are used to mode the effective filter inductors. The leakage inductance value equals to the effective filter inductance value.
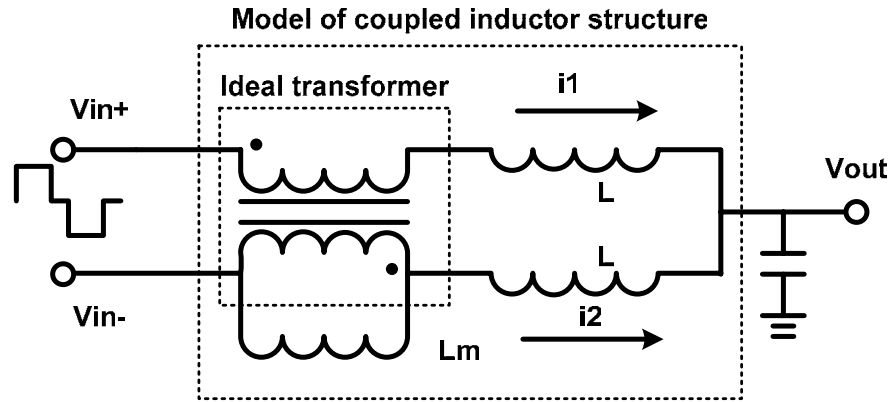
Fig. 4.3 Circuit Model

$$v_{1e} = -L_m \cdot \left(\frac{d}{dt} i_2 - \frac{d}{dt} i_1 \right) + L \cdot \frac{d}{dt} i_1$$

$$v_{2e} = L_m \cdot \left(\frac{d}{dt} i_2 - \frac{d}{dt} i_1 \right) + L \cdot \frac{d}{dt} i_2$$

(45)

In these equations,

$$L = L_0 + 2L_c + 4M_c - M_0$$
$$= (1 - k_0)L_0 + 4k_c \sqrt{L_0 L_c} + 2L_c$$

(46)

$$L_m = -L_c + M_0 - 2M_c$$
$$= -L_c + k_0 L_0 - 2k_c \sqrt{L_0 L_c}$$

(47)

$$\begin{pmatrix} \dfrac{d}{dt} i_1 \\ \dfrac{d}{dt} i_2 \end{pmatrix} = \begin{pmatrix} L_m + L & -L_m \\ -L_m & L_m + L \end{pmatrix}^{-1} \cdot \begin{pmatrix} v_{1e} \\ v_{2e} \end{pmatrix}$$

(48)

We can see from these equations that the effective filter inductance value is controllable for the Y-shape connection. Because the effective inductance value is adjusted by the air gap length and the center leg winding simultaneity, the adjustable range is large. For the two winding coupled inductor structure shown in [76], the inductance value is changed through adjusting the air gap length only. So, the adjustable range and the effective value are small.

4.1.2 Circuit Analysis

There are four working modes for this Y-shape coupled inductor structure when the duty cycle for each inductor winding is less than 0.5.

Mode 1: $[t_0, t_1]$

In this mode, the switch S1 is off and S2 is on.
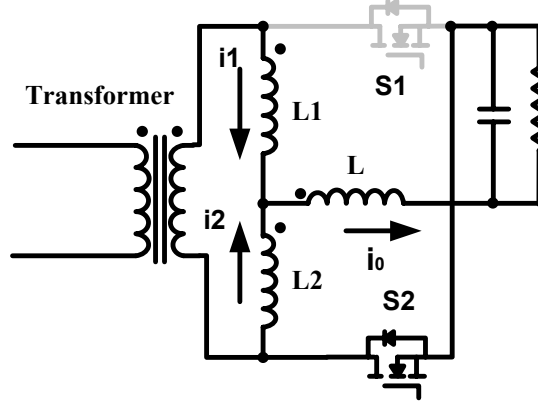
Fig. 4.4 Mode 1 Circuit

In this mode: $v_{1e} = V_{in} - V_0$ and $v_{2e} = -V_0$.

$$\frac{d}{dt} i_1 = \frac{L_m + L}{L^2 + 2 \cdot L_m \cdot L} \cdot V_{in} - \frac{1}{L} \cdot V_0 \tag{49}$$

$$\frac{d}{dt} i_2 = \frac{L_m}{L^2 + 2 \cdot L_m \cdot L} \cdot V_{in} - \frac{1}{L} \cdot V_0 \tag{50}$$

$$\frac{d}{dt} i_0 = \frac{1}{L} \cdot (V_{in} - 2 \cdot V_0) \tag{51}$$

For each winding, the current slope is less than that in the discrete current doubler structure. From this point, the coupled inductor structure is helpful to decrease the current ripple in each winding. At the same time, the output current ripple is also decreased.

Mode 2: $[t_1, t_2]$

77
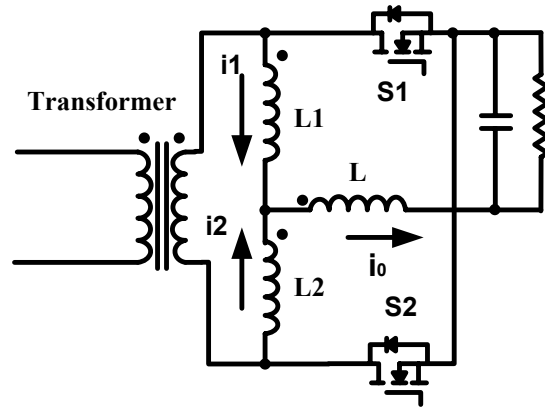
Fig. 4.5 Mode 2 Circuit

In this mode, the switch S1 is on and S2 is on, the circuit is working on free wheeling status.

In this time period: $v_{1e} = -V_0$ and $v_{2e} = -V_0$.

$$\frac{d}{dt} i_1 = -\frac{1}{L} \cdot V_0$$

(52)

$$\frac{d}{dt} i_2 = -\frac{1}{L} \cdot V_0$$

(53)

$$\frac{d}{dt} i_0 = -2 \cdot \frac{1}{L} \cdot V_0$$

(54)

Mode 3: $[\ t_2, t_3\ ]$
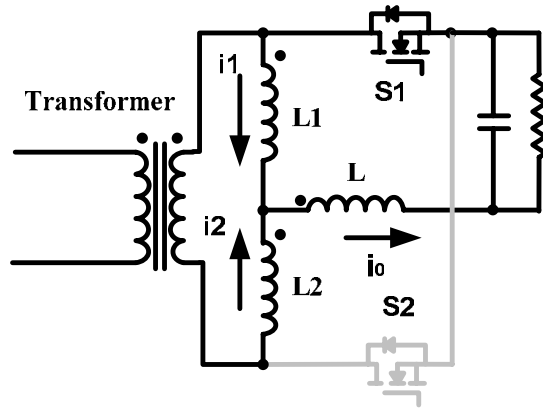
Fig. 4.6 Mode 3 Circuit

In this time period: $v_{1e} = -V_0$ and $v_{2e} = V_{in} - V_0$.

$$\frac{d}{dt} i_1 = \frac{L_m}{L^2 + 2 \cdot L_m \cdot L} \cdot V_{in} - \frac{1}{L} \cdot V_0$$

(55)

$$\frac{d}{dt} i_2 = \frac{L_m + L}{L^2 + 2 \cdot L_m \cdot L} \cdot V_{in} - \frac{1}{L} \cdot V_0$$

(56)

$$\frac{d}{dt} i_0 = \frac{1}{L} \cdot \left(V_{in} - 2 \cdot V_0 \right)$$

(57)

Mode 4: $[t_3, t_4]$

This mode is same as the mode 2, the switch S1 is on and S2 is on. The whole circuit is working on free wheeling status.

The current waveform is shown Fig. 4.7.

79
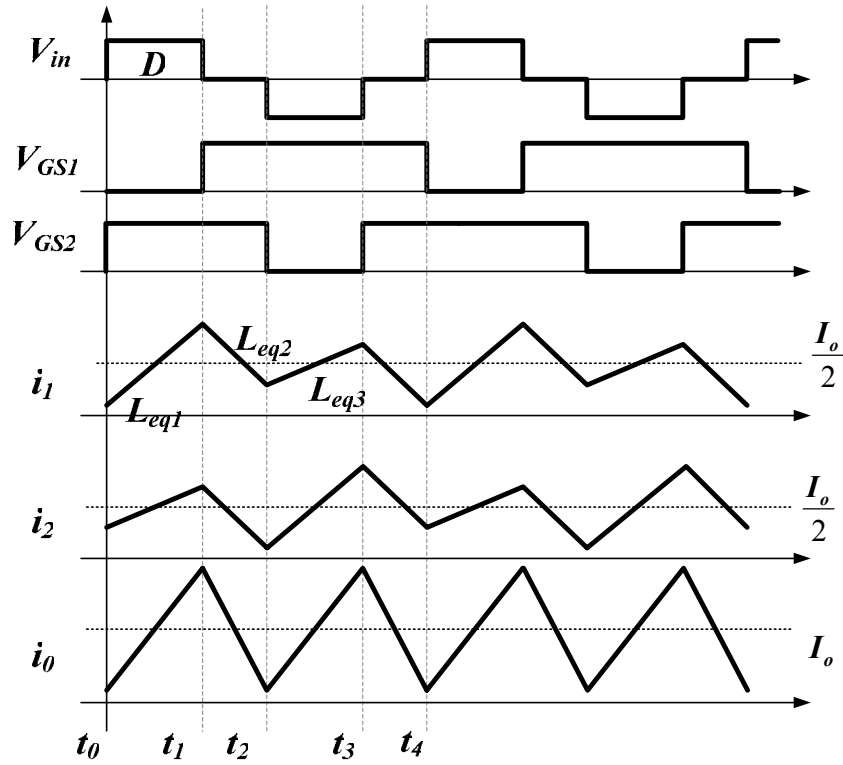
Fig. 4.7 Circuit waveforms

For the uncoupled case, the current ripple for each inductor is:

$$\Delta I_{uncoupled\_L} = \frac{V_0}{L} \cdot (1-D) \cdot T$$

(58)

The current ripple for total output is:

$$\Delta I_{uncoupled\_out} = \frac{V_0}{L} \cdot (1-2D) \cdot T$$

(59)

For the coupled case, from the equations derived before, the current ripple for each winding

is:

$$\Delta I_{coupled\_L} = \left(\frac{L_m + L}{L^2 + 2 \cdot L_m \cdot L} \cdot V_{in} - \frac{1}{L} \cdot V_0 \right) \cdot D \cdot T$$

$$= \left(\frac{1 + \dfrac{L_m}{L}}{1 + 2 \dfrac{L_m}{L}} \cdot \frac{1}{D} - 1 \right) \cdot \frac{V_0}{L} \cdot D \cdot T \tag{60}$$

The current ripple for total output is:

$$\Delta I_{coupled\_out} = \frac{2 \cdot V_0}{L} \cdot (0.5 - D) \cdot T = \frac{V_0}{L} \cdot (1 - 2D) \cdot T \tag{61}$$

So, the total output current ripple is determined by the effective inductance value L. The larger effective inductance value, the smaller current ripple.

If K is defined as the coupling coefficient parameter and:

$$K = \frac{L_m}{L_m + L} \tag{62}$$

In this way the influence of the coupling coefficient on the current-doubler parameters can be conveniently analyzed without affecting the value of inductance. If the current ripple ratio is defined as:

$$P_L = \frac{\Delta I_{coupled\_L}}{\Delta I_{uncoupled\_L}} = \frac{\dfrac{1 + \dfrac{L_m}{L}}{1 + 2 \dfrac{L_m}{L}} - D}{1 - D} = \frac{1 - \dfrac{D}{1 - D} K}{1 + K} \tag{63}$$

Then the each inductor current ripple vs. coupling coefficient is shown in Fig. 4.8. Given different duty cycle, when the coupling coefficient is increased, the current ripple is decreased. Especially when duty cycle equals 0.5, the current ripple will be near zero. The strong coupling means small current ripple.
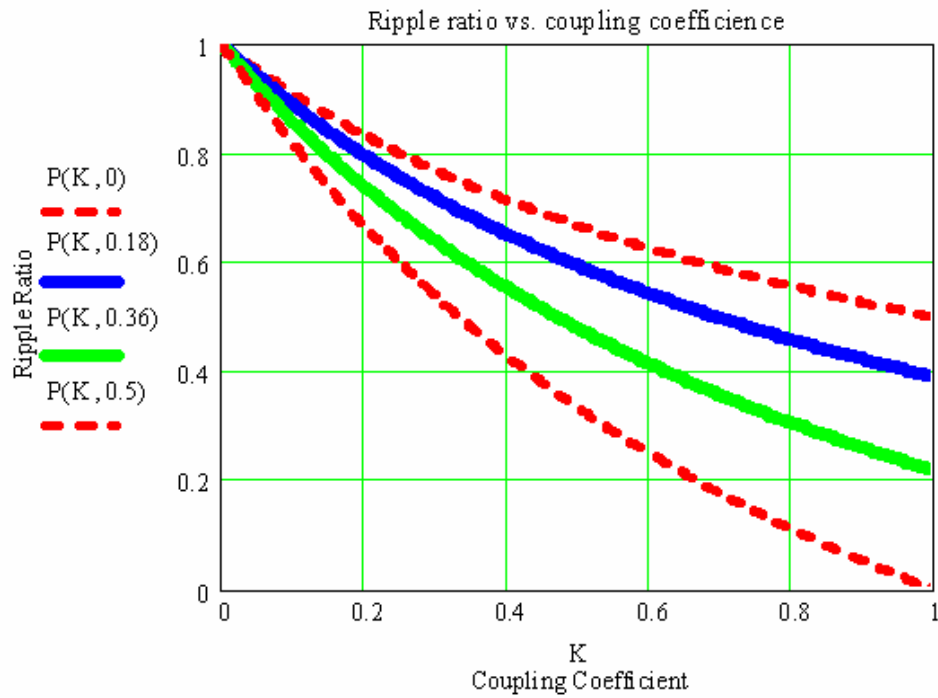
Fig. 4.8 Current ripples vs. coupling coefficient

4.1.3 Analysis and Comparison

In this section, the performance of the circuit with the discrete current doubler structure is compared with conventional two coupled inductors and Y-shape coupled inductors circuit. To

make the comparison fair, the foot print area and the effective filter inductor value L are kept same for different structure.

When the core size is equal, adjusting the coupled inductors coupling coefficient values can get the biggest effective filter inductance value. In this working condition, the coupled inductor structures have lest output current ripple. The Y-shape coupled structure has larger adjustable range for the effective filter inductance value. The structures not only decrease the power loss, but also decrease the output filter capacitor value. In other words, the Y-shape structure can increase the output inductance value and decrease the output capacitance value further.

When the effective inductance value of coupling-inductor structure is equal, then the total output current ripple are same. But the current ripple for each inductor winding is decided by the coupling coefficient K. Strong coupling means small current ripple. When K value is near 1, each coupled inductor current ripple is just half of the discrete structure. Furthermore, this deduction is extended to the MOSFET circuit and decreases the switching losses. For Y-shape coupled inductor, because the effective inductance value is larger than other cases, the current ripple will be decreased further.

Table 4.1 Comparison of Different Structures

Topology	Current Doubler	Coupled Inductor	Y-Shape Structure	
L Number	2	2	3	
Core Number	2	1	1	
L-Effective Inductance	L	$(1-k_0)\cdot L_0$	$(1-k_0)L_0 + 4k_c\sqrt{L_0 L_c} + 2L_c$	
L_m	0	$L_0 \cdot \dfrac{1}{1+\alpha}$	$\dfrac{1+0.5\alpha}{1+\alpha}\cdot L_0 - \dfrac{L}{2}$	
L Average Current	$\dfrac{I_0}{2}$	$\dfrac{I_0}{2}$	$\dfrac{I_0}{2}$	I_0
L Current Ripple	$\dfrac{v_0}{L}\cdot(1-D)\cdot T$	$\left(\dfrac{1+\dfrac{L_m}{L}}{1+2\dfrac{L_m}{L}}\cdot\dfrac{1}{D}-1\right)\cdot\dfrac{V_0}{L}\cdot D\cdot T$	$\left(\dfrac{1+\dfrac{L_m}{L}}{1+2\dfrac{L_m}{L}}\cdot\dfrac{1}{D}-1\right)\cdot\dfrac{V_0}{L}\cdot D\cdot T$	$\dfrac{v_0}{L}\cdot(1-2D)\cdot T$
Total Ripple	$\dfrac{v_0}{L}\cdot(1-2D)\cdot T$	$\dfrac{v_0}{L}\cdot(1-2D)\cdot T$	$\dfrac{v_0}{L}\cdot(1-2D)\cdot T$	

4.1.4 Simualtion Results and Experiment Verification

The Y-shape structure is applied to a half bridge DC/DC converter. One pair of EE core is used in the circuit. The core size is E18 and the core material is 3F3. The core was milled in the center leg to keep from saturation and get the suitable inductance value. Through adjusting the air gap length and center leg winding turn number, the effective filter inductance value can be changed. Steady state asks for high inductance value and less current ripple and the transient response asks for small inductance value. There must have some trade off between the steady

state and transient state. To keep reasonable transient performance, the center leg winding turn number is 1. The circuit operation condition is Fs = 200 KHz, Vin = 36 V, Vout = 3.3 V and the effective inductance value = $150\,nH$.

Due to the inverse coupled out leg winding, the DC flux in the outer leg is partially cancelled by the two corresponding windings. If the effective inductance values are same, the overall DC flux in the coupled inductor structure is almost same as those in the noncoupled core structure. So, when we milled the core center leg, the noncoupled inductor measurement method is adopted.

The electrical circuit simulation result is shown in the Fig. 4.9. The output current ripple is almost the double of the each coupled inductor current ripple. The picture of the hardware is shown in Fig. 4.10. With the inverse coupled inductors, the current ripple in each inductor winding is almost half of the total output current ripple. The experimental results verified the analysis and the simulation results.
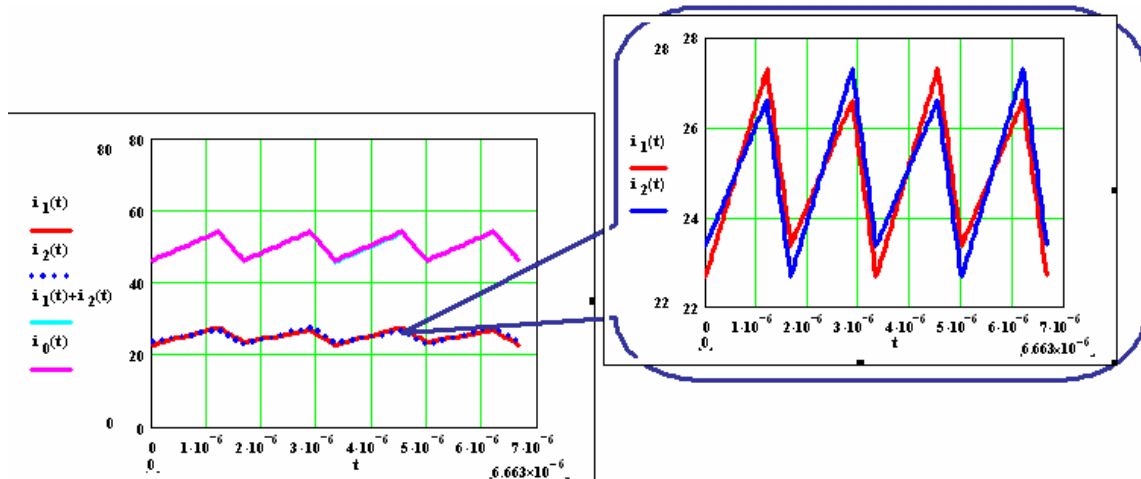
Fig. 4.9 Inductor current waveform simulation results

In this situation, the coupling coefficient is about 0.9.
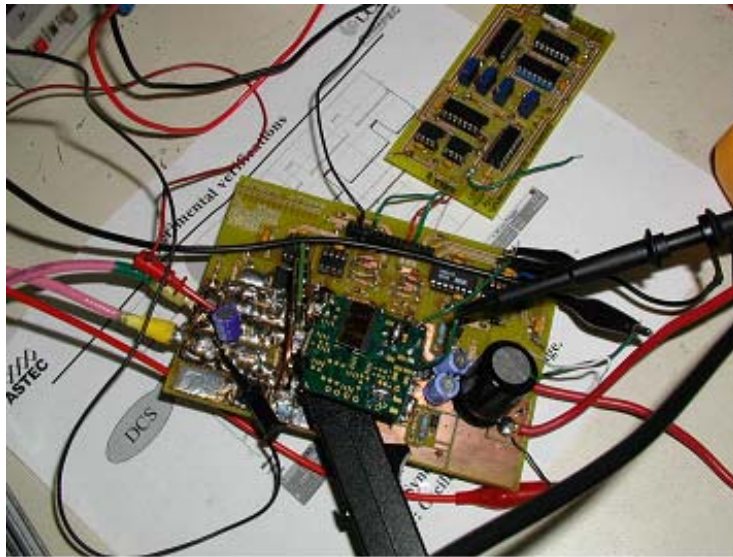
Fig. 4.10 Experiment circuit

The experimental result is showing in Fig. 4.11.
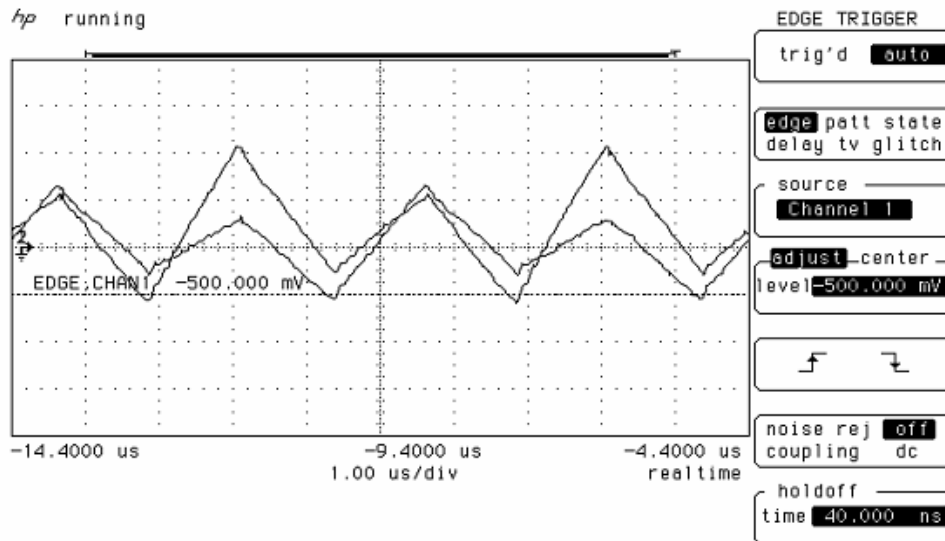
Fig. 4.11 Inductor current experimental result

The simulation and experimental results clearly show that strong coupling can substantially

reduce the ripple in the steady-state waveform.
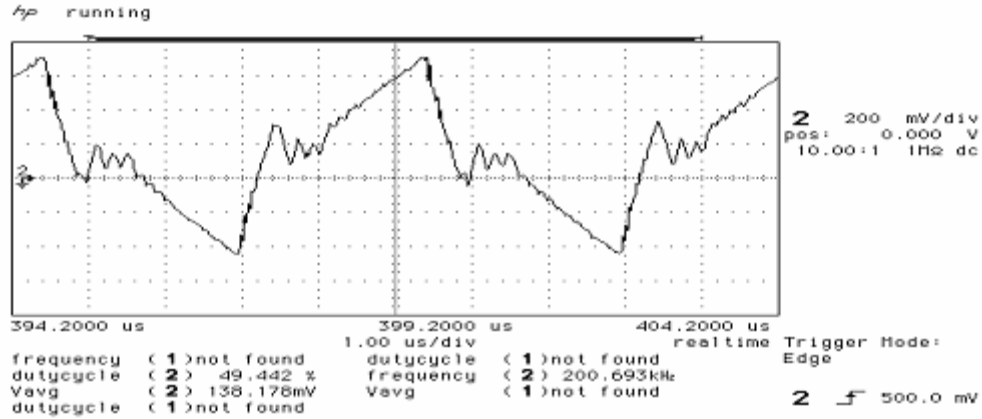
Fig. 4.12 Primary current waveform of discrete structure
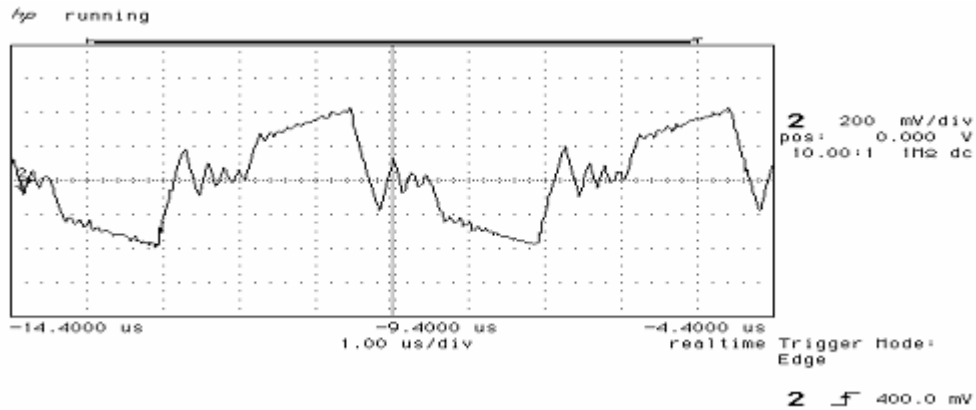
Fig. 4.13 Primary current waveform of coupled inductors structure

The inductor winding current waveforms of the coupled inductor structure and discrete

structure are showing in Fig. 4.12 and Fig. 4.13. Under the same circuit specification and

keeping same effective inductor value and same footprint area for magnetic component, the

coupled inductor structure can decrease primary current ripple.

This circuit can be used as unit and parallel several together for multiphase high current application. The figure was shown in Fig. 4.14. Because of the large filter inductance value, the Y-shape can decrease the phase number and components number. So, for the whole circuit, the cost will be decreased.
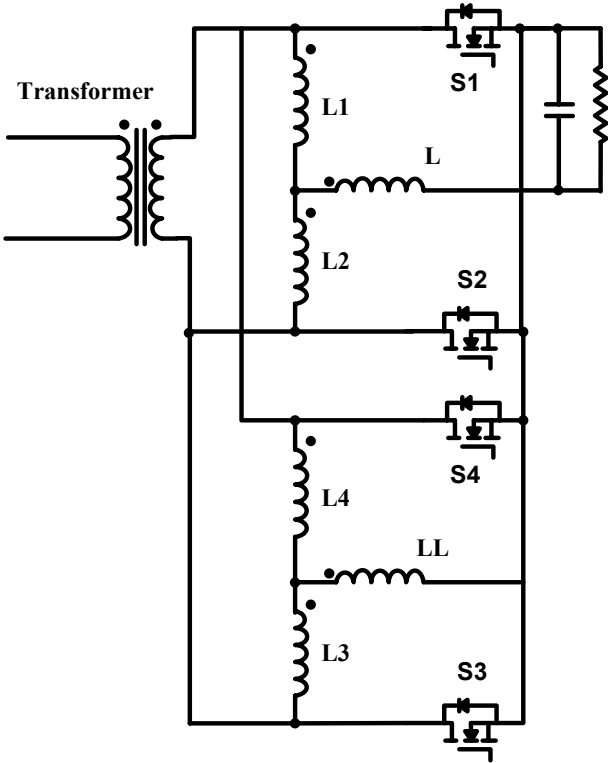
Fig. 4.14 Four phase circuit

4.2 Integrated Transformer and Inductors

As an alternative rectification circuit, the current doubler rectifier has been proven to be suitable for high current DC/DC converters. The applications for this kind of converter include high-input Voltage Regulator Modules (VRMs), both load-end converters and front-end modules

of Distributed Power Systems (DPS), and so on. Compared with the conventional center-tap rectifier, the current doubler rectifier simplifies the structure of the isolation transformer, and cuts the secondary winding conduction loss in half. The inherent disadvantage of this topology is the three magnetic components thus increasing the cost and size of the system as well as causing termination power loss.

By integrating all the magnetic components into one single core, several integrated magnetic solutions have been proposed to solve the problems above. Unlike conventional magnetic integration which only focuses on core integration, both core and winding integration are realized in these designs. For high current applications, this winding integration is becoming more important because of lower termination loss and lower conduction loss.

In this section, four integrated magnetics structures for current-doubler rectifier are investigated and compared thoroughly. High order reluctance model of each integrated magnetics structure is constructed and the quality impedance matrix is derived. With the same core shape, same winding arrangement, same circuit connections and same foot print area, numerical FEA simulation results are compared and implied to the electrical circuit analysis. After unified electrical circuit modes are proposed, the comparison of different structures is more reasonable. The experimental results verify the new core shape design. Due to the less circuit connections and current ripple cancellation, the efficiency of the integrated structure is high.

4.2.1 Comparison of Different Magnetics Structure

4.2.1.1 Different Integrated Magnetics Structures

As explained before, power inductors and transformers are the key components to decide the size, weight and power density in low voltage, high current DC-DC converter. Especially for high current applications, the winding integration is becoming more important because of lower termination loss and lower conduction loss. IM designs typically use soft-ferrite E-I or E-E core structures. The main difference is only in winding arrangements on the three "legs" of the core structure. For the core leg where inductor windings are situated, an air gap is added to obtain the desired inductance values. Effective core leg areas must be chosen in accord with the maximum flux levels, which will occur as a result of converter operation, to prevent saturation of any leg under maximum loading conditions of the system. The use of printed wiring methods for the windings of an IM can lower the height profile of the overall package of the magnetic component. This planar magnetics component can decrease the cost and is easy assembly. In addition, the magnetic features and electric parameters are repeatable. Several integrated magneics circuits have been investigated to decrease the volume and increase the power efficiency [79] [80].

Four different integrated magnetics structures are shown in Fig. 4.15. In structure 1, the transformer and inductor windings can be selected independently. The transformer and the inductors are decoupled from each other. This provides freedom in the design and allows higher inductance to be achieved. But, the separated transformer and inductor windings imply the use of

more copper as well as higher conduction and interconnection losses. In structure 2 [81], the primary and second windings of transformer are located on the different legs. So, the leakage inductance of the transformer is high. This structure has limited filter inductance value. Structure 3 [80] has lower leakage inductance than structure 2. The transformer primary winding is constructed by two windings connected in series. This structure can be considered as the two transformers connected in series. Because the leakage inductor works as the filter inductor, this structure also has limited filter inductance. Compared with other structures, the orthogonal winding structure 4 is proposed [79] to increase the filter inductance value. There is an extra orthogonal winding located on the center leg. The sum of the leakage inductor and the extra winding inductor works as the output filter inductor for the converter. For this structure, the orthogonal winding structure is not normal. So the fabrication complexity is increased. Because the extra winding increases the extra copper, the conduction loss is also increased when the current ripples are same.
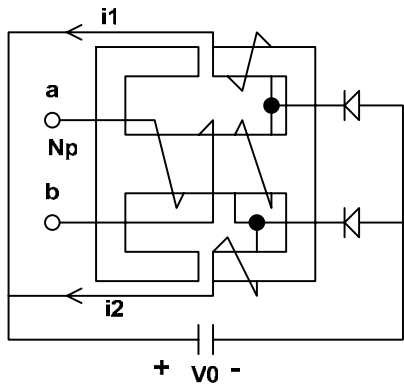
Structure 1   Structure 2
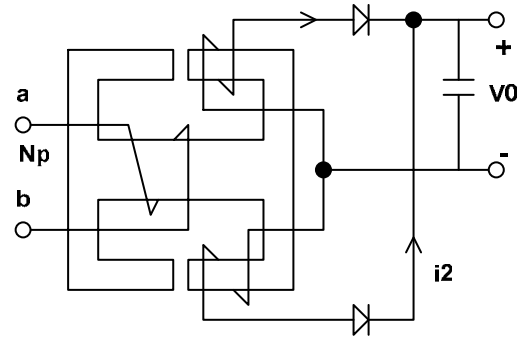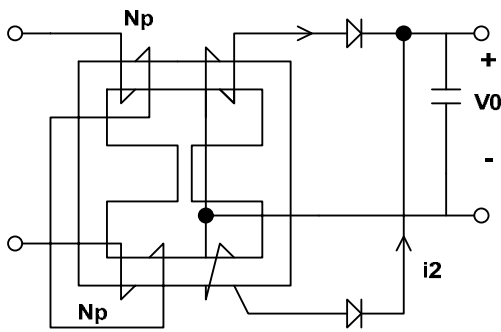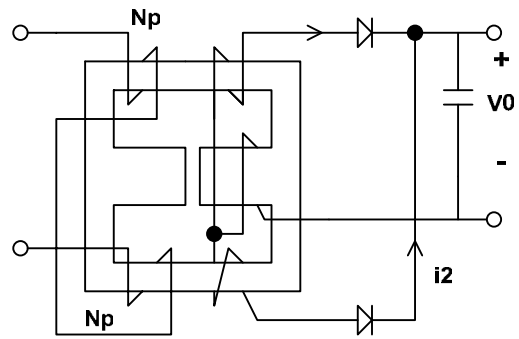
Structure 3   Structure 4

Fig. 4.15 Different integrated magnetics structures

4.2.1.2 Equivalent Reluctance Model Comparison

No matter which kind integrated magnetics component, the equivalent electrical circuit of magnetic component is needed to enable improved analysis of circuit performance. There are two main methods that can derive the equivalent electrical circuit from the magnetic device physical properties: Gyrator-Capacitor method and Reluctance-duality method.

Gyrator-Capacitor is one widely used method to define magnetic component equivalent electrical circuit. It is easier to relate electrical performance back to the magnetic elements. A major advantage of Gyrator-Capacitor is that it does not require the magnetic circuit be "planar", as the reluctance duality method does. However, the equivalent electrical circuit derived from this method looks nothing like a classical inductor or transformer. Inductive energy storage elements are replaced by capacitors and transformer windings are replaced by gyrators. An equivalent circuit with capacitors and gyrators replacing inductive elements whose layout closely resembles the structure of the magnetic device. This facilitates insight into the physical electrical relationship, but severely diminishes insight into circuit analysis [82].

The conventional reluctance-duality method defines an electrical circuit whose magnetic elements include leakage, magnetizing inductances and transformer windings, etc. This facilitates intuitive and insightful circuit analysis, but it does not resemble the magnetic device physical structure, diminishing insight into the physical-electrical relationship. Magnetic circuits and electrical circuits are in a different realm, and the duals are truly equivalent.

In the integrated magnetics comparison and analysis, the magnetizing inductance, leakage inductance and effective windings are very important for the circuit performance. So, the conventional Reluctance-duality method is adopted here. For these four different IM structures, the simple reluctance model is shown in Fig. 4.16.

Structure 1   Structure 2

Structure3   Structure 4
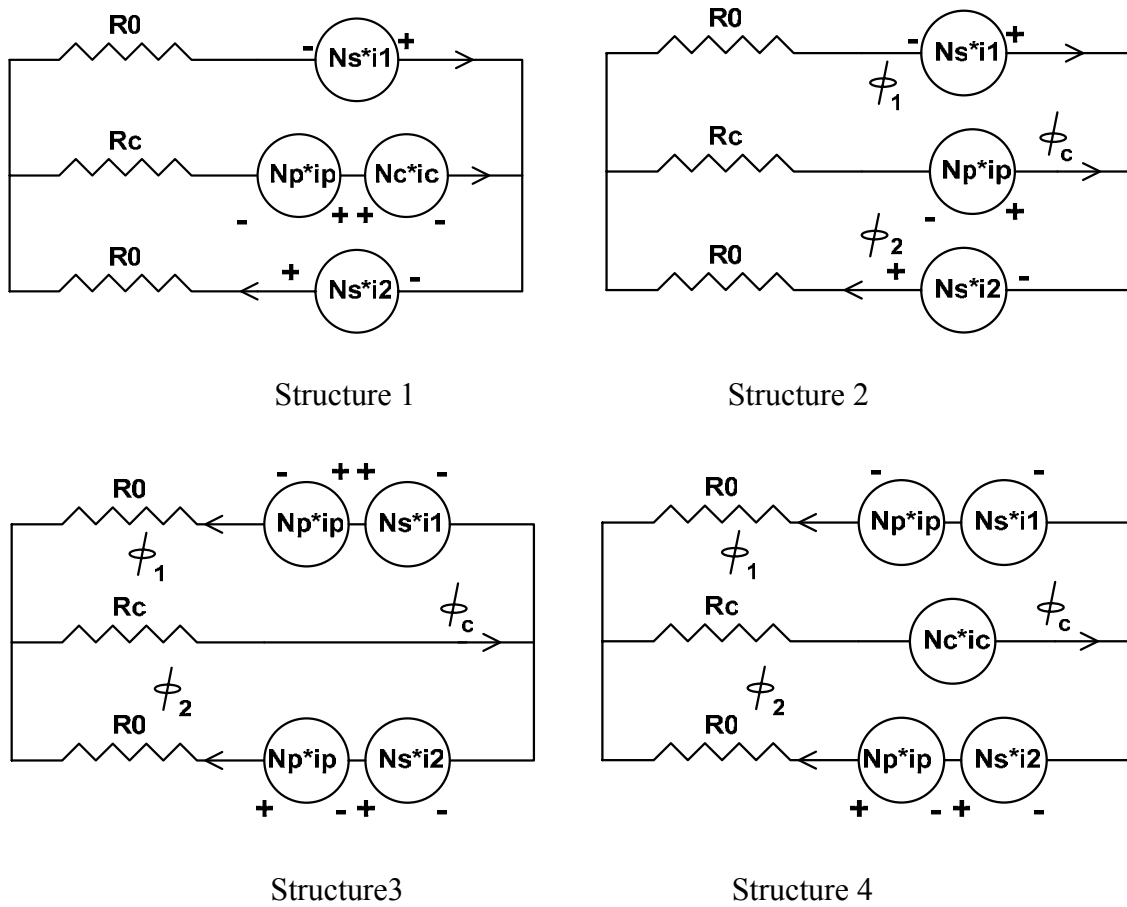
Fig. 4.16 Different reluctance model structures

There are four working modes for current doubler rectifier and it was shown in Fig. 4.17. In these reluctance models, R_0 is the out leg reluctance and R_c is the center leg reluctance; N_p is the primary winding turns number and N_s is the secondary winding turns number; ϕ_1 and ϕ_2 are flux in out legs and ϕ_c is the flux in the center leg.

94

Mode 1   Mode 2

Mode3   Mode 4
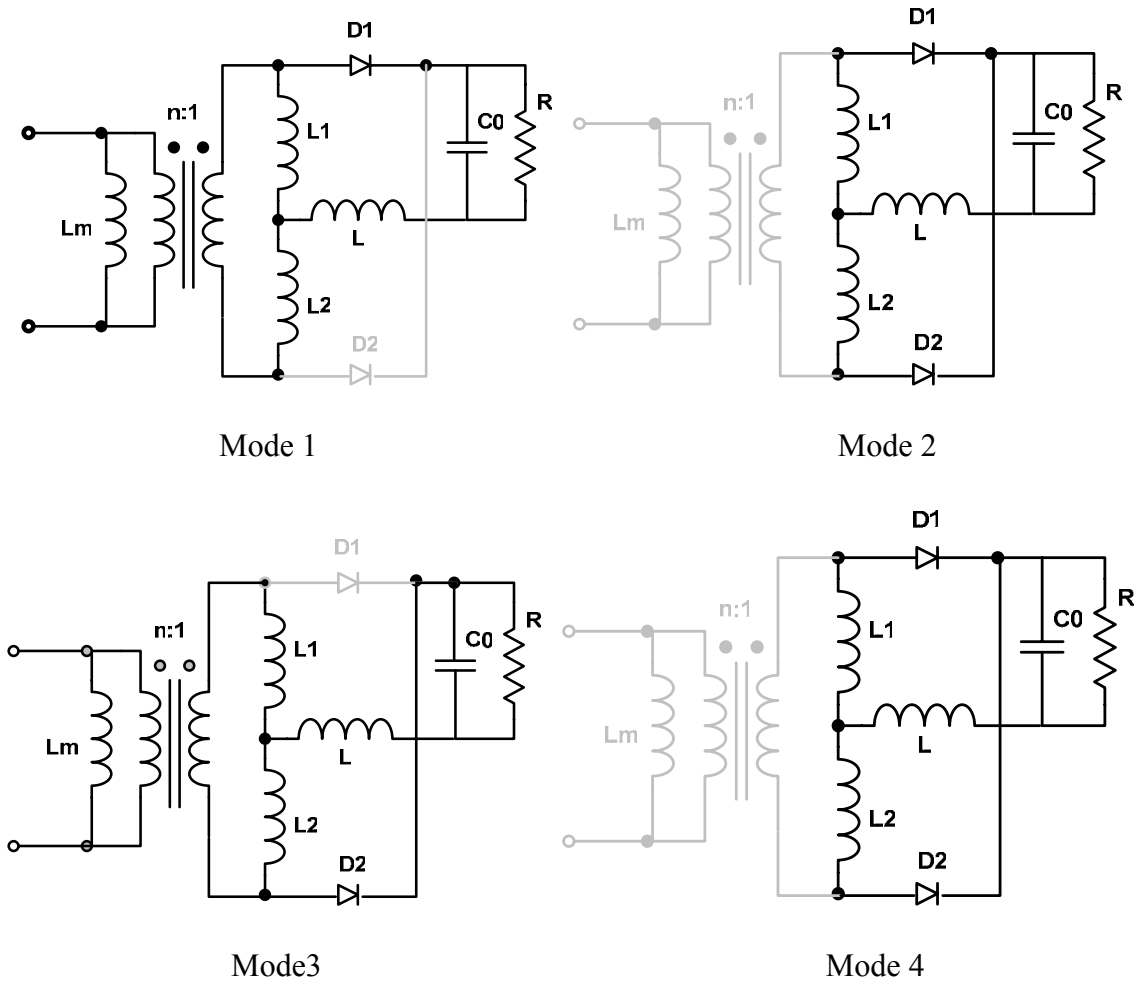
Fig. 4.17 Current doubler working modes

For structure 1:

The flux in each core leg is shown:

$$\phi_1 = \frac{-1}{2R_c + R_0}\left(N_p i_p\right) + \frac{i_1}{2R_c + R_0}\left(\frac{R_0 + R_c}{R_0}N_s + N_c\right) + \frac{i_2}{2R_c + R_0}\left(\frac{R_c}{R_0}N_s + N_c\right)$$

(64)

$$\phi_2 = \frac{1}{2R_c + R_0}\left(N_p i_p\right) + \frac{i_1}{2R_c + R_0}\left(\frac{R_c}{R_0}N_s - N_c\right) + \frac{i_2}{2R_c + R_0}\left(\frac{R_0 + R_c}{R_0}N_s - N_c\right)$$

(65)

$$\phi_c = \frac{2}{2R_c + R_0}\left(N_p i_p\right) + \frac{i_1}{2R_c + R_0}\left(-N_s - 2N_c\right) + \frac{i_2}{2R_c + R_0}\left(N_s - 2N_c\right) \tag{66}$$

The primary and secondary winding voltage equations are in the following:

$$V_{in} = N_p \frac{d}{dt}\phi_c = \frac{2N_p^2}{2R_c + R_0}\frac{d}{dt}i_p + \frac{-2N_c N_p - N_p N_s}{R_0 + 2R_c}\frac{d}{dt}i_1 + \frac{-2N_c N_p + N_p N_s}{R_0 + 2R_c}\frac{d}{dt}i_2 \tag{67}$$

$$V_1 = N_s\frac{d}{dt}\phi_1 - N_c\frac{d}{dt}\phi_c = \frac{-N_P N_s - 2N_P N_c}{2R_c + R_0}\frac{d}{dt}i_p + \frac{\frac{R_0 + R_c}{R_0}N_s^2 + 2N_c N_s + 2N_c^2}{R_0 + 2R_c}\frac{d}{dt}i_1 + \frac{\frac{R_c}{R_0}N_s^2 + 2N_c^2}{R_0 + 2R_c}\frac{d}{dt}i_2 \tag{68}$$

$$V_2 = N_s\frac{d}{dt}\phi_2 - N_c\frac{d}{dt}\phi_c = \frac{N_P N_s - 2N_P N_c}{2R_c + R_0}\frac{d}{dt}i_p + \frac{\frac{R_c}{R_0}N_s^2 + 2N_c^2}{R_0 + 2R_c}\frac{d}{dt}i_1 + \frac{\frac{R_0 + R_c}{R_0}N_s^2 - 2N_c N_s + 2N_c^2}{R_0 + 2R_c}\frac{d}{dt}i_2 \tag{69}$$

According to the working modes and voltage-second balance, the voltage ratio MD is:

$$MD = D\frac{2N_c + N_s}{N_p} \tag{70}$$

The effective filter inductance value is derived as:

$$L = \frac{N_s^3}{\left(-N_s + 2N_c\right)R_0} \tag{71}$$

The magnetizing inductance value as:

$$L_m = \frac{N_p^2}{0.5R_0 + R_c} \tag{72}$$

The mutual inductance value between the two filter inductors is:

$$M = \frac{2N_c N_p + N_p N_s}{R_0 + 2R_c}$$

(73)

Using the same analysis method, the quality parameters for different IM structures are shown in Table 4.2.

Table 4.2 Four IM structures parameters comparison

	Turn ratio	L	Lm
1	$\dfrac{N_p}{2N_c + N_s}$	$\dfrac{N_s^3}{(2N_c + N_s) \cdot R_0}$	$\dfrac{N_p^2}{0.5R_0 + R_c}$
2	$\dfrac{N_p}{N_s}$	$\dfrac{N_s^2}{R_0}$	$\dfrac{N_p^2}{0.5R_0 + R_c}$
3	$\dfrac{N_p}{N_s}$	$\dfrac{N_s^2}{R_0 + 2R_c}$	$\dfrac{2N_p^2}{R_0}$
4	$\dfrac{N_p}{N_s}$	$\dfrac{N_s^2 + 4N_s N_c + 4N_c^2}{R_0 + 2R_c}$	$\dfrac{2N_p^2}{R_0}$

From the table, we can see that the structure 1 and structure 2 are similar to each other. Structure 1 has less turn ratio and less effective inductance value. Structure 3 and 4 are similar to each other, except that structure 4 has larger effective inductance value. It is easy to understand that the less the air gap length, the larger the magnetizing inductance value.

To obtain a better understanding of the magnetic operations of the IM structures, equivalent circuit models are developed, using the high order reluctance-to-inductance modeling method described in following. These models can be used to study the dynamics and magnetic

97

interactions between the transformer and inductive sections of an integrated magnetics component. The methodology to construct the dual circuit from the original physical structure consists of the following procedure:

1. Construct the magnetic circuit from the original physical structure.

2. Put a reference dot inside each loop of the magnetic circuit and a reference dot outside. These points become the nodes of the electric circuits.

3. Draw a line between any two nodes of the magnetic circuit to pass through one and only one circuit element. Repeat the same procedure for each element of the magnetic circuits.

4. Scale the dual magnetic circuit model by the number of turns on the primary.

5. Replace reluctances with inductances and use ideal transformer symbols where appropriate.

The physical structure of integrated magnetics structure 1 is shown in Fig. 4.18 (a). Then, the high order reluctance mode is constructed in Fig. 4.18 (b). Using the methodology that we have introduced before, the equivalent circuit model is presented in Fig. 4.18 (c).

The RL0 means the leakage reluctance to the air around the core out leg; RLps is the leakage reluctance between the primary windings and the secondary windings; RL is the secondary winding leakage reluctance; Rm is the core reluctance for the top and bottom; Rc is the center leg reluctance.

(a) Physical Model

(b) High Order Reluctance Model

(c) Equivalent Circuit Model
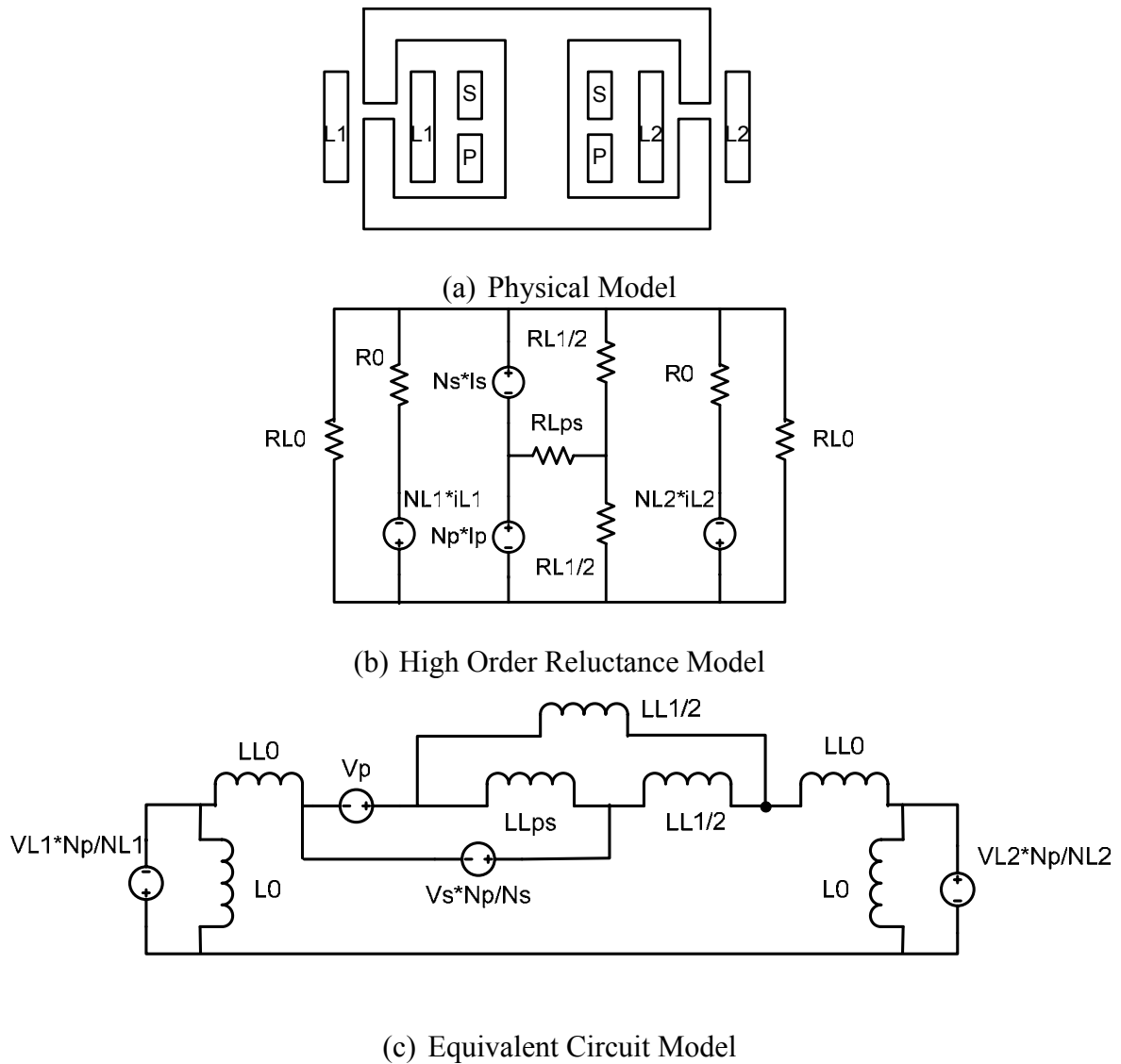
Fig. 4.18 IM structure 1 model derivations

Through the reluctance-duality method, we scale the dual magnetic circuit model by the number of turns on the primary. Each physical winding is modeled as a voltage source. In the equivalent high order circuit model, all the parameters are reflected to the primary and they are directly related to their physical structure. From the circuit, the impedance matrix can be extracted.

$$\begin{bmatrix} v_p \\ v_{ps} \\ v_{pL1} \\ v_{pL2} \end{bmatrix} = \begin{pmatrix} 2(LL0+L0)+\dfrac{\dfrac{LL1}{2}\left(LLps+\dfrac{LL1}{2}\right)}{LLps+LL1} & 2(LL0+L0)+\dfrac{\dfrac{LL1}{2}\cdot\dfrac{LL1}{2}}{LLps+LL1} & L0 & L0 \\[6mm] 2(LL0+L0)+\dfrac{\dfrac{LL1}{2}\cdot\dfrac{LL1}{2}}{LLps+LL1} & 2(LL0+L0)+\dfrac{\dfrac{LL1}{2}\left(LLps+\dfrac{LL1}{2}\right)}{LLps+LL1} & L0 & L0 \\[6mm] L0 & L0 & L0 & 0 \\[2mm] L0 & L0 & 0 & L0 \end{pmatrix}\cdot i$$

$$(74)$$

Through the same method, the physical structure of integrated magnetics structure 2 is obtained and shown in Fig. 4.19 (a). The high order reluctance mode is constructed in Fig. 4.19 (b). Using the methodology that we have introduced before, the equivalent circuit model is presented in Fig. 4.19 (c). From the circuit, the impedance matrix can be extracted.
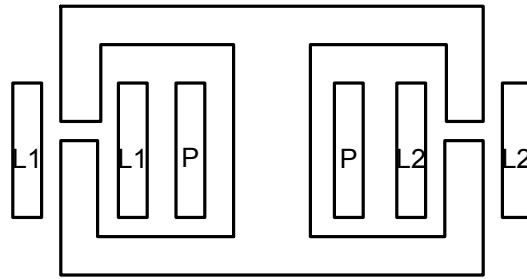
(a) Physical model
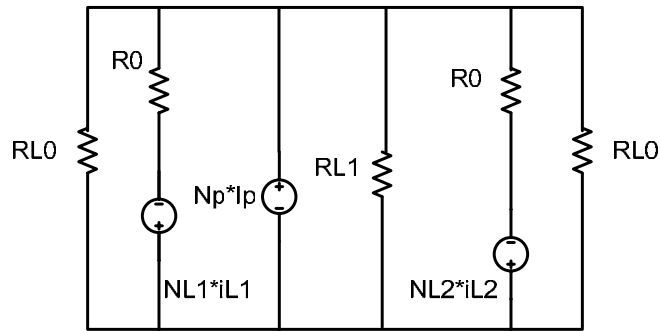
(b) High order reluctance model
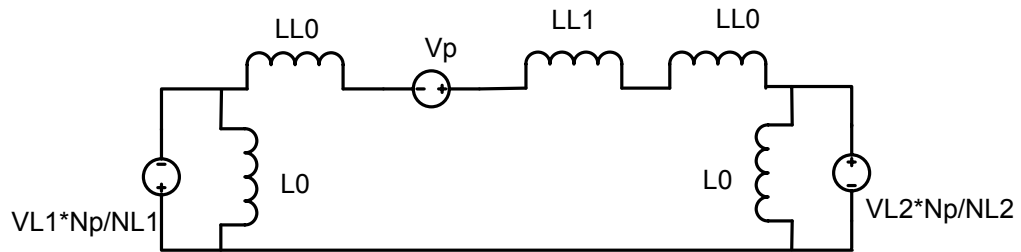
(c) Equivalent Circuit Model

Fig. 4.19 IM structure 2 model derivations

$$\begin{bmatrix} v_p \\ v_{pL1} \\ v_{pL2} \end{bmatrix} = \begin{pmatrix} 2(L0 + LL0) + LL1 & L0 & L0 \\ L0 & L0 & 0 \\ L0 & 0 & L0 \end{pmatrix} \cdot i \tag{75}$$

The physical structure of integrated magnetics structure 3 is shown in Fig. 4.20 (a). The high order reluctance mode is constructed in Fig. 4.20 (b). The equivalent circuit model is illustrated in Fig. 4.20 (c). From the circuit, the impedance matrix is derived.

(a) Physical model

(b) High order reluctance model

(c) Equivalent circuit model

Fig. 4.20 IM structure 3 model derivations

102

$$Z =$$

$$
\begin{pmatrix}
2LL_0 + LL_c + \dfrac{LL_1\left(LL_{ps} + \dfrac{LL_1}{2}\right)}{LL_{ps}+LL_1} & LL_0 + \dfrac{LL_c}{2} + \dfrac{\dfrac{LL_1}{2}\dfrac{LL_1}{2}}{LL_{ps}+LL_1} & -\left(LL_0 + \dfrac{LL_c}{2} + \dfrac{\dfrac{LL_1}{2}\dfrac{LL_1}{2}}{LL_{ps}+LL_1}\right) \\[3em]
LL_0 + \dfrac{LL_c}{2} + \dfrac{\dfrac{LL_1}{2}\dfrac{LL_1}{2}}{LL_{ps}+LL_1} & LL_0 + \dfrac{L_m(L_m+LL_c)}{LL_c+2L_m} + \dfrac{\dfrac{LL_1}{2}\left(LL_{ps}+\dfrac{LL_1}{2}\right)}{LL_{ps}+LL_1} & \dfrac{L_mL_m}{LL_c+2L_m} \\[3em]
-\left(LL_0 + \dfrac{LL_c}{2} + \dfrac{\dfrac{LL_1}{2}\dfrac{LL_1}{2}}{LL_{ps}+LL_1}\right) & \dfrac{L_mL_m}{LL_c+2L_m} & LL_0 + \dfrac{L_m(L_m+LL_c)}{LL_c+2L_m} + \dfrac{\dfrac{LL_1}{2}\left(LL_{ps}+\dfrac{LL_1}{2}\right)}{LL_{ps}+LL_1}
\end{pmatrix}
$$

$$(76)$$

The physical structure of integrated magnetics structure 4 is shown in Fig. 4.21 (a). The high order reluctance mode is constructed in Fig. 4.21 (b). The equivalent circuit model is given in Fig. 4.21 (c). From the circuit, the impedance matrix is shown.

(a) Physical model

(b) High order reluctance model

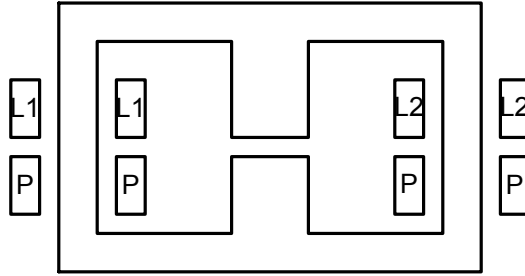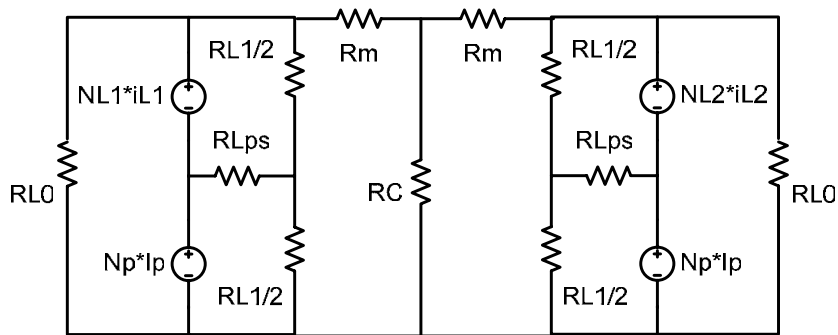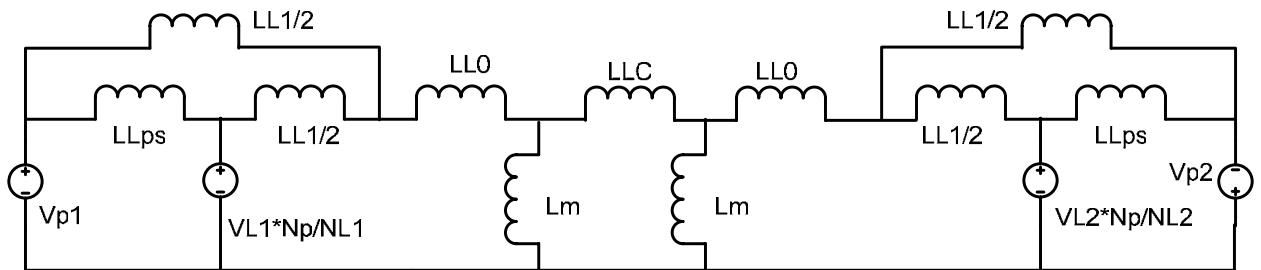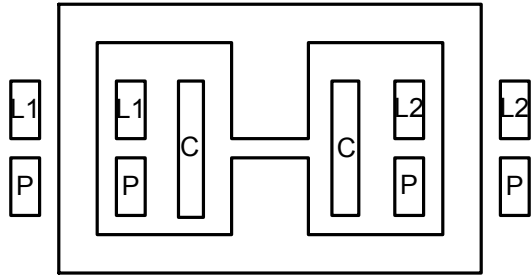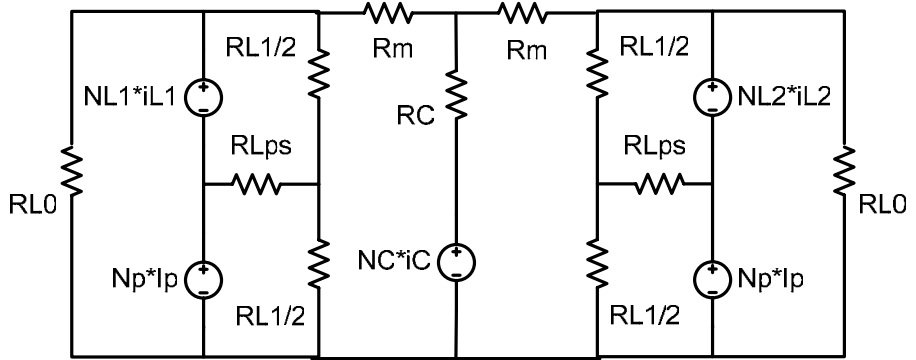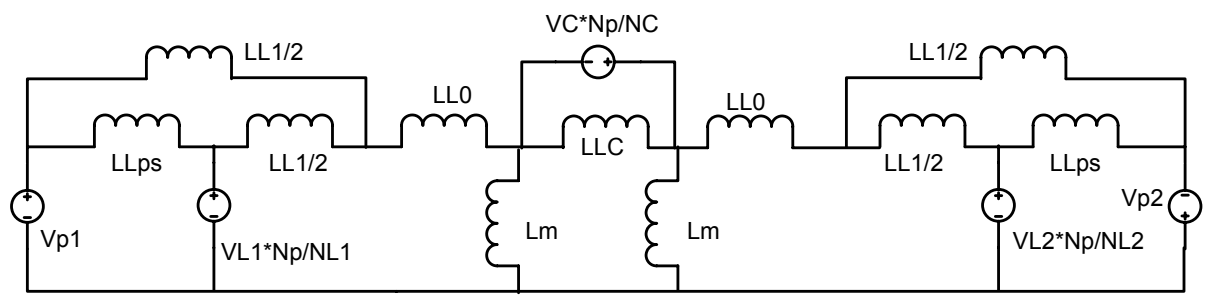(c) Equivalent circuit model

Fig. 4.21 IM structure 4 model derivations

$$
\begin{pmatrix}
2LL_0 + LL_t + \dfrac{LL_1\left(LLps + \dfrac{LL_1}{2}\right)}{LLps + LL_1} & LL_0 + \dfrac{LL_t}{2} + \dfrac{\dfrac{LL_1}{2}\dfrac{LL_1}{2}}{LLps + LL_1} & -\left(LL_0 + \dfrac{LL_t}{2} + \dfrac{\dfrac{LL_1}{2}\dfrac{LL_1}{2}}{LLps + LL_1}\right) & -LL_t \\[4mm]
LL_0 + \dfrac{LL_t}{2} + \dfrac{\dfrac{LL_1}{2}\dfrac{LL_1}{2}}{LLps + LL_1} & LL_0 + \dfrac{L_m(L_m + LL_t)}{LL_t + 2L_m} + \dfrac{\dfrac{LL_1}{2}\left(LL_{ps} + \dfrac{LL_1}{2}\right)}{LL_{ps} + LL_1} & \dfrac{L_m L_m}{LL_t + 2L_m} & \dfrac{-LL_t L_m}{LL_t + 2L_m} \\[4mm]
-\left(LL_0 + \dfrac{LL_t}{2} + \dfrac{\dfrac{LL_1}{2}\dfrac{LL_1}{2}}{LL_{ps} + LL_1}\right) & \dfrac{L_m L_m}{LL_t + 2L_m} & LL_0 + \dfrac{L_m(L_m + LL_t)}{LL_t + 2L_m} + \dfrac{\dfrac{LL_1}{2}\left(LL_{ps} + \dfrac{LL_1}{2}\right)}{LL_{ps} + LL_1} & \dfrac{LL_t L_m}{LL_t + 2L_m} \\[4mm]
-LL_t & \dfrac{-LL_t L_m}{LL_t + 2L_m} & \dfrac{LL_t L_m}{LL_t + 2L_m} & \dfrac{LL_t L_m}{LL_t + 2L_m}
\end{pmatrix}.
$$

$$\tag{77}$$

The order of the matrix is decided by the winding number. Each winding is molded as a voltage source. Even though the primary winding is constructed by two sub windings, it's still considered as one source because the two sub-windings are connected in series and the currents flowing through them are always same.

Compared with the simple reluctance model, the high order reluctance model has an accurate calculation method for the leakage inductance, properly predicts a small leakage between adjacent windings and each leakage inductance is directly related to the space between the windings. The models predict there is more deviation from ideal transformer turn ratio as the windings move further from the primary winding because the current has to flow through more leakage inductance.

4.2.1.3 CAD Methodology and Unified Circuit Model

The simple reluctance model can only give some quality comparisons. When there is air gap, the accurate parasitic value is difficult to obtain. Even though the high order reluctance model is adopted, it is suitable for quality analysis instead of quantity analysis. At the same time, the interleaved winding strategy and non-interleaved strategy have the same reluctance model. The magnetizing and leakage inductances (the coupling coefficients) of both cases are different. Since these values are very sensitive to the winding strategy, their calculations are very difficult using analytical expressions. To improve or enhance the circuit performance, the magnitude of relevant parasitic magnetic elements is needed and the quantity comparison is needed. The FEA numerical analysis is adopted to do the simulation.

"Double 2-D" is a methodology used to calculate the energy and losses in 3-D structures (EE and toroids), taking into account the 3-D effects and using 2-D FEA solvers. This is shown in Fig. 4.22.

From the front direction

+

From the side direction
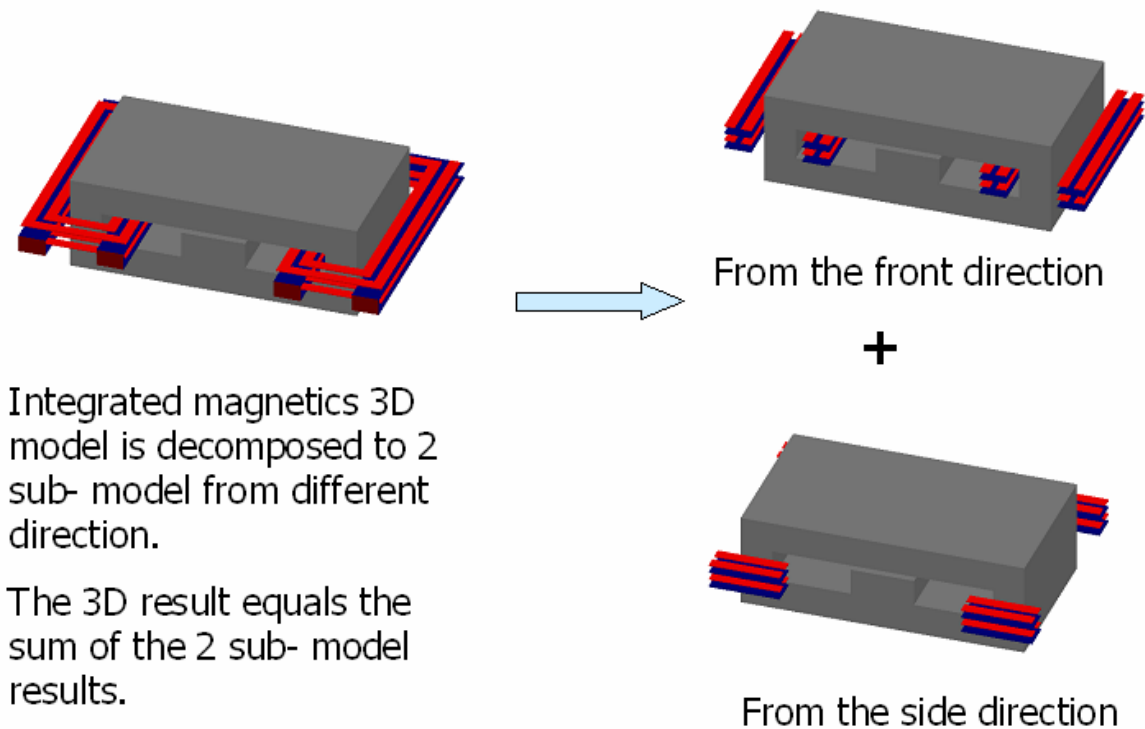
Fig. 4.22 Double-2D methodology

The double 2D simulation omits the corner effects and it's suitable for the E core. When the frequency is increased and the ration of the skin depth and cooper thickness is decreased, the accuracy of the 2D simulation decreases. The simulation result is only accurate during reasonable range. Otherwise, the 3D simulation is needed. From the simulation results, the impedance matrixes are extracted. The order of the impedance matrix is decided by the winding number. If the total winding of the IM structure is n, the matrix will be the n X n matrix. In this situation, it is hard to compare the parameters of the different structure. To make a reasonable comparison, all the models have to been changed to one 3 port electrical net. The unified format is constructed in Fig. 4.23 (a).
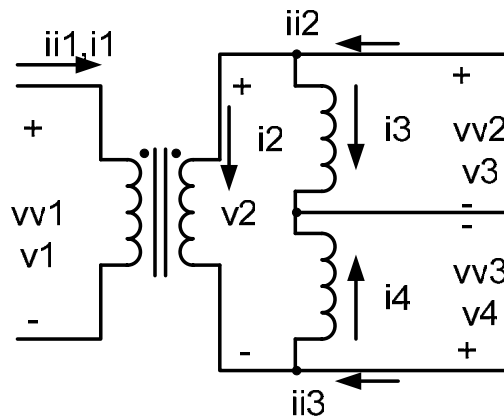
(a) Physical structure
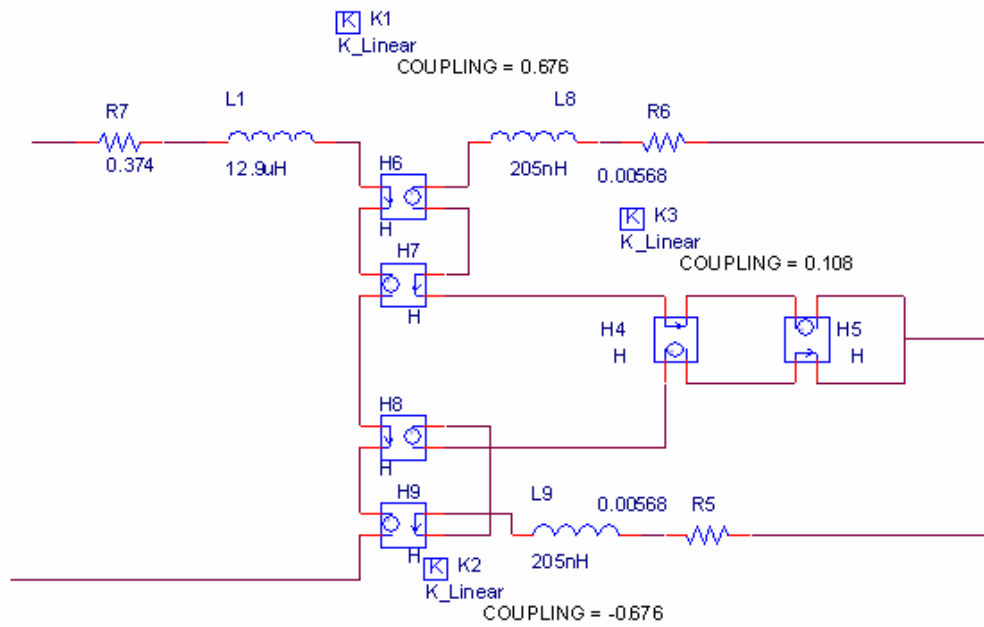
(b) Pspice unified circuit model

Fig. 4.23 Unified 3 ports electrical circuit

All the impedance matrix and coupling coefficient matrix can be changed to 3 by 3 matrix. The

Pspice simulation model is constructed based on the 3 by 3 matrix. The H block is used to construct

the mutual resistors. K linear is used to construct the coupling coefficient. When the unified model is putted into the model, it is easy to analyze and to improve the performance of the circuit.

It has been explained before that the magnetics component parameters are decided by the physical dimension of the core, winding structure and terminal connections. It does not make sense to compare the structures if the comparison conditions are not fixed. The different integrated structures may have same performance due to the different conditions. So, to make the results more reasonable, we set following conditions: same core shape (E18), same core material (3F3), same foot print (including cooper area), and same terminal connections. For these specified designs, we conduct the simulations and compare them with each other.

The FEA results for integrated structures are as follows:

Table 4.3 IM Structure 1 Impedance Matrix

	P		L1		L2	
	Resistor (ohm)	Inductor (H)	Resistor (ohm)	Inductor (H)	Resistor (ohm)	Inductor (H)
P	1.36×10^{-1}	2.92×10^{-6}	-1.3×10^{-2}	-4.73×10^{-7}	1.3×10^{-2}	4.73×10^{-7}
L1	-1.3×10^{-2}	-4.73×10^{-7}	5.035×10^{-3}	1.671×10^{-7}	4.43×10^{-4}	9.151×10^{-9}
L2	1.3×10^{-2}	4.73×10^{-7}	4.43×10^{-4}	9.151×10^{-9}	5.035×10^{-3}	1.67×10^{-7}

	P	L1	L2
P	1	-0.702	0.701
L1	-0.702	1	0.00618
L2	0.701	0.00618	1

Table 4.4 IM structure 2 impedance matrix

	P		L1		L2	
	Resistor (ohm)	Inductor (H)	Resistor (ohm)	Inductor (H)	Resistor (ohm)	Inductor (H)
P	1.48×10^{-1}	3.14×10^{-6}	-1.27×10^{-2}	-5.027×10^{-7}	1.27×10^{-2}	5.027×10^{-7}
L1	-1.27×10^{-2}	-5.027×10^{-7}	5.542×10^{-3}	1.841×10^{-7}	2.564×10^{-5}	4.182×10^{-10}
L2	1.27×10^{-2}	5.027×10^{-7}	2.564×10^{-5}	4.182×10^{-10}	5.542×10^{-3}	1.84×10^{-7}

	P	L1	L2
P	1	-0.66114	0.66114
L1	-0.66114	1	0.002272
L2	0.66114	0.002272	1

Table 4.5 IM Structure 3 Impedance Matrix

	P		L1		L2	
	Resistor (ohm)	Inductor (H)	Resistor (ohm)	Inductor (H)	Resistor (ohm)	Inductor (H)
P	1.208×10^{-1}	7.7×10^{-5}	-1.27×10^{-2}	-5.027×10^{-7}	2.498×10^{-3}	1.02×10^{-5}
L1	-7.31×10^{-5}	-1×10^{-5}	4.448×10^{-3}	1.51×10^{-6}	6.799×10^{-4}	-1.36×10^{-6}
L2	2.498×10^{-3}	1.02×10^{-5}	6.799×10^{-4}	-1.36×10^{-6}	4.448×10^{-3}	1.51×10^{-6}

	P	L1	L2
P	1	-0.9301	0.94208
L1	-0.9301	1	0.90139
L2	0.94208	0.90139	1

Table 4.6 IM Structure 4 Impedance Matrix

	P		L1		L2	
	Resistor (ohm)	Inductor (H)	Resistor (ohm)	Inductor (H)	Resistor (ohm)	Inductor (H)
P	1.35×10^{-1}	7.018×10^{-5}	3.633×10^{-3}	-1.009×10^{-5}	-3.064×10^{-4}	-1.022×10^{-5}
L1	3.633×10^{-3}	-1.009×10^{-5}	2.1×10^{-2}	1.717×10^{-6}	7.198×10^{-3}	1.585×10^{-6}
L1	-3.064×10^{-4}	-1.022×10^{-5}	7.198×10^{-3}	1.585×10^{-6}	2.1×10^{-2}	1.813×10^{-6}

	P	L1	L2
P	1	-0.919	0.906
L1	-0.919	1	0.898
L2	0.906	0.898	1

In each table above, the first matrix is the resistance and inductance value and the second matrix is the coupling coefficient. From the matrix, we can see that structures 1 and 2 are almost the same. Structure 3 and 4 are similar. In the first two structures, the output two inductors are almost decoupled. For the current doubler application, the strong coupling between these two inductors can decrease the current ripple. The impedance matrix clearly shows that structure 3 has the least power loss (least resistor value).

The precondition for comparison is to keep the total footprint area equal for each structure. At the same time, the effective filter inductance values are also equal. For structures 1 and 2, the two inductors are almost decoupled from each other and the self inductance value equals the filter inductance value. The coupling coefficient value is near zero. But for structures 3 and 4, there are strong coupling between the two inductors. The coupled inductors can be molded as an

ideal inverse transformer and the effective filter inductor value can be modeled as the leakage inductance value of this transformer. For structures 1 and 2, the primary and the secondary windings have less coupling compared with structures 3 and 4. So the leakage inductance values for them are large. But, even the other two structures are strongly coupled; the coupling coefficient values are still less than the discrete magnetics structure. The one feature of integrated magnetics is the higher leakage inductance value compared with the discrete structure. It should be mentioned that the inductor resistance value for the structure 4 is larger than other three. This comes from extra winding located on the center leg.

4.2.1.4 Experiment Verification

Through the procedure described above, discrete magnetics current doubler structure and four different integrated magnetics structures are analyzed and compared with each other. To verify the analysis, a half bridge converter is constructed. Each different magnetics structure is added to the same power circuit. Through the experiments, the input voltage and the load current are kept equal for each different structure. At the same time, the effective inductance values for each IM structures are equal to the discrete inductance value. The footprint areas of these structures are the same. These entire requirements are going to decrease the influence coming from the semiconductor components and circuit connections. The experiment is trying to make the main efficiency difference between the circuit efficiency to represent the different power loss between different magnetics components. The experimental prototype is shown in Fig. 4.24.
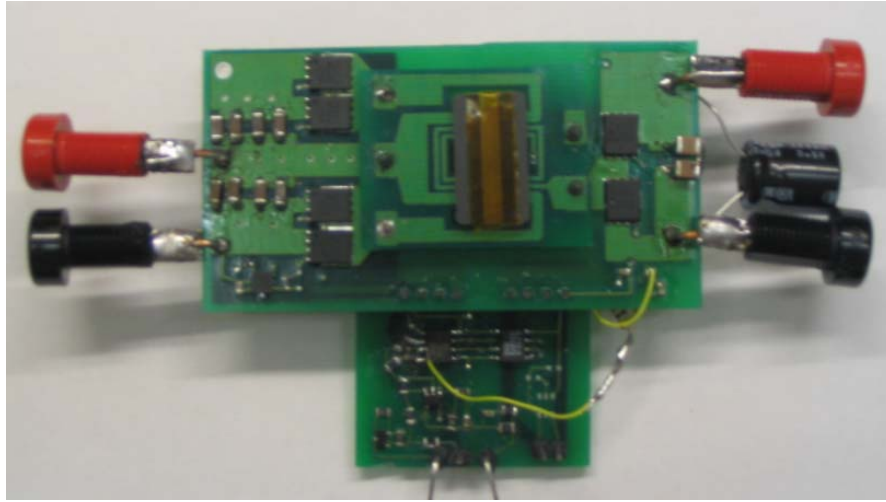
(a) Experiment power circuit
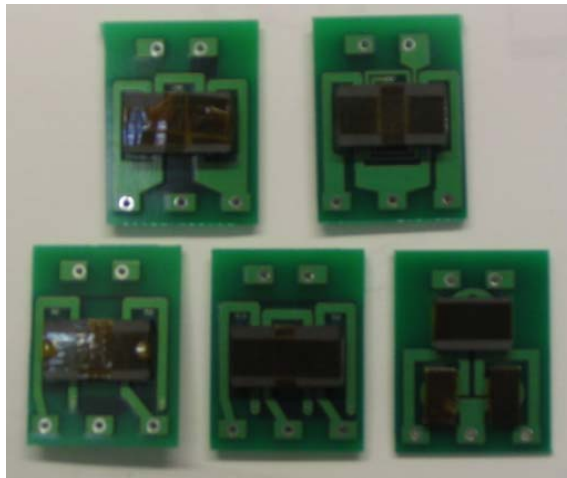
(b) Different magnetics structure

Fig. 4.24 Experiment prototypes

The experimental waveforms are shown in Fig. 4.25.
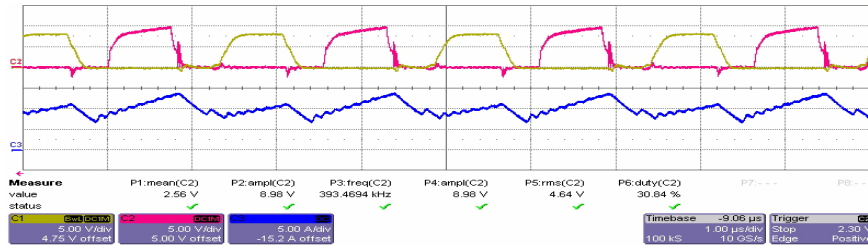
(a) Discrete structure output current
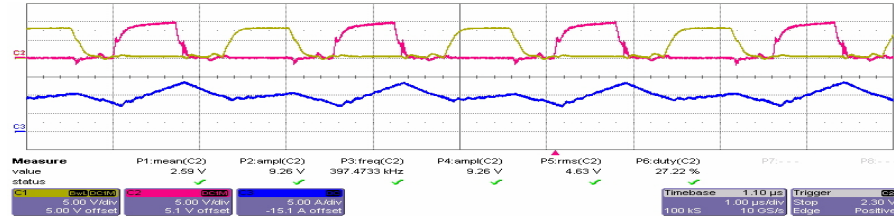
(b) Integrated magnetics structure 1 output current
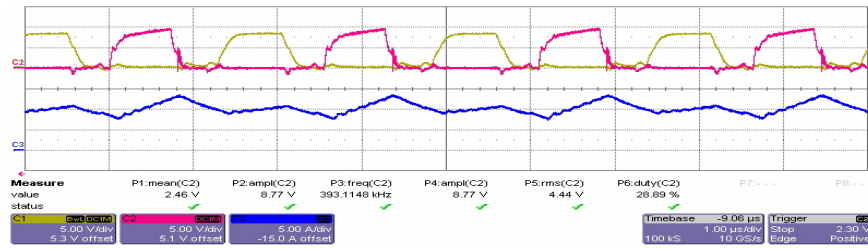
(c) Integrated magnetics structure 2 output current
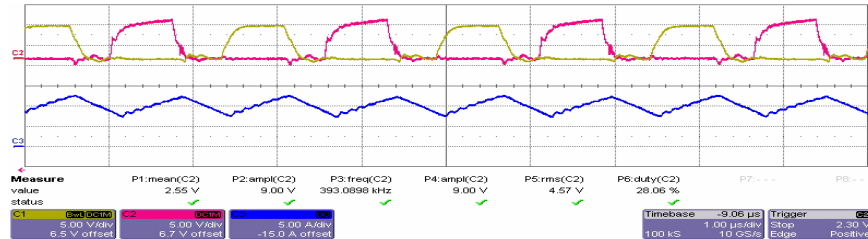
(d) Integrated magnetics structure 3 output current
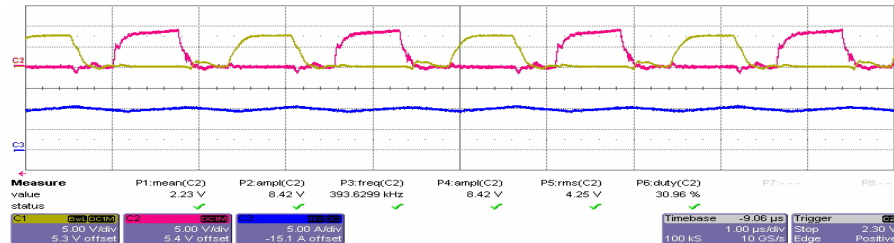
(e) Integrated magnetics structure 4 output current

Fig. 4.25 Output current waveforms for different magnetics structure

For the discrete structure, because the air gap length for the two discrete inductors is adjusted separately, it is easy to get unequal inductance value. This phenomenon happens to structures 1 and 2. Because for these two structures, the air gaps are located on the two out legs and the core parts connection is located on the center leg. These structures are mechanical unstable in practice. Even when the air gap lengths are same, the shake during the experiment will make the inductance value unbalance. For other structures, because the air gap is located on the center leg, the results of structures 3 and 4 are symmetry. Compared with other structures, structure 4 really has high inductance value resulting from the extra filter winding. But, the extra winding also brings the extra copper loss.

The efficiency comparison curves are shown in Fig. 4.26. From the efficiency curve of different structures, obviously, the discrete structure has the least efficiency for light load. The efficiencies for other four integrated magnetic structures are almost same. The small difference is mainly because the magnetics components resistor value is small compared with the whole circuit switching loss, semiconductor conduction loss and the circuit conduction loss. Compared with the discrete structure, the integrated magnetics structures have larger leakage inductance than the discrete magnetics structure, because there are air gaps in the core. When the load current is small, the advantage of IM structure is more obvious. If the load current is constantly increased, the leakage inductance effect will be increased and the difference between the IM structures and discrete structure will be decreased.
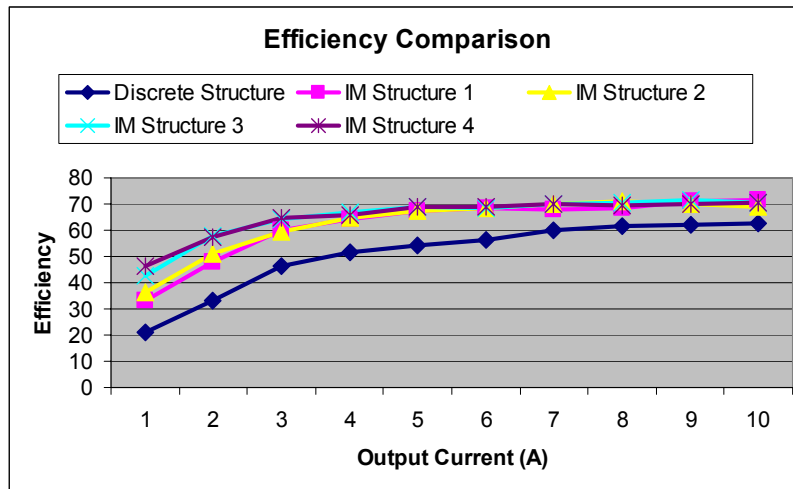
(a) Discrete structure and IM structures efficiency comparison
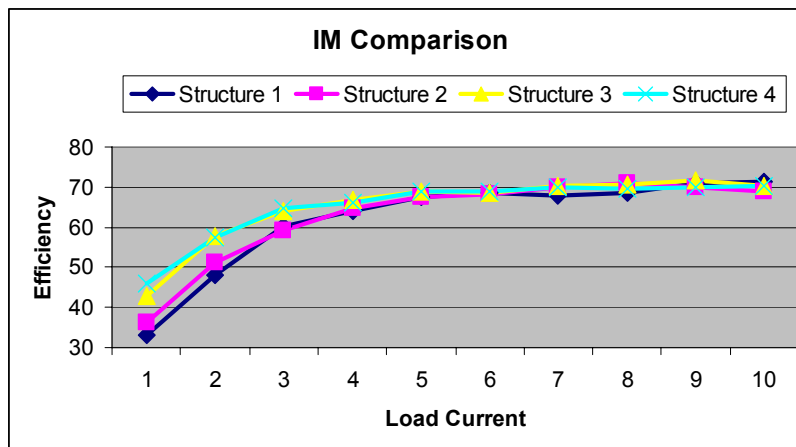
(b) IM structures efficiency comparison

Fig. 4.26 Different structures efficiency comparison

4.2.2 Half Bridge Integrated Magnetics Design

The specification of the integrated magnetics design is same as that of the discrete magnetics design:

Size:	0.9 in x 1.3 in x 0.2 in
Input:	36~75V
Output:	1.0V@30A
Load Slew Rate:	50 amps/us, ST 10us max
Deviaton:	3% with zero external capacitance
Efficiency:	86% @ full load
Swithching frequency:	$\geq$ 400kHz
I/O:	Surface-Mount, configuration not specified
Match Isolation:	Basic

Based on the comparison results of the previous section, the IM structure 3 is applied to the circuit design.

4.2.2.1 Design Procedures

The IM structure and reluctance model are shown in Fig. 4.15 and Fig. 4.16 separately. The design procedure is as follows:

1. Calculating the effective filter inductance value;

The effective filter inductance value L is expressed as:

$$L = \frac{V_0 \cdot (0.5 - D)}{\Delta I} \qquad\qquad (78)$$

2. Deciding the core section area;

In this design, the core structure is symmetry and the out leg areas are same. So the minimal out leg section area can be written as:

$$A_1 = A_2 \geq \frac{\dfrac{-V_0}{N_s} \cdot D \cdot T_s + \dfrac{1}{2} \cdot I_0 \cdot \dfrac{N_s}{R_0 + 2 \cdot R_c} + \dfrac{V_0}{2 \cdot N_s} \cdot D \cdot T_s}{B_{\max}} \qquad (79)$$

The minimal center leg section area is:

$$A_c \geq \frac{\dfrac{V_0}{N_s} \cdot (R_0 + 2 \cdot R_c) \cdot (0.5 - D) \cdot T_s + I_0}{(R_0 + 2 \cdot R_c) \cdot B_{\max}} \cdot N_s \qquad (80)$$

When the core material is chosen, the maximum flux density value will be determinated. Then, the core section area will be decided.

3. Selecting height;

In this design, the height is decided by the low profile circuit requirements.

4. Selecting window area;

The core window area should be big enough to accommodate all the windings and avoid the thermal issue. In the following discussion, two parameters are defined:

K_r : winding filling factor, practically, 0.2-0.4;

$J_{\max}$: maximum allowable current density, A/m^2, practically, 5-20 $MegA/m^2$, depending on the type of windings.

Then, for each window, the minimal required window area is estimated to be:

$$A_W \cong \frac{I_0}{K_r \cdot J_{\max}} \cdot \max_{D_{\min} \leq D \leq D_{\max}} \left(\frac{N_p}{N_s} \cdot \sqrt{D} + \frac{N_s}{2} \cdot \sqrt{1-D} \right) \qquad (81)$$

5. Calculating the air gap length;

118

When the core dimensions are decided, the air gap length can be calculated from the equations:

$$L = \frac{N_s^2}{R_0 + 2 \cdot R_c}$$

(82)

$$R_c = \frac{H - L_g}{\mu_r \cdot \mu_0 \cdot A_c} + \frac{L_g}{\mu_0 \cdot A_c}$$

(83)

6. CAD methodology is adopted which is introduced in section 4.2.1. The core dimension parameters are verified in the system simulation and the value can be adjusted to optimize the design.

4.2.2.2 Proposed Core Shape and Loss Comparison

The proposed magnetic core optimization includes two parts: core shape optimization and core volume optimization. Normally, the E core is suitable for the integrated magnetics design. To decrease the copper loss further, the new core shape is proposed. The concept comes from the basic idea: for the same area, the circle shape has least perimeter. So, changing shape of out legs can decrease the copper loss especially for the high current applications.

The proposed new core shape is shown in Fig. 4.27.
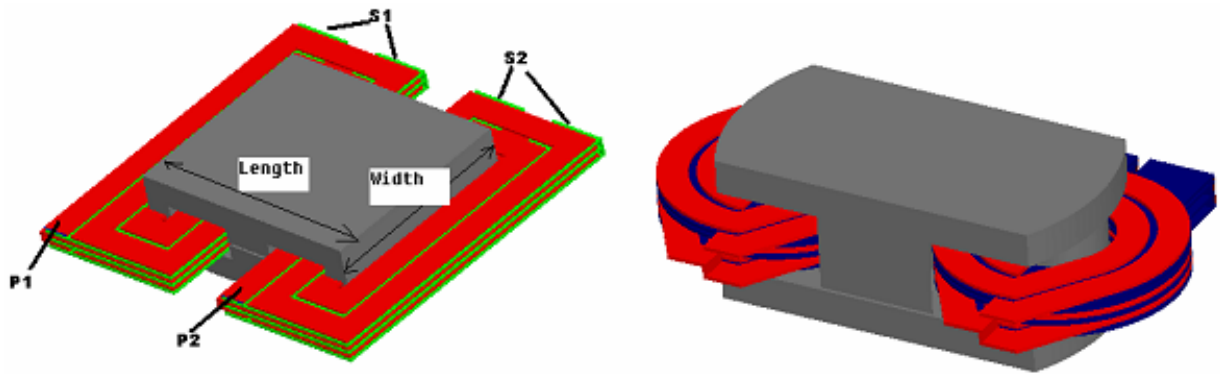
(a) E Core and the proposed customer core
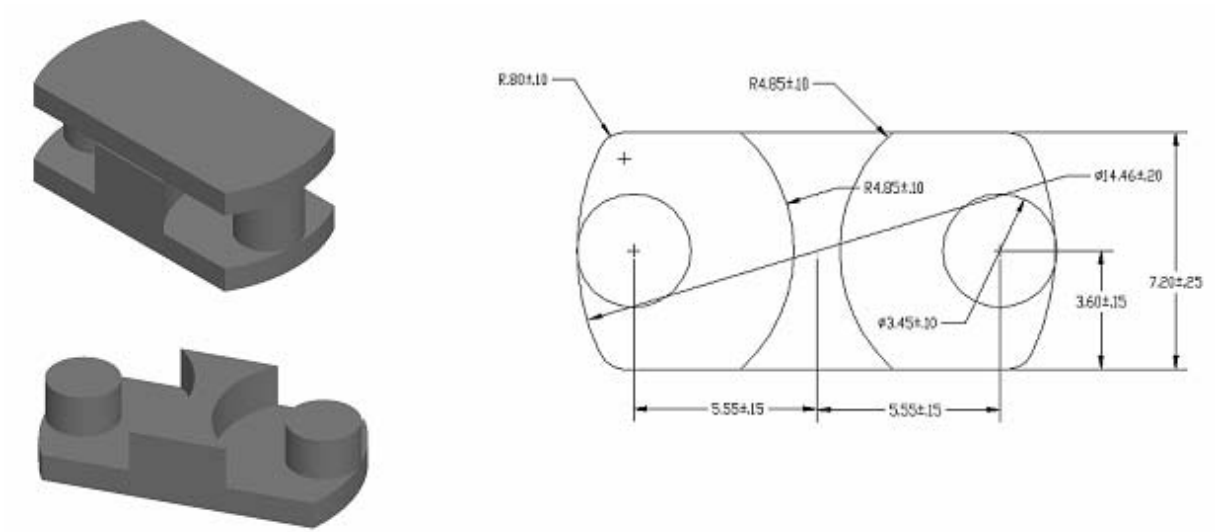
(b) Dimensions of proposed customer core

Fig. 4.27 Proposed new core shape

Because more copper areas are not covered by the magnetics core, the leakage inductance value of new shape is increased a little. Normally, the leakage inductance value is not as high as our transitional thought (5%). Most of the time, it is less than 2% or 3% of magnetizing inductance value. So, the little increasing of leakage inductance value is not an issue at all. On the other hand, we care more about the absolute value of the leakage inductance value. If the

120

absolute value is under control, the power stage will still work well. The 3D FEA model is constructed and simulated. The results are shown in Fig. 4.28. From the simulation results, the average flux density distributions satisfy the design requirements. But at the edge of the core, the flux density is high. So, some angles should be added to the vertical shape.
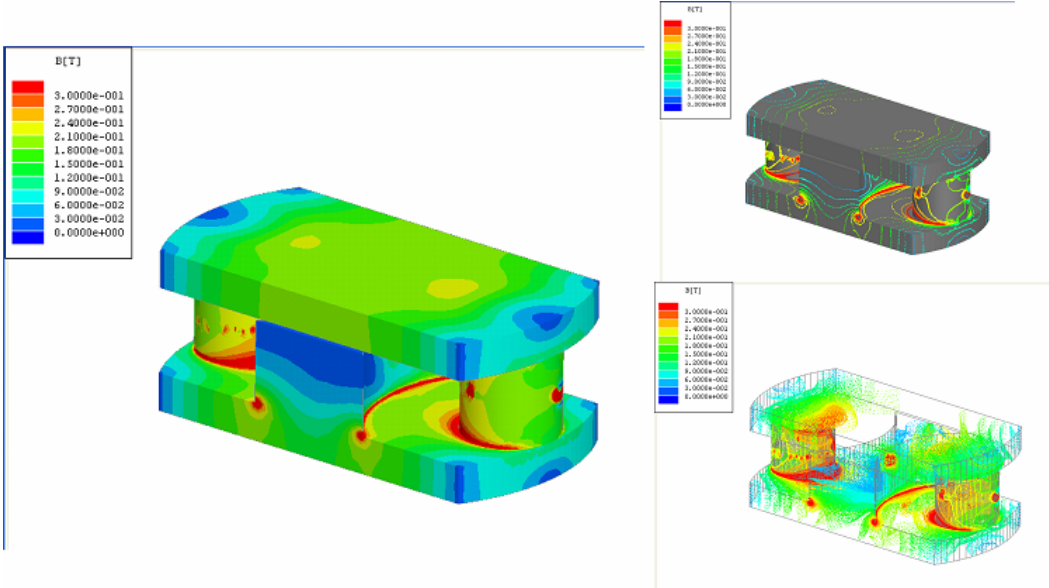
Fig. 4.28 Maxwell 3D simulation result

For the passive components, the 1-D model is very time efficient and can give an acceptable result as long as the conditions for the 1-D approximation can be well satisfied. In planar magnetics, the winding conductor thickness is always less than or equal to the skin depth of the conductor at the switching fundamental frequency, while it is also much smaller than the conductor width. The windings are also always placed far away from the air gap. This implies that the fringing effects and edge effects can be neglected in this structure. The 1-D winding loss

model is used in the volume optimization. The procedure is same as the one introduced in section 3.1.4.

The winding arrangement of the integrated magnetics is as follows:
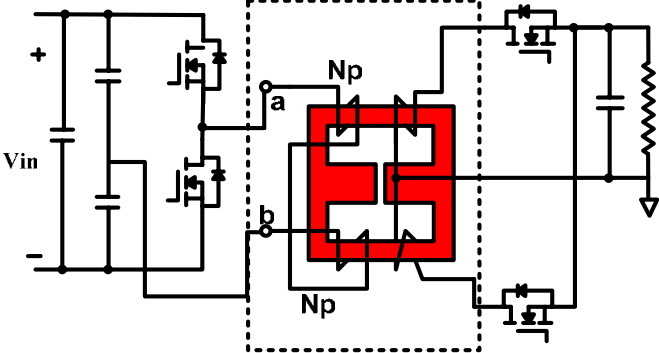
Fig. 4.29 Interleaved winding arrangement

The interleaving winding arrangement is selected and the structure is shown in Fig. 4.30.
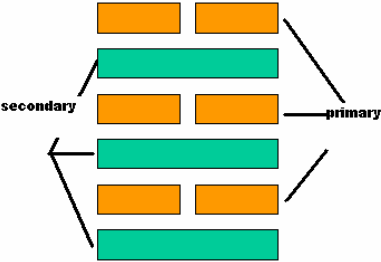
Fig. 4.30 Interleaved winding structure

In this design, the DC resistor value comes from the simple calculation. The AC resistor value comes from the Maxwell 3D simulation. The result includes all the parasitic effect, cross talking effect and so on. So, the result is more accurate. Table 4.7 is the power loss of different structure. From the calculated results, we can see that, if the customer core shape is adopted, the power loss can be decreased a lot.

122

Table 4.7 Power Loss of Different Components

	Separate inductors	Separate transformer	Integrated inductor	Integrated inductor and transformer	
core	EQ13	EQ13	ER14.5	E18	Custom Core
Core loss (w)	0.0314	0.2549	0.1	0.114	0.165
Cope loss (w)	0.1066	1.0542	0.391	1.864	1.251
Total loss (w)	0.138	1.3091	0.491	1.978	1.416
Length (mm)	2 x 12.8	12.8	21.5	28	31.2
Width (mm)	2 x 11.2	11.2	20.6	20	13.8
Height (mm)	5	5	5	5	5

4.2.2.3 Simulation Results

In the whole PCB board, the footprint area of integrated magnetics is less than that of the discrete magnetics structure. The footprint area of the integrated magnetics is 70% of the discrete magnetics structure.

From the Maxwell 3D simulation, the 3x3 matrix is extracted:

Table 4.8 Parameter Matrix

	P		L1		L2	
	Resistor (ohm)	Inductor (H)	Resistor (ohm)	Inductor (H)	Resistor (ohm)	Inductor (H)
P	0.079114	1.09E-4	0.001049	-9.14E-6	-1.96E-4	9.15E-6
L1	0.001049	-9.14E-6	4.54E-3	9.10E-7	5.72E-4	-7.61E-7
L2	-1.96E-4	9.15E-6	5.72E-4	-7.61E-7	3.25E-3	9.03E-7

Through the same method as the discrete magnetics, the Pspice model is constructed:
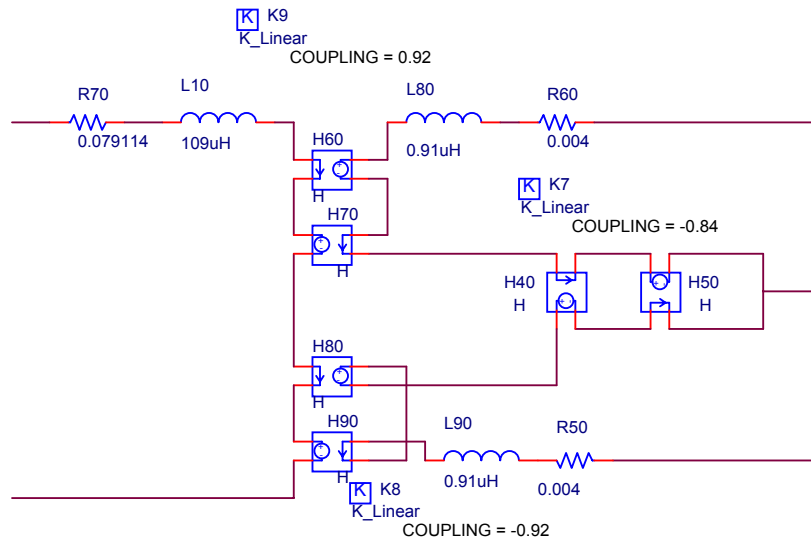
Fig. 4.31 Integrated magnetics Pspice model

Putting the integrated magnetics model into the whole circuit, the simulation result is shown the Fig. 4.32 and Fig. 4.33.
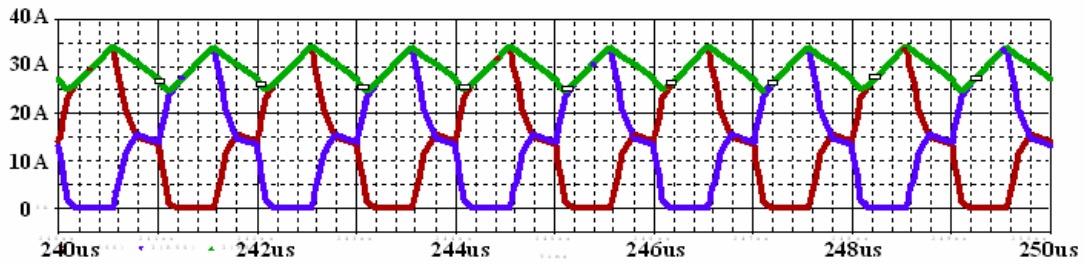
Fig. 4.32 Secondary side current waveforms
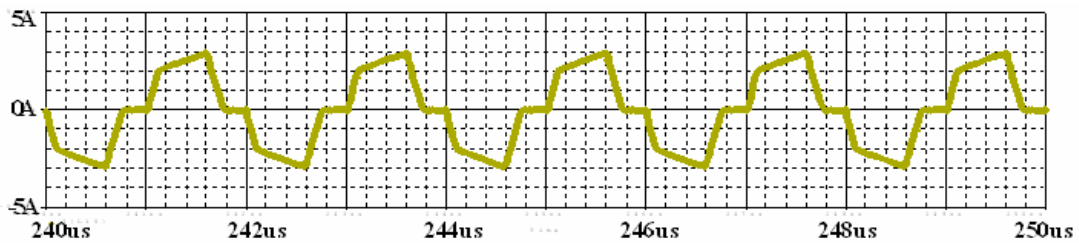
Fig. 4.33 Primary side current waveform

124

The comparison between the discrete structure and IM structure is shown in Table 4.9.

Table 4.9 Discrete structure vs. integrated structure

	Discrete Structure	Integrated Structure
Footprint Area	20mm*16mm	20.8mm*9.7mm
Effective Inductance Value	227nH	140nH
Primary Resistor	AC: 0.374 ohm DC: 0.016 ohm	AC: 0.079 ohm DC: 7.5m ohm
Inductor Resistor	AC: 5.68m ohm DC: 0.375m ohm	AC: 4.54m ohm DC: 0.42m ohm
Total winding number	4	3
Turn ratio	6 over 1	12 over 1
Winding Strategy	Simple	Complex

The comparison conditions are same footprint area and same output current ripple. Because the integrated structure has less effective inductance value, the transient response will be better. If the effective inductance values are same, the integrated structure will have smaller current ripple. The efficiency will also be higher.

The main reason for the different performance comes from the different coupling coefficient. This point is shown very clearly from the following parameter matrix.

	P		L1		L2	
P	0.374	1.29E-05	-0.026	-1.10E-06	2.60E-02	1.10E-06
L1	-0.026	-1.10E-06	5.68E-03	2.05E-07	1.20E-03	2.19E-08
L2	2.60E-02	1.10E-06	1.20E-03	2.19E-08	5.68E-03	2.05E-07

	P	L1	L2
P	1	0.676	0.676
L1	0.676	1	0.108
L2	0.676	0.108	1

Discrete Structure Parameters Matrix

	P		L1		L2	
P	0.079114	1.09E-04	0.001049	-9.14E-06	-1.96E-04	9.15E-06
L1	0.001049	-9.14E-06	4.54E-03	9.10E-07	5.72E-04	-7.61E-07
L2	-1.96E-04	9.15E-06	5.72E-04	-7.61E-07	3.25E-03	9.03E-07

	P	L1	L2
P	1	0.91754	0.92249
L1	0.91754	1	0.83926
L2	0.92249	0.83926	1

Integrated Structure Parameters Matrix

Fig. 4.34 Parameter Matrix

The resistor value of the discrete structure is bigger than that of integrated magnetics structure. This means high primary side power loss. The integrated magnetics structure has strong coupling in the secondary side. The secondary side can be treated as two coupled inductor structure. From the analysis in section 4.1.3, this can decrease the secondary current ripple.
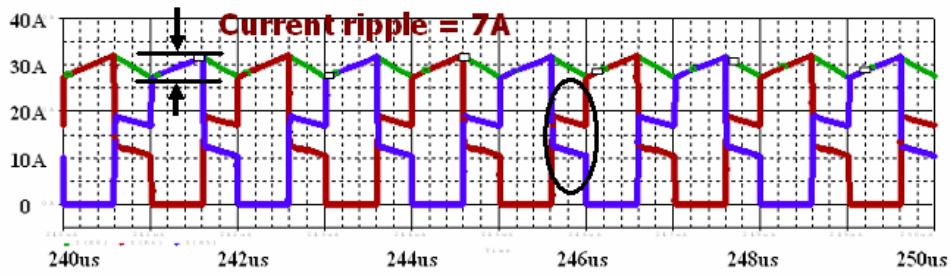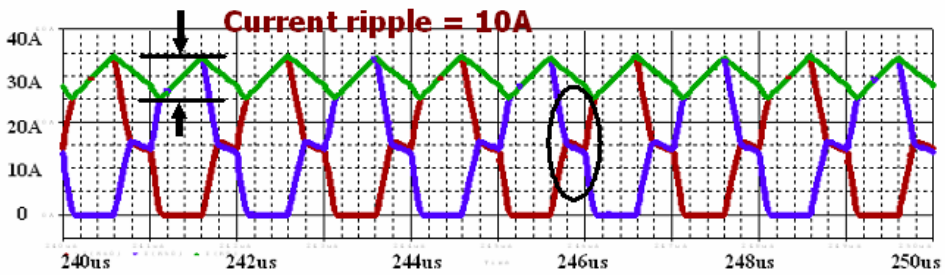
Fig. 4.35 Secondary side current waveforms
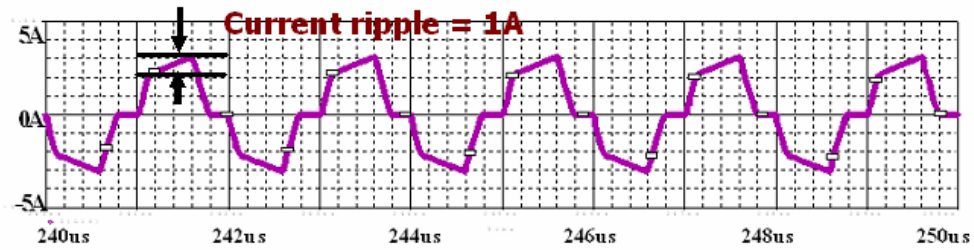
Fig. 4.36 Primary side current waveforms

127

The main components power loss is shown in Table 4.10. The total power loss is almost same. If the inductor value of integrated magnetics can be increased further, the efficiency of the integrated magnetics structure will be increased.

Table 4.10 Power loss of discrete structure vs. integrated structure

	primary side MOSFET power loss	secondary side MOSFET power loss	magnetic components power loss	total components power loss
discret structure	0.348w	2W	1.56W	3.9W
integrated struture	0.295W	1.82W	1.68W	3.8W

4.2.2.4 Experiment Verification
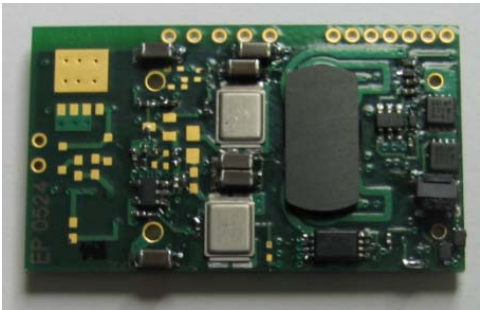
Fig. 4.37 Integrated magnetics PCB board

The primary current waveform and driver signal are shown in the Fig. 4.38.
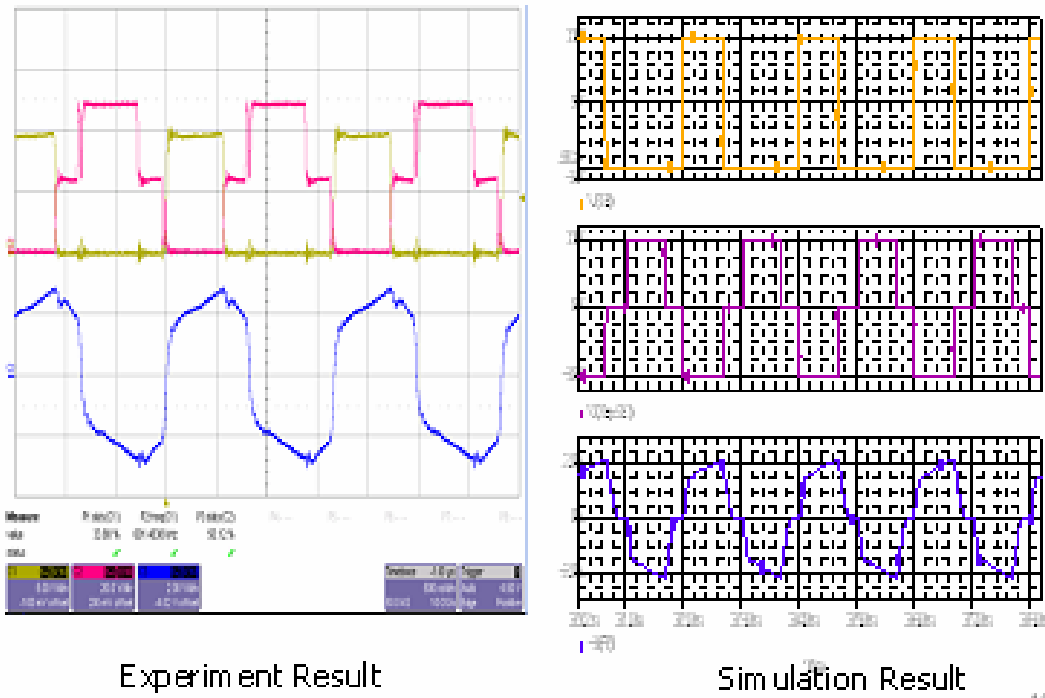
Fig. 4.38 Experimental waveforms vs. simulation waveform
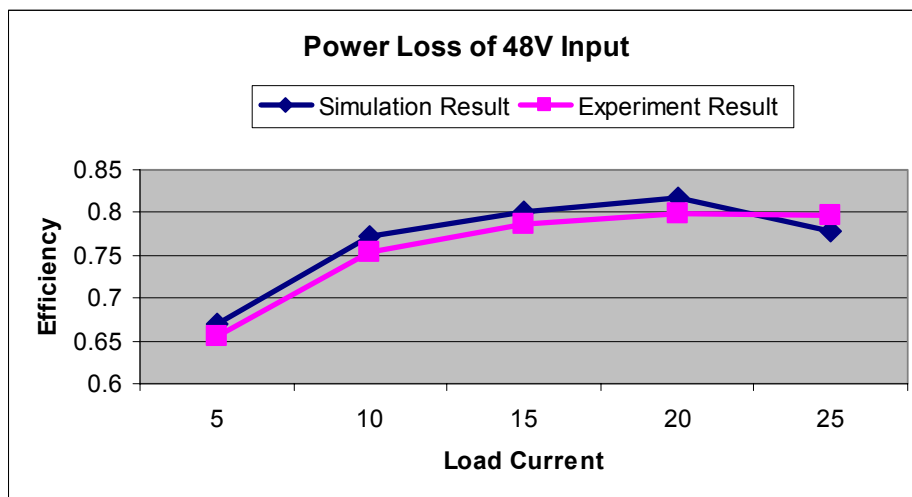
Fig. 4.39 Power loss vs. load

In Fig. 4.39, the power loss is shown when the circuit works under 48V input.

4.3 Integrated Magnetics for Peak Current Mode Control

As far as the control method is concerned, the use of standard peak current-mode control is precluded for half bridge rectifier by low-frequency stability problems, which show themselves through a drift of the input capacitors midpoint voltage. Thus, voltage mode control is generally used to cope with the two pole transfer function of the converter. In this case, for continuous conduction mode (CCM) of operation, a standard PID controller is adopted to achieve reasonable control loop bandwidth, with the drawback of an increase of high frequency noise coupled with the control circuitry and, above all, with the strong dependency of the crossover frequency on output capacitor ESR.

Compared with the voltage mode control, peak current-mode control is more attractive due to the following advantages: inherent over load limitation, higher loop bandwidth achievable with respect to voltage mode control and lower audio susceptibility. Due to the above mentioned instability problem, some provisions must be taken to implement the peak current control for half bridge topology.

4.3.1 Half Bridge Converter Current Mode Control Issue

Current mode control uses the error between the desired and actual output voltage to control the inductor current. As it is shown in Fig. 4.40, output current signal is sensed and transformed to corresponding voltage signal I_{cmp}. This signal is compared with the associated reference Iref, which reflects the error between output voltage and its reference, to give the duty control signals for the power devices. When I_{cmp} increases and is equal to its reference, the

corresponding power devices are turned off. The output voltage is controlled indirectly by the action of controlling inductor current. This feature provides very fast dynamic response as compared with conventional voltage mode control. At the same time, current control offers the cycle by cycle current limiting.
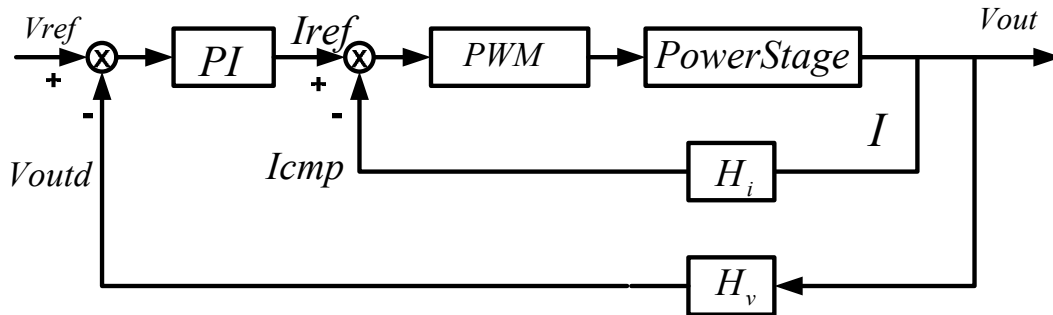
Fig. 4.40 Current mode control concept circuit

Fig. 4.41 shows the input stage of half-bridge converter. When the voltages of the two input capacitors are slightly different due to manufacturing and load variation, the duty cycle will be different for Fig. 4.41 (b) circuit and Fig. 4.41 (c) circuit. For example, when the Vcin1 ≠ Vcin2, the duty for "Q1" is greater than that of "Q2" if ''Vcin1'' is smaller than ''Vcin2'. As the result, the capacitor with smaller voltage value discharges more than the capacitor with greater voltage value. The same discharge cases occur in the following periods until the duty reaches its maximum value.
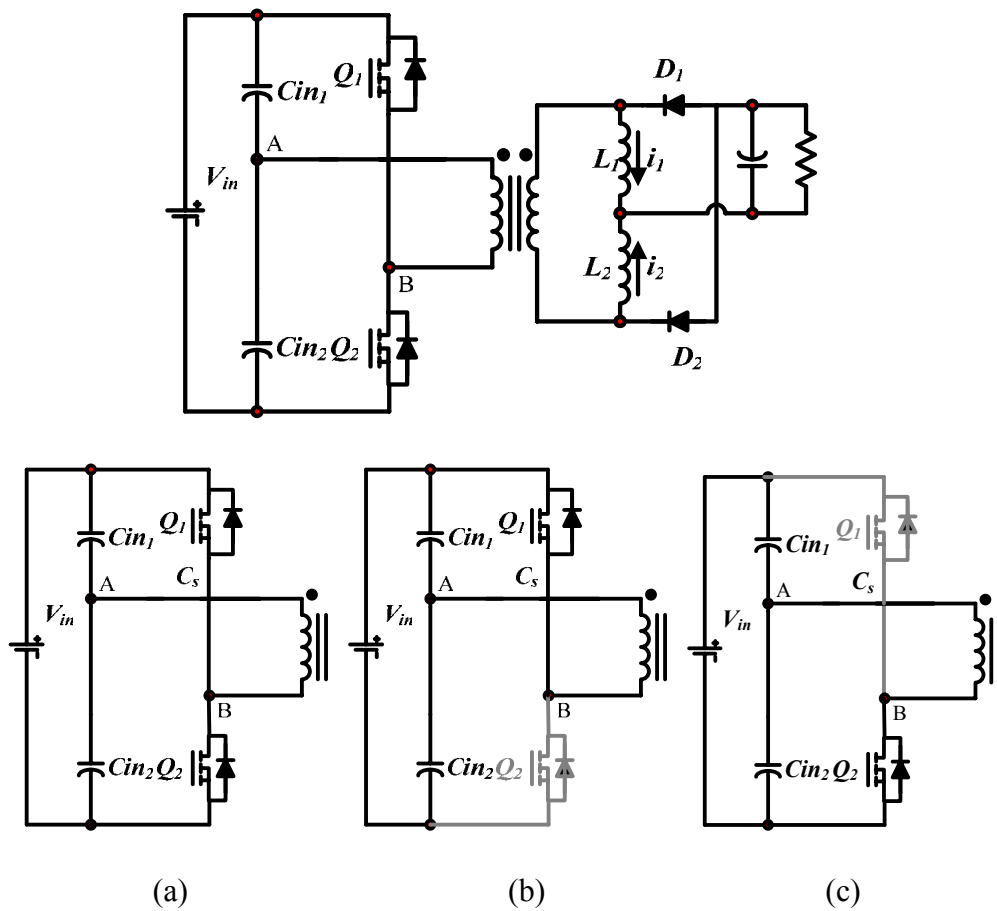
Fig. 4.41 Half-bridge voltage unbalance issue

4.3.2 Voltage Balance Technique

Changing the control loop is a solution to solve the voltage unbalance issue. Unfortunately, it needs more components for control design and control loop is more complicated compared with other methods.

One voltage balance technique iss presented in [46]. The topology is shown in Fig. 4.42. But it can't work well since the current sense circuit contains both load current and the magnetizing current for the auxiliary winding.
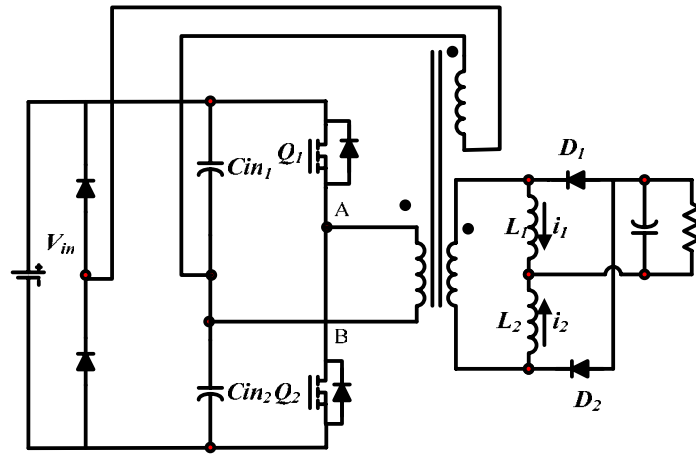
Fig. 4.42 Half-bridge voltage balance circuit

Another improved technique is introduced in [45] and it is shown in Fig. 4.43. The principle is similar to that shown in [46]. However, the magnetizing current of auxiliary transformer will not go through the primary winding of the main transformer of converter. Therefore the current sense circuit can precisely reflect the load working conditions for current mode control. Moreover, the presented technique provides a degree of freedom for auxiliary transformer design and implementation. Since the secondary side of auxiliary transformer needs to overcome the voltage drop caused by the series diode, the voltage should be slightly greater than that of the primary voltage of main transformer. With the presented technique, this requirement can be easily achieved by proper design of the turn ratio for auxiliary transformer.

133
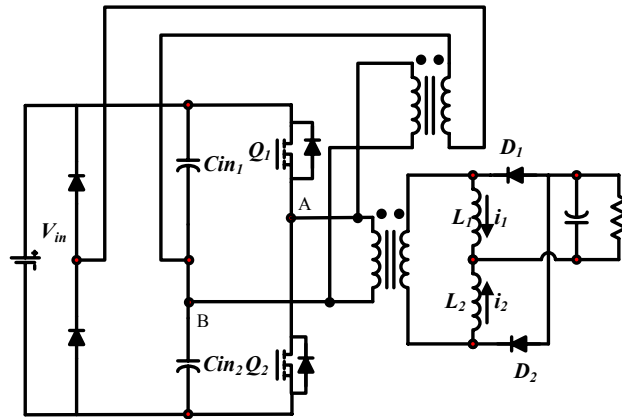
Fig. 4.43 Improved half-bridge voltage balance circuit

4.3.3 Proposed Integrated Magnetics Structure

Here, one new integrated magnetics structure based on the same concept is proposed. The circuit structure is shown in the following figure:
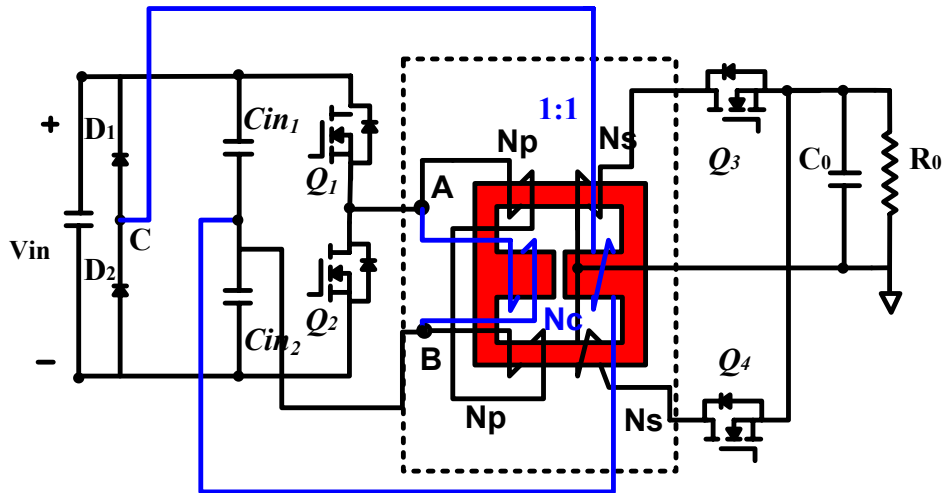
Fig. 4.44 Proposed half-bridge voltage balance IM circuit
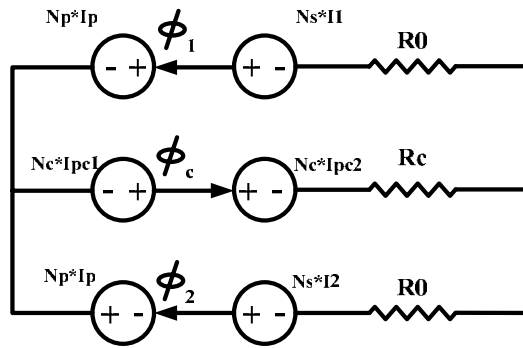
Fig. 4.45 Reluctance mode

The steady state operation of the proposed half bridge circuit includes three basic working modes.

Mode 1 [0, DT], Q1 is on and Q2 is off. Q3 is on and Q4 is off.
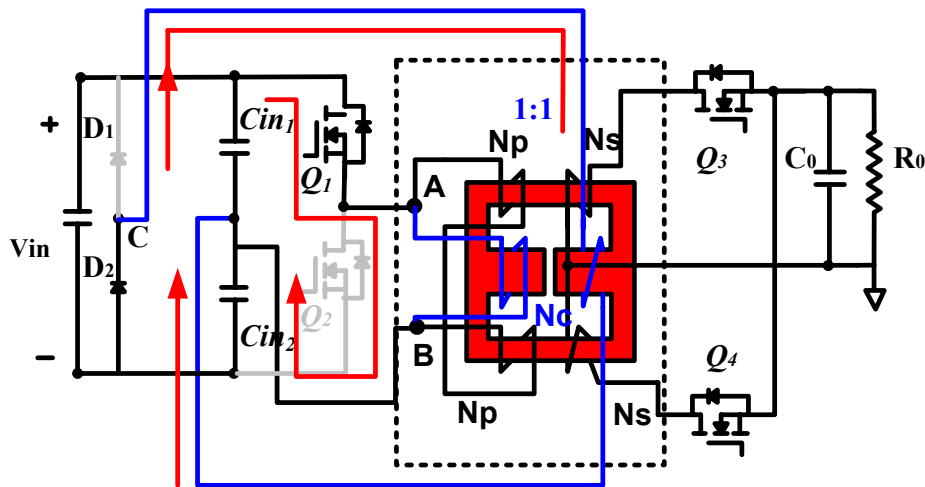
Fig. 4.46 Proposed circuit working mode 1

During this time period, the diode D2 is on and the node C voltage is settled near 0. The current direction in the blue winding is shown with the red line in the Fig. 4.46. Because the turn ratio of the two blue windings is 1:1, the voltage between node A and node B is same as the voltage between the node B and node C. The voltage V (A, B) is the capacitor voltage Vcin1. The voltage V (B, C) is the capacitor voltage Vcin2. In this situation, the two blue windings are working as extra voltage sources to force the two capacitor voltages to be equal. The voltage unbalance issue is solved and the current mode control can be applied to the half bridge circuit.

The reluctance mode is given in following figure:
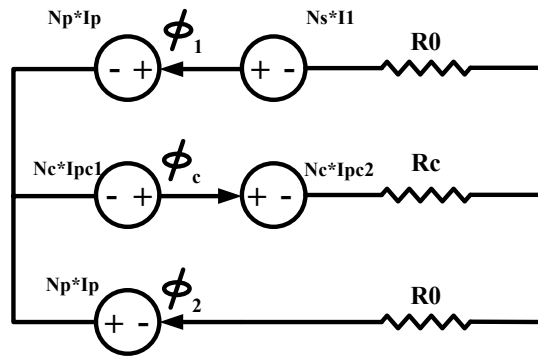
Fig. 4.47 Reluctance mode

The flux equations are:

$$\phi_1 = \frac{-1}{R_0} \cdot N_p \cdot i_p + \frac{R_0 + R_c}{R_0(R_0 + 2R_c)} \cdot N_s \cdot i_1 + \frac{1}{R_0 + 2R_c} \cdot \left(N_c \cdot i_{pc1} - N_c \cdot i_{pc2}\right)$$

$$\phi_2 = \frac{1}{R_0} \cdot N_p \cdot i_p - \frac{R_c}{R_0(R_0 + 2R_c)} \cdot N_s \cdot i_1 + \frac{1}{R_0 + 2R_c} \cdot \left(N_c \cdot i_{pc1} - N_c \cdot i_{pc2}\right)$$

$$\phi_c = \frac{1}{R_0 + 2R_c} \cdot N_s \cdot i_1 + \frac{1}{0.5 \cdot R_0 + R_c} \cdot \left(N_c \cdot i_{pc1} - N_c \cdot i_{pc2}\right)$$

(84)

From the Maxwell equations, the first secondary winding voltage: $V_1 = -V_0$. (85)

The second secondary winding voltage: $V_2 = \dfrac{N_s}{N_p} \cdot V_{in} - V_0$. (86)

The output voltage is V_0. So the effective transformer turn ratio is: $N_p : N_s$. (87)

Mode 2 [DT, 0.5T], Q1 is off and Q2 is off.
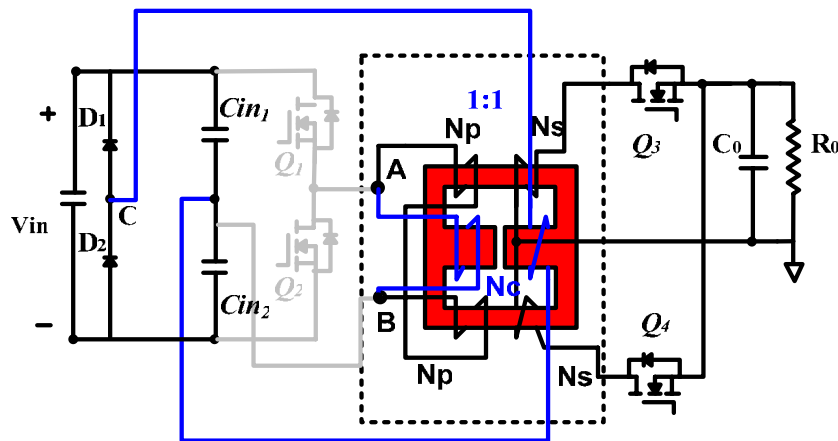
Fig. 4.48 Proposed circuit working mode 2

During this time period, the Q1 and Q2 are off. The voltage between the node A and node B V (A, B) is zero. D1 and D2 are off. There is no current flow in blue windings and winding Np. The two secondary windings Ns work as the filter inductor for the converter. The two windings are coupled with each other and share the total load current. This is suitable for high current applications.

The reluctance mode is:
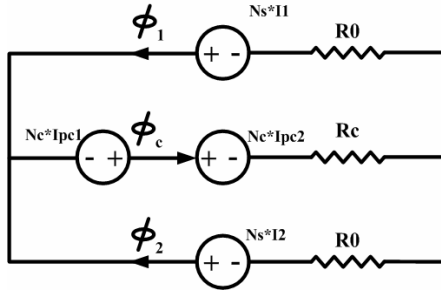
Fig. 4.49 Reluctance mode

The flux equations are:

$$\phi_1 = \frac{R_0 + R_c}{R_0(R_0 + 2R_c)} \cdot N_s \cdot i_1 - \frac{R_c}{R_0(R_0 + 2R_c)} \cdot N_s \cdot i_2 + \frac{1}{R_0 + 2R_c} \cdot \left(N_c \cdot i_{pc1} - N_c \cdot i_{pc2}\right)$$

$$\phi_2 = -\frac{R_c}{R_0(R_0 + 2R_c)} \cdot N_s \cdot i_1 + \frac{R_0 + R_c}{R_0(R_0 + 2R_c)} \cdot N_s \cdot i_2 + \frac{1}{R_0 + 2R_c} \cdot \left(N_c \cdot i_{pc1} - N_c \cdot i_{pc2}\right)$$

$$\phi_c = \frac{1}{R_0 + 2R_c} \cdot N_s \cdot i_1 + \frac{1}{R_0 + 2R_c} \cdot N_s \cdot i_2 + \frac{1}{0.5 \cdot R_0 + R_c} \cdot \left(N_c \cdot i_{pc1} - N_c \cdot i_{pc2}\right)$$

$$(88)$$

From the Maxwell equations, the effective inductance value for the coupled inductors is:

$$L = \frac{N_s^2}{R_0 + 2R_c}$$

$$(89)$$

Mode 3 [0.5T, (0.5+D) T], Q1 is off and Q2 is on. Q3 is off and Q4 is on.
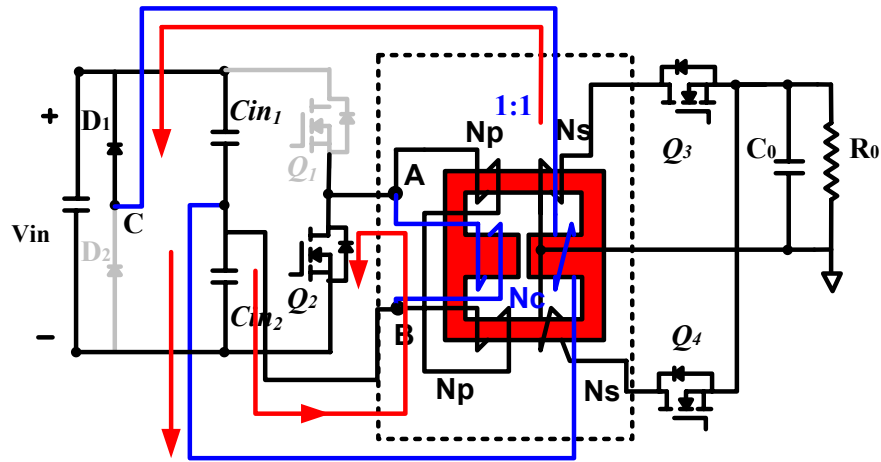
Fig. 4.50 Proposed circuit working mode 3

Similar to the mode 1, the diode D1 is on and the node C voltage is hold near Vin. The current direction in the blue winding is shown with the red line in the Fig. 4.50. Because the turn ratio of the two blue windings is 1:1, the voltage between node A and node B is same as the voltage between the node B and node C. The voltage V (A, B) is the capacitor voltage Vcin1. The voltage V (B, C) is the capacitor voltage Vcin2. The two blue windings are working as extra voltage sources to force the two capacitor voltage to be equal. The unbalanced capacitor voltage of current mode control is solved.

Because the circuit is symmetry, the reluctance mode is similar to the mode 1.

Mode 4 [(0.5+D) T, T], Q1 is off and Q2 is off. It is same as the mod 2.

Similar to the mode 2, the two secondary windings work as two coupled inductors. The reluctance mode is same as the mode 2.

The Maxwell 3D simulation has been finished for the integrated magnetic component. The coupling coefficient matrix is shown in Table 4.11. In this matrix, the L1 and L2 are the two secondary windings. The primary is the two part of primary winding that is connected in series. The P1 and P2 are the windings that are wound on the center leg.

Table 4.11 Maxwell 3D Coupling Matrix

	Primary	L1	L2	P1	P2
Primary	1	0.97703	0.44093	0.02072	0.01931
L1	0.97703	1	0.41039	0.18579	0.1747
L2	0.44093	0.41039	1	0.08319	0.07925
P1	0.02072	0.18579	0.08319	1	0.94139
P2	0.01931	0.1747	0.07925	0.94139	1

For each winding, the self coupling coefficient is 1. The mutual coupling coefficient is decided by the winding arrangement. The matrix shows that the windings on the center leg are almost decoupled from the other windings. These two windings work like a separate transformer. This transformer feeds forward to the primary side to apply the current mode control. Because it is decoupled from the other windings, the performance of the secondary side does not influence the control circuit.

In this integrated magnetic structure, blue winding works as the isolated voltage source. It will force the two capacitor voltage to follow each other and make the current mode control possible. Strongly coupled inductors can decrease the current ripple. Therefore, we can choose smaller inductance value to improve the transient response of the circuit.

Simulation results are shown in Fig. 4.51. The green curve and the yellow curve are the driver signal of the primary MOSFET. The purple curve is the primary current waveform. Fig. 4.51 is the primary waveform of conventional half bridge circuit with current mode control when the unbalance problem exists. Fig. 4.52 is the primary waveform of proposed circuit. The unbalance problem is solved.
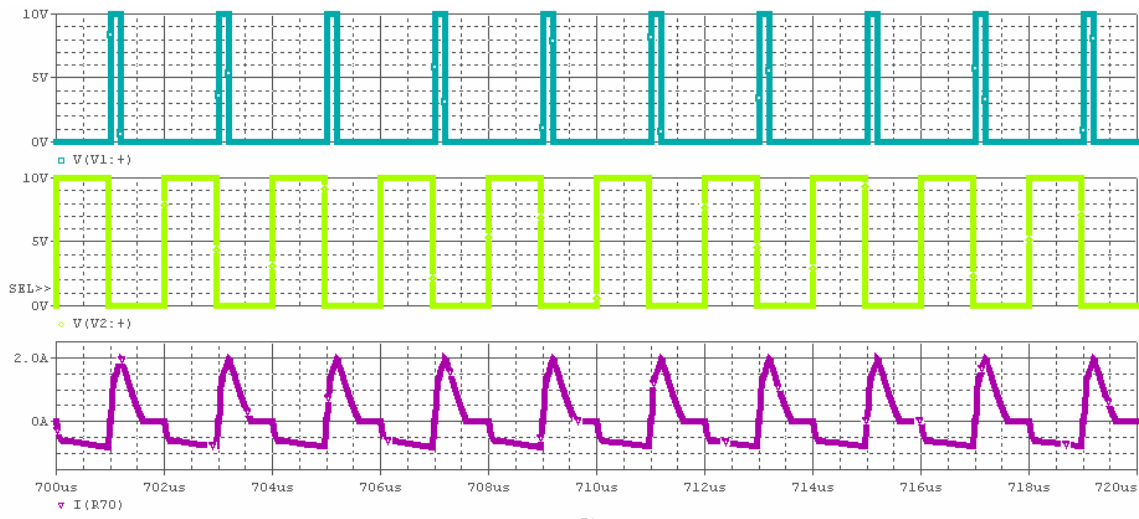
Fig. 4.51 Unbalanced waveforms for conventional half bridge current mode control
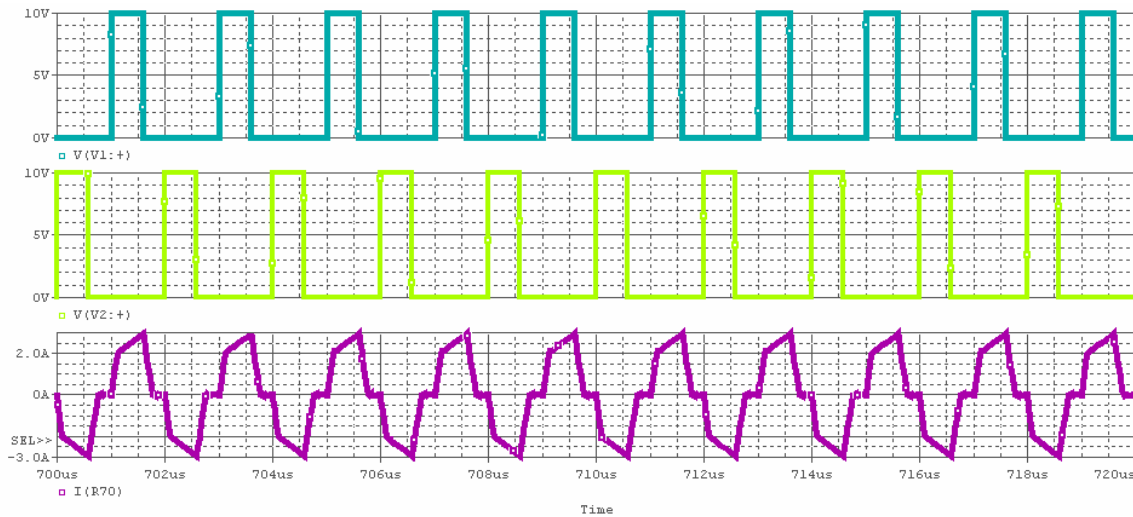
Fig. 4.52 Balanced waveforms for proposed half bridge current mode control

The proposed IM structure has simple structure compared with other method implementing the current mode control to half bridge topology. This structure can provide cycle by cycle peak current mode control. Because the connection loss in the integrated magnetics is less than that of the discrete structure, the efficiency is also high. The potential current doubler structure is integrated in the proposed structure; then the current ripple will be small. Normally, for the current mode control, high bandwidth and better transient response are available. From the analysis, it can be seen that this structure will supply feed forward control to the input line disturbance and good output regulation can be achieved.

CHAPTER 5: CONCLUSIONS

The advancement of technology requires that power supplies have high efficiency and high power density. Because the biggest volume in the whole converter board is normally occupied by the magnetics components, good magnetics component design becomes critical in the circuit. This dissertation addresses the following magnetics component issues in low voltage high current applications: integrated magnetics structure, unified circuit model, design methodology and new applications.

Current-doubler topology is presented in the literature as a possible method to reduce power losses in the transformer secondary side windings. The penalty for that improvement is an additional inductor. This inconvenience can be partially alleviated by integrating both transformer and inductors on a common core. Four integrated magnetics structures for current-doubler rectifier are investigated and compared thoroughly. Given the same core shape, same winding arrangement, same circuit connections and same foot print area, numerical FEA simulation results are compared and implemented to the electrical circuit analysis. Because of the complex winding arrangements, the windings lengths are increased and the efficiency is decreased. One optimized core shape is proposed in the dissertation to reduce the copper loss. The concept comes from the basic idea: for the same area, the circle shape has least perimeter.

Leakage inductance value and parasitic capacitance value are very critical parameters for the circuit performance. Many experimental phenomena are related to them. A CAD design methodology based on FEA simulation is proposed. Because the parameters of the circuit analysis model are directly extracted from the electromagnetic field analysis, the result is more

accurate and frequency dependent. The disadvantage of this CAD methodology is that we need to re-run the simulation when the component physical dimension is changed.

From the simulation results, the impedance matrixes are extracted. The order of the impedance matrix is decided by the winding number. For different winding number and different winding arrangement, it is difficult to make a reasonable comparison. One unified model is constructed in the dissertation. The whole component is modeled with general coupled inductors and only the terminal properties are considered in this circuit model. This will simplify the circuit analysis and make it possible to compare different structures.

Active transient voltage compensator (ATVC) is a good solution to the challenging high slew rate load current transient requirement of VRM. The transformer works as an extra voltage source. During the transient periods, the transformer injects or absorbs the extra transient to or from the circuit. ATVC only works in transient periods. Because the main VR only operates in low frequency in steady period, the efficiency of the VR is high.

The main advantage of the current mode control is its simpler dynamics. The transfer function has one less pole than the voltage mode control. So, the output voltage wide-bandwidth control can be obtained. An added benefit is the cycle by cycle over load protection. But, because of the inherent voltage unbalance issue, the current model control can not be implemented directly in the half bridge topology. A peak current mode controlled integrated magnetics structure is proposed in the dissertation. An extra transformer is added and works as a voltage source. It can force the two input capacitors of HB to have the same voltage potential. The proposed IM structure has simple structure compared with other methods implementing the

144

current mode control to half bridge topology. The simulation and theory analysis have verified the concept of new structure. The further experiment is needed.

For isolated low voltage high current applications, in order to improve the power density and the efficiency, the magnetic components should be integrated as much as possible. With the proposed unified magnetic model, the circuit simulation of different core and winding structures becomes possible. Applying the proposed magnetic methodology and unified model to evaluate the different coupling core and winding structures could be an interesting future research topic.

LIST OF REFERENCES

[1] C. Quinn, K. Rinne, T. O'Donnell, M. Duffy, and C. O. Mathuna: A review of planar magnetic techniques and technologies. IEEE APEC'2001, Vol. 2, pp: 1175-1183

[2] M. Rascon, J. Ara, R. Madsen, J. Navas, M. Perez, and F. San Miguel: Thermal analysis and modelling of planar magnetic components. IEEE APEC'2001, Vol. 1, pp. 97 -101

[3] P. D. Evans, and W. J. B. Heffernan: Multi-megahertz transformers. IEEE IAS'1995, Vol. 1, pp. 824 -832

[4] Bo Yang, Rengang Chen, and F. C. Lee: Integrated magnetic for LLC resonant converter. IEEE APEC'2002, Vol. 1, pp. 346-351

[5] Leung-Pong Wong, Yim-Shu Lee, and David Ki-Wai Cheng: A new approach to the analysis and design of integrated magnetics. IEEE APEC'2001, Vol. 2, pp. 1196-1202

[6] W. A. Roshen: A practical, accurate and very general core loss model for non-sinusoidal waveforms

[7] G. Schuellein, "Current sharing of redundant synchronous buck regulators powering high performance microprocessors using the V2 control method", in Thirteenth Annual Applied Power Electronics Conf. and Exposition, 1998, vol. 2, pp. 853–9.

[8] A.M.Wu, Jinwen Xiao, D. Markovic, and S.R. Sanders, "Digital PWM control: application in voltage regulation modules", in 30th Annual IEEE Power Electronics Specialists Conf., 1999, pp. 77–83 vol.1.

[9] Jinwen Xiao, A.V. Peterchev, and S.R. Sanders, "Architecture and IC implementation of a digital VRM controller", in 32nd Annual IEEE Power Electronics Specialists Conf., 2001.

[10] Xunwei Zhou, Pit-Leong Wong, Peng Xu, F.C. Lee, and A.Q. Huang, "Investigation of candidate VRM topologies for future microprocessors", IEEE Trans. on Power Electronics, vol. 15, no. 6, pp. 1172–82, 2000.

[11] G.J. Mehas, K.D. Coonley, and C.R. Sullivan, "Converter and inductor design for fast-response microprocessor power delivery", in Proceedings of the 31st Annual Power Electronics Specialist Conf., 2000, pp. 1621–6 vol.3.

[12] R. Miftakhutdinov, "Optimal design of interleaved synchronous buck converter at high slew-rate load-current transients", in 32nd Annual Power Electronics Specialists Conf., 2001.

[13] Pit-Leong Wong, Q. Wu, Peng Xu, Bo Yang, and F.C. Lee, "Investigating coupling inductors in the interleaving QSW VRM", in Proceedings of APEC 2000 - Applied Power Electronics Conf., pp. 973–8 vol.2.

[14] Pit-Leong Wong, Peng Xu, P. Yang, and F.C. Lee, "Performance improvements of interleaving VRMs with coupling inductors", IEEE Trans. on Power Electronics, vol. 16, no. 4, pp. 499–507, 2001.

[15] R. P. Sevems and G. E. Bloom, Modem DC-to-DC Switchmode Power Converter Circuits, Reprint Edition, dj BLOOM associates Inc., 1990,pp. 262-324 (ISBN 0-442-21396-4, Van Nostrand Reinhold, 1985).

[16] S. Ouk, "A New Zero-Ripple Switching Dc-to-Dc Converter and Integrated Magnetics," IEEE Power Electronics Specialists ConferenceRecord, 1980, pp. 12-32 (IEEE Pub. 80CH1529-7).

[17] W. J. Hirshberg, "Improving Multiple Output Converter Performance with Coupled Output Inductors," Proceedings of POWERCON 9, Power Concepts Inc., July 1982, pp. G4-1 to G4-5.

[18] G. E. Bloom and R. P. Sevems, 'The Generalized Use of Integrated Magnetics and Zero-Ripple Techniques in Switchmode Power Converters," IEEE Power Electronics Specialists Conference Record, 1984, pp. 15-33 (IEEE Pub. 84CH2000-8).

[19] G. E. Bloom, "New Integrated-Magnetic Power Converter Circuits for Telecommunications Systems," IEEE INTELEC Conference Record, 1984, pp. 359-366 (IEEE Pub. 84CH2073-5).

[20] G. E. Bloom, "New Integrated-Magnetic DC-DC Power Converter Circuits and System," IEEE APEC Record, 1987, pp. 57-66 (IEEE Pub. 86CH2312-7).

[21] R. Severns, "Circuit reinvention in power electronics and identification of prior work," in Proc. IEEE Applied Power Electronics Conference (APEC'97), 1997, pp. 3–9.

[22] K. O'Meara, "A new output rectifier configuration optimized for high frequency operation," in Proc. High Frequency Power Conversion (HFPC'91) Conference, 1991, pp. 219–226.

[23] C. Peng, M. Hannigan, and O. Seiersen, "A new efficient high frequency rectifier circuit," in Proc. High Frequency Power Conversion (HFPC'91) Conference, 1991, pp. 236–243.

[24] Pietkiewicz and D. Tollik, "Coupled-inductor current-doubler topology in phase-shifted full-bridge dc-dc converter," in Proc. INTELEC' 98 Conf., 1998, pp. 2–3.

[25] W. Chen et al., "Design of high efficiency, low profile, low voltage converter with integrated magnetics," in Proc. IEEE Applied Power Electronics Conference (APEC'97), 1997, pp. 911–917.

[26] P. Xu et al., "A novel integrated current doubler rectifier," in Proc. IEEE Applied Power Electronics Conference, 2000, pp. 735–740.

[27] J. Sun and V. Mehrotra, "Unified analysis of half-bridge converters with current-doubler rectifier," in Proc. IEEE Applied Power Electronics Conference, 2001, pp. 514–520.

[28] Changtong, K.; Erickson, R.W.; Maksimovic, D.; "A comparison of the ladder and full-order magnetic models", Power Electronics Specialists Conference, 2001. PESC. 2001 IEEE 32nd Annual Volume 4, 17-21 June 2001 Page(s):2067 - 2071 vol. 4

[29] Jieli Li; Abdallah, T.; Sullivan, C.R.; "Improved calculation of core loss with nonsinusoidal waveforms", Industry Applications Conference, 2001. Thirty-Sixth IAS Annual Meeting. conference Record of the 2001 IEEE Volume 4, 30 Sept.-4 Oct. 2001 Page(s):2203 - 2210 vol.4

[30] M. Albach, T. Durbaum, and A. Brockmeyer, "Calculating core losses in transformers for arbitrary magnetizing currents a comparison of different approaches.", in PESC 96 Record. 27th Annual IEEE Power Electronics Specialists Conference, June 1996, vol. 2, pp. 1463–8.

[31] J. Reinert, A. Brockmeyer, and R.W. De Doncker, "Calculation of losses in ferro- and ferrimagnetic materials based on the modified steinmetz equation", in Proceedings of 34th Annual Meeting of the IEEE Industry Applications Society, 1999, pp. 2087–92 vol.3.

[32] Brockmeyer, "Experimental evaluation of the influence of dc premagnetization on the properties of power electronic ferrites", in APEC '96. Eleventh Annual Applied Power Electronics Conference, 1996, pp. 454–60.

[33] Brockmeyer and J. Paulus-Neues, "Frequency dependence of the ferrite-loss increase caused by premagnetization", in Twelfth Annual Applied Power Electronics Conference and Exposition, 1997, pp. 375–80.

[34] Wai Keung Mo, D.K.W. Cheng, and Y.S. Lee, "Simple approximations of the dc flux influence on the core loss power electronic ferrites and their use in design of magnetic components", IEEE Transactions on Industrial Electronics, vol. 44, no. 6, pp. 788–99, 1997.

[35] G. Bertotti, Hysteresis in magnetism: for physicists, materials scientists, and engineers, Academic Press, 1998.

[36] M.S. Lancarotte and A. de Arruda Penteado, Jr., "Estimation of core losses under sinusoidal or nonsinusoidal induction by analysis of magnetization rate", in Electric Machines and Drives International Conference IEMD '99, 1999, pp. 490–492.

[37] New voltage balance technique for capacitors of symmetrical half-bridge converter with current mode control Yu-Chieh Hung; Fu-San Shyu; Chih Jung Lin; Yen-Shin Lai; Power Electronics and Drive Systems, 2003. PEDS 2003.

[38] P. L. Dowell, "Effects of eddy currents in transformer windings," Proc. Inst. Elect. Eng., vol. 113, no. 8, Aug. 1966.

[39] M. P. Perry, "Multiple layer series connected winding design for minimum losses," IEEE Trans. Power App. Syst., vol. PAS-98, no. 1, Jan./Feb. 1979.

[40] J. A. Ferreira, Electromagnetic Modeling of Power Electronic Converters. Norwell, MA: Kluwer, 1989.

[41] "Improved analytical modeling of conductive losses in magnetic components," IEEE Trans. Power Electron., vol. 9, no. 1, pp. 127–131, Jan. 1994.

[42] J. P. Vandelac and P. Ziogas, "A novel approach for minimizing high frequency transformer copper loss," in Proc. IEEE PESC'87, 1987, pp. 355–367.

[43] R. Severns, "A simple, general method for calculating HF winding loss for arbitrary current waveforms," High Freq. Power Convers., vol. 6, pp. 149–159, Jun. 1991. E. C. Snelling, Soft Ferrite, Properties and Applications, 2nd ed. London, U.K.: Butterworth, 1988.

[44] New voltage balance technique for capacitors of symmetrical half-bridge converter with current mode control

[45] Yu-Chieh Hung; Fu-San Shyu; Chih Jung Lin; Yen-Shin Lai; Power Electronics and Drive Systems, 2003. PEDS 2003. The Fifth International Conference on Volume 1, 17-20 Nov. 2003 Page(s):365 - 369 Vol.1

[46] Unitrodc, "A 300W, 300 kHz currcnt modc half bridge convcrtcr with multiplc outputs using couplcd inductors," Power S~rppl~v Design Seminar, 1994.

[47] X. Wang, Issa Batarseh, "active transient voltage compensator for VRM transient improvement at high current slew rate load", IEEE-APEC2005, pp: 1430-1435

[48] Qiong Li and Fred C. Lee, "Deisng consideration of transformer DC bias of forward converter with active-clap reset" . IEEE 1999

[49] C. Quinn, K. Rinne, T. O'Donnell, M. Duffy, and C. O. Mathuna: "A review of planar magnetic techniques and technologies." IEEE APEC'2001, Vol. 2, pp: 1175-1183

[50] M. Rascon, J. Ara, R. Madsen, J. Navas, M. Perez, and F. San Miguel: "Thermal analysis and modelling of planar magnetic components." IEEE APEC'2001, Vol. 1, pp. 97 -101

[51] N. Dai, A. W. Lotfi, G. Skutt, W Tabisz, F. C. Lee: "A comparative study of high frequency low profile planar transformer technologies." IEEE APEC'94, pp.153 – 161

[52] Jieli Li, "Using coupling inductors to enhance transient performance of multi-phase buck converters", Proc. IEEE APEC2004, pp.1289-1293

[53] Philips Magnetic Components: "Design of Planar Power Transformers."

[54] Application Note, "Design of Planar Power Transformer," www.ferroxcube.com.

[55] "30A 12V-input programmable integrated switching regulator PT8120 series", Texas Instruments application datasheets.

[56] C. Quinn, K. Rinne, T. O'Donnell, M. Duffy, and C. O. Mathuna: A review of planar magnetic techniques and technologies. IEEE APEC'2001, Vol. 2, pp: 1175-1183

[57] M. Rascon, J. Ara, R. Madsen, J. Navas, M. Perez, and F. San Miguel: Thermal analysis and modelling of planar magnetic components. IEEE APEC'2001, Vol. 1, pp. 97 -101

[58] P. D. Evans, and W. J. B. Heffernan: Multi-megahertz transformers. IEEE IAS'1995, Vol. 1, pp. 824 -832

[59] G.J. Mehas, K.D. Coonley, and C.R. Sullivan, "Converter and inductor design for fast-response microprocessor power delivery", in Proceedings of the 31st Annual Power Electronics Specialist Conf., 2000, pp. 1621–6 vol.3.

[60] Pit-Leong Wong, Peng Xu, P. Yang, and F.C. Lee, "Performance improvements of interleaving VRMs with coupling inductors", IEEE Trans. on Power Electronics, vol. 16, no. 4, pp. 499–507, 2001.

[61] Xunwei Zhou, "Low-Voltage High-Efficiency Fast Transient Voltage Regulator Modules," Ph.D. Dissertation, Virginia Polytechnic Inst. State Univ., Blackburg, 1999.

[62] Y. Panov and M. Jovanovic, "Design and Performance Evaluation of Low-Voltage/High-Current DC/DC On-Board Modules," IEEE Fourteenth Annual Applied Power Electronics Conference and Exposition, APEC'99, Vol. 1, pp. 545–552, 1999.

[63] X. Zhu, Bo Yang, L. Amoroso, F. C. Lee, and P. Wong, " A Novel High-Input-Voltage, High Efficiency and Fast Transient Voltage Regulator Module: The Push-Pull Forward Converter," Fourteenth Annual Applied Power Electronics Conference and Exposition, 1999. APEC '99., Volume: 1, 14-18 March 1999, Page(s): 279–283, Vol. 1.

[64] Jaber A. Abu-Qahouq, Hong Mao, and Issa Batarseh, "Novel Control Method for Multiphase Low-Voltage High-Current Fast Transient VRMs," 2002 IEEE 33rd Annual Power Electronics Specialists Conference, PESC '02, Page(s): 1576 –1581, Vol. 4, 2002.

[65] Hong Mao, Jaber Abu-Qahouq, Shiguo Luo, and Issa Batarseh, "New Zero-Voltage-Switching Half-Bridge DC-DC Converter and PWM Control Method," Eighteenth Annual IEEE Applied Power Electronics Conference and Exposition, APEC 2003, Vol. 2, Pages: 635-640, February 2003.

[66] P. Xu, R. Yuan-Chen, M. Ye, and F. C. Lee, "A Family of Novel Interleaved DC/DC Converters for Low-Voltage High-Current Voltage Regulator Module Applications," IEEE 32nd Annual Power Electronics Specialists Conference, 2001, PESC 2001, 17-21 June 2001, Volume: 3, Page(s): 1507 –1511.

[67] Jaber A. Abu Qahouq, "High-Density High-Current Fast-Transient Low-Voltage DC-DC Converters," Ph.D. Dissertation, University of Central Florida, Orlando, Florida, 2003.

[68] C. Peng, M. Hannigan, O. Seiersen, "A new efficient high frequency rectifier circuit", Proc. of HFPC' 91, pp. 236-243.

[69] K. O'Meara, "A new output rectifier configuration optimized for high frequency operation", Proc. of HFPC'

[70] L. Balogh, "Design review: l00W, 400kHz, dc/dc converter with current doubler synchronous rectification achieves 92% efficiency", Unitrode Seminar Manual

[71] N. Kutkut, "A full-bridge soft-switched telecom power supply with a current-doubler rectifier", Proc. Of Intelec' 97, pp. 344-35 1.

[72] Enrico Santi and Slobodan Cuk, "Comparison and design of three coupled inductor structures", Industrial Electronics, Control and Instrumentation, 1994. IECON '94.

[73] Jieli Li, Charles R. Sullivan, and Aaron Schultz, "Coupled inductor design optimization for fast-response low-voltage DC-DC converters", in IEEE Applied Power Electronics Conference, 2002.

[74] A. M. Schultz and C.R. Sullivan, "Voltage converter with coupled inductive windings, and associated methods", 2002, U.S. Patent number 6,362,986, Volterra Semiconductor Corp.

[75] Pit-Leong Wong, Q. Wu, Peng Xu, Bo Yang, and F.C. Lee, "Investigating coupling inductors in the interleaving QSW VRM", in Proceedings of APEC 2000 - Applied Power Electronics Conf., 2000, vol. 2, pp. 973–978.

[76] Pit-Leong Wong, Peng Xu, P. Yang, and F.C. Lee, "Performance improvements of interleaving VRMs with coupling inductors", IEEE Trans. on Power Electronics, vol. 16, no. 4, pp. 499507, 2001.

[77] P. Zumel, O. Garca, J. Cobos, and J. Uceda, "Magnetic integration for interleaved converters", in IEEE Applied Power Electronics Conference, 2002.

[78] Robert W. Erickson, Fundamentals of Power Electronics, Kluwer Academic Publishers, fourth printing edition, 1999.

[79] Jian Sun, Kenneth F. Webb and Vivek Mehrotra "Integrated magnetics for current-doubler rectifiers", IEEE Transaction on Power Electronics, VOL.19, No.3, May 2004.

[80] Peng Xu, Mao Ye, Pit-Leong Wong and Fred C. Lee "Design of 48V voltage regulator modules with a novel integrated magnetics", IEEE Transaction on Power Electronics, VOL.17, No.6, Nov. 2002.

[81] Wei Chen, et.al, "Design of high efficiency, low profile, low voltage converter with integrated magnetics", IEEE 1997.

[82] Lloyd Dixon, "Deriving the equivalent electrical circuit from the magnetic device physical properties".